ABSTRACT

Title of dissertation: MULTI-BAND BOSE-HUBBARD MODELS AND EFFECTIVE THREE-BODY INTERACTIONS

Saurabh Paul, Doctor of Philosophy, 2016

Dissertation directed by: Professor Eite Tiesinga
Joint Quantum Institute
Department of Physics
University of Maryland, College Park

Experiments with ultracold atoms in optical lattice have become a versatile testing ground to study diverse quantum many-body Hamiltonians. A single-band Bose-Hubbard (BH) Hamiltonian was first proposed to describe these systems in 1998 and its associated quantum phase-transition was subsequently observed in 2002. Over the years, there has been a rapid progress in experimental realizations of more complex lattice geometries, leading to more exotic BH Hamiltonians with contributions from excited bands, and modified tunneling and interaction energies. There has also been interesting theoretical insights and experimental studies on "unconventional" Bose-Einstein condensates in optical lattices and predictions of rich orbital physics in higher bands. In this thesis, I present our results on several multi-band BH models and emergent quantum phenomena. In particular, I study optical lattices with two local minima per unit cell and show that the low energy states of a multi-band BH Hamiltonian with only pairwise interactions is equivalent to an effective single-band Hamiltonian with strong three-body interactions. I also propose a

second method to create three-body interactions in ultracold gases of bosonic atoms in a optical lattice. In this case, this is achieved by a careful cancellation of two contributions in the pair-wise interaction between the atoms, one proportional to the zero-energy scattering length and a second proportional to the effective range. I subsequently study the physics of Bose-Einstein condensation in the second band of a double-well 2D lattice and show that the collision aided decay rate of the condensate to the ground band is smaller than the tunneling rate between neighboring unit cells. Finally, I propose a numerical method using the discrete variable representation for constructing real-valued Wannier functions localized in a unit cell for optical lattices. The developed numerical method is general and can be applied to a wide array of optical lattice geometries in one, two or three dimensions.

MULTI-BAND BOSE HUBBARD MODELS AND EFFECTIVE THREE-BODY INTERACTIONS

by

Saurabh Paul

Dissertation submitted to the Faculty of the Graduate School of the
University of Maryland, College Park in partial fulfillment
of the requirements for the degree of
Doctor of Philosophy
2016

Advisory Committee:
Dr. Steve L. Rolston, Chair
Dr. Eite Tiesinga, Advisor
Dr. Paul D. Lett
Dr. Mohammad Hafezi
Dr. Dionisios Margetis

Dedication

I dedicate this thesis to my parents, my brothers and my wife.

Acknowledgments

My interest in science, and physics in particular, developed at an early age largely due to my brothers' persistence. They introduced me to science and mathematics in an interesting and accessible way. This interest always grew, thanks in part to my family, and teachers during my school and college days in India. I would not have come this far, but for this wonderful start right in my family.

I would like to thank my advisor, Prof. Eite Tiesinga, who has been a source of constant guidance. He would always have time to discuss on problems, at times throughout the day, and gave me the opportunity to work at my own pace. His insights and suggestions have helped me come up with problems and solutions that otherwise looked elusive. I would like to thank Dr. Paul D. Lett, Dr. Mohammad Hafezi and Dr. Dionisios Margetis for being on my thesis committee, and Prof. Steve L. Rolston for chairing the committee.

I have had some wonderful friends at the Joint Quantum Institute and the University of Maryland in general. Discussions with them would always lighten me up and motivate me to look at the brighter side of things. Life without them would indeed have been quite lonely.

I would like to thank my parents who have been a constant source of support. Finally, I would like to thank my wife for being always by my side during thick and thin. Her enthusiasm and liveliness would keep my spirits up. Her support was key in this long, and at times, arduous journey.

Table of Contents

List of Tables

List of Figures

Chapter 1

Overview

1.1 Optical Lattice

Systems of ultracold atoms trapped in periodic potentials best known as optical lattices have become a hotbed of experimental implementations of diverse quantum many-body Hamiltonians owing to their inherent high degree of tunability. Realization of complex lattice geometries have further enhanced the scope to study evermore interesting physical systems, in particular quantum many-body Bose-Hubbard (BH) models with contributions from excited bands and richer atom-atom interactions. The present thesis is primarily devoted to the study of such models.

Optical lattices are periodic potentials created by interfering counter propagating lasers to form standing waves [1]. The simplest form is a cubic lattice with periodicity $\lambda/2$ in each direction, where λ is the laser wavelength. In recent years, however, lattices with complex geometries have been realized, such as double-well lattices [2–5], honeycomb, triangular, one-dimensional stripe and Kagome lattices [6, 7], and artificial graphene [8]. Figure 1.1 shows contour plots of two such

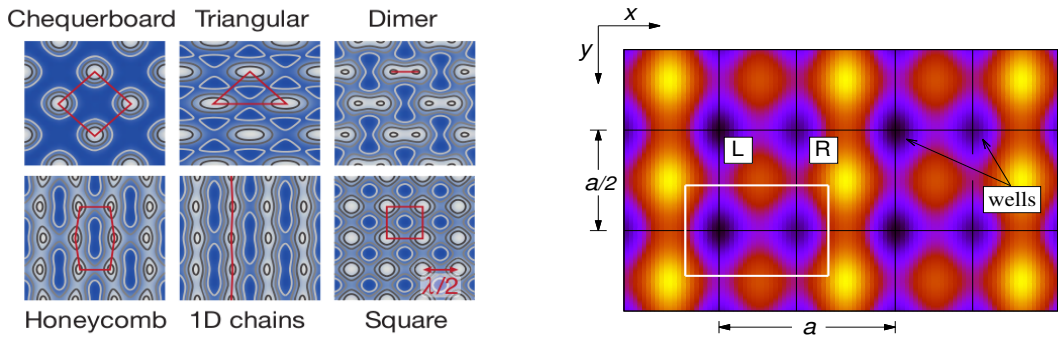

(a) (b)

Figure 1.1: (a) Contour plots of two-dimensional optical lattice potentials [6] with six different geometries created by simply tuning the parameters of a single lattice potential. The red lines denote the unit cell and the white regions represent potential minima. (b) A double-well lattice potential often studied in this thesis [9]. Dark blue regions represent the potential minima while the white box encloses a unit cell. Individual wells within each double-well are denoted by L and R.

optical lattice potentials. Both have been experimentally realized. The double-well potential in Fig. 1.1b is used throughout this thesis. A simple sinusoidal potential along the transverse direction is assumed.

1.2 Multi-band Bose-Hubbard models

The behavior of ultracold cold atoms trapped in sufficiently deep optical lattices can be described by the commonly used single-band BH model [1, 11]. All BH models are an approximation to the full many-body Hamiltonian in the tight-binding limit and are obtained by restricting the atoms to occupy one or more

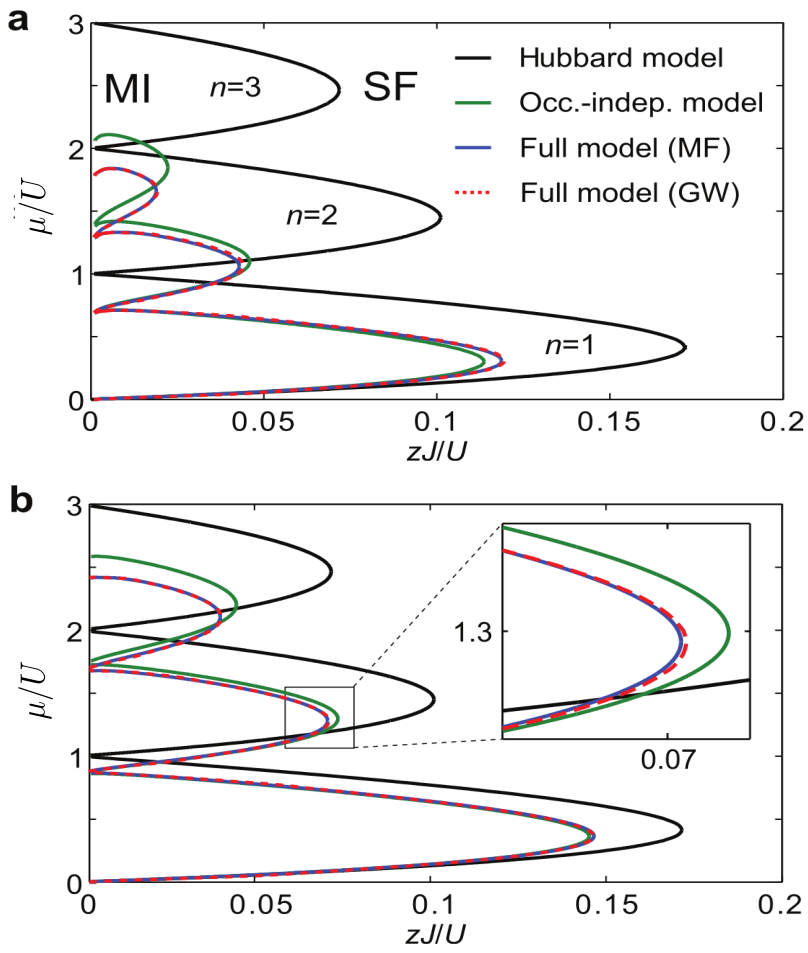

Figure 1.2: Phase diagrams of superfluid (SF)-Mott (MI) transition in a simple cubic lattice [10]. The vertical axis shows the dimensionless chemical potential μ/U and the horizontal axis shows the dimensionless tunneling energy zJ/U. Panels (a) and (b) are for two typical positive values of the interaction strength U. Black lines correspond to the single-band BH model while the green line refers to a single-band BH model that includes density-induced tunneling, both using mean-field (MF) theory. The Hamiltonian corresponding to the green curve is referred to as occupation-independent Hamiltonian in Ref. [10]. The blue (MF) and dashed red (Gutzwiller) lines include, in addition, contributions from excited bands. The Mott lobes correspond to $n = 1, 2$ and 3 atoms per unit cell.

Bloch bands or equivalently only occupy the corresponding localized Wannier functions. For deep lattices, the band gap between the lowest two bands is typically much larger than the energy scales involved in the system dynamics. Thus, atoms primarily populate the lowest band and in addition, the hopping matrix elements beyond nearest neighbors, to a good approximation, can also be neglected. Under these conditions, the system is described by the single-band BH model [12]. This Hamiltonian is thus characterized by a single-particle tunneling energy J between Wannier function of adjacent unit cells and pairwise atom-atom interaction energy U between atoms occupying the same lattice site. By varying the relative strength of the tunneling energy and atom-atom interaction strength, this model predicts a quantum phase transition between a delocalized compressible superfluid state and a localized incompressible Mott state [12, 13]. This was first observed by Greiner *et al.* [14] in a cubic lattice.

Recent studies have shown that couplings between adjacent unit cells due to atom-atom interactions are also important and can lead to significant density-induced tunneling energies. For simple cubic lattices, such additional terms in the BH Hamiltonian have been shown to measurably modify the location of the superfluid (SF) to Mott (MI) phase boundaries [10, 15]. Figure 1.2 shows the effect of density-induced tunneling energies on the SF-Mott insulator phase transition as computed using a cubic lattice in Ref. [10]. Here z denotes the number of nearest neighbors and μ is the chemical potential. Note that to reasonable approximation, μ/U corresponds to the mean atom number per unit cell. Figures 1.2(a) and (b) correspond to two different interaction strengths U. The black lines correspond to the

phase boundary obtained between a superfluid and a Mott insulator ground state using the single-band BH model within the mean-field (MF) theory [13]. The phase boundaries in green are obtained with a MF theory of a BH model including contributions from nearest-neighbor density-induced tunneling. The density-induced tunneling energy, although much smaller than the on-site interaction energies, leads to an effective increase in single-particle hopping. This results in a marked difference in the SF-Mott phase boundary between the two models and in fact, enhancement of the tunneling energy considerably reduces the area where the ground state is a Mott insulator. Including the effects of excited bands further shifts the SF-Mott phase boundary (although not so drastically), as shown by the blue and dashed red curves. The blue curve correspond to a MF calculation while a Gutzwiller Ansatz [12] is used to obtain the dashed red curve.

Significantly altered SF-Mott phase boundaries are similarly observed for cold atom systems using complex lattice geometries. For lattice geometries having more than one potential minima in a unit cell, a single-band BH model is inadequate owing to the relatively small band-gap between the ground and first (or even higher) excited band(s). In fact, strong atom-atom interaction energies involving higher bands and large excited band tunneling energies play a crucial role in determining the behavior of these systems [9, 16]. In addition, the BH model might also need to include tunneling energies beyond nearest-neighbors [9, 17]. I determined the SF-Mott phase transition (using numerical MF calculation) for ^{87}Rb atoms in a symmetric double-well optical lattice [9]. The phase diagram is shown in Fig. 1.3. A contour plot of this double-well potential is shown in Fig. 1.1b, where the lattice

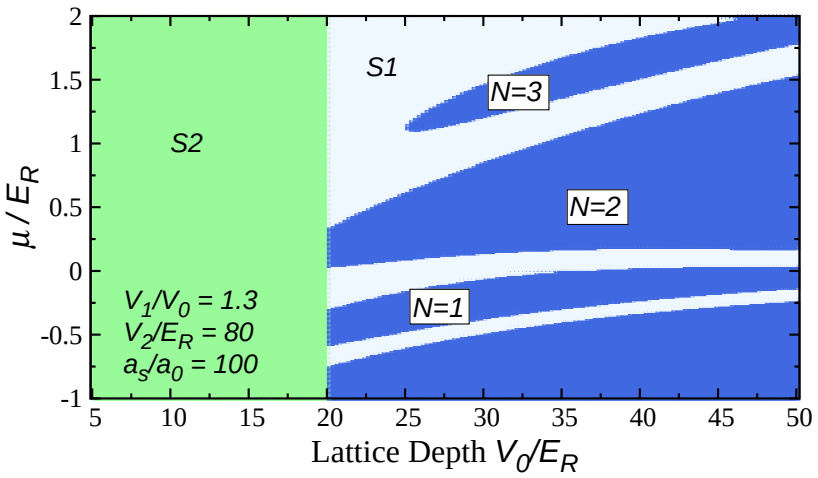

Figure 1.3: Phase diagram for ^{87}Rb in a symmetric double-well lattice as a function of lattice depth and chemical potential in units of the recoil energy $E_R = \hbar^2 k_L^2/(2m)$, where k_L is the laser wave vector and m is the atomic mass [9]. Dark blue regions are the Mott lobes, while $S1$ and $S2$ are superfluid phases.

depths along the three directions are parametrized by three strengths V_0, V_1 and V_2 (see Eq. (2.2)) and the barrier height between L and R wells within a double-well is controlled by the ratio V_1/V_0. It is evident from the figure that the phase diagram significantly differs from that of a single-band BH model (see Fig. 1.2), in that the Mott lobes do not monotonically decrease in size with increasing atom number. For the double-well system, the interplay between the atom-atom interaction induced pair-tunneling term and the band-gap between the lowest two bands crucially determine the behavior of the system [9]. Most interestingly, I will show in chapter 2 that the low-energy states of this system actually emulate a Hubbard model with strong three-body interactions.

1.3 Effective three-body interactions

There has been a lot of interest in broadening the scope of BH models and associated quantum phases accessible to cold atom systems. I have discussed some of these ideas in the previous section. In conjunction, efforts are also underway to create exotic interactions, and in particular, three-body interactions. Many-body Hamiltonians with three-body interaction can have significantly modified quantum phases [18–24] that can have promising uses in quantum computation [25].

Three-body interactions always arise out of pairwise two-body interactions. Johnson *et al.* [26] showed, using the ideas of effective field theory, that virtual transitions to excited energy bands generate effective three-body interactions between atoms in the ground band of an optical lattice. Their results were obtained for a deep 3D lattice where tunneling can be neglected. Thus, the system can be described by an effective Hamiltonian of the form

$$\tilde{H}_{\text{eff}} = \sum_{m=1}^{3} \frac{1}{m!} \tilde{U}_m a^{\dagger m} a^m, \tag{1.1}$$

where $a^\dagger(a)$ are creation (annihilation) operators of atoms in the lowest Wannier function of a lattice site and $\tilde{U}_m$ represents the effective m-body interaction energy. In this case, virtual transitions arise out of second- and higher-order perturbative corrections to the ground state energy due to two-body interactions between atoms occupying the ground band. Leading-order perturbative shifts in the energy are represented in Fig. 1.4. The labels μ and ν represent band indices. Figures 1.4(b) and (c) show second-order perturbative two-body processes. The contributions from

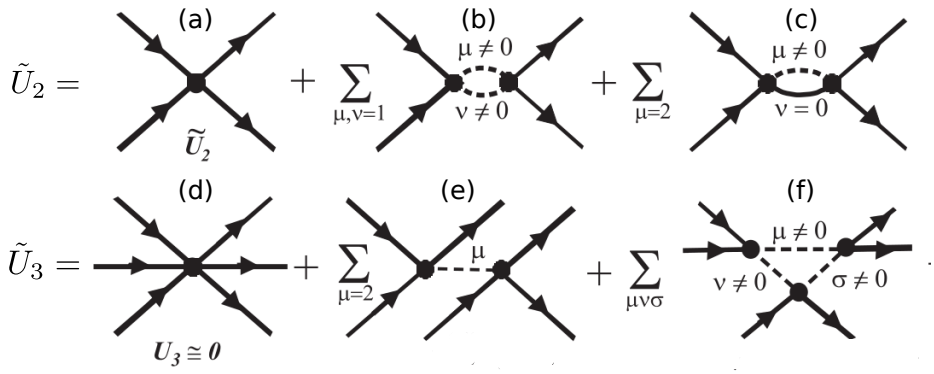

Figure 1.4: Diagrams representing leading perturbative terms that shift the ground state energy [26]. The effective two-body interaction energy $\tilde{U}_2$ is given through second order by diagrams (a)-(c). Diagrams (d)-(f) are examples of processes contributing to the effective three-body interaction energy $\tilde{U}_3$.

these terms diverge and are regularized and renormalized by a counter-term (see Ref. [26]) to ensure that $\tilde{U}_2$ is the effective two-body interaction energy. Figure 1.4(e) is the leading order effective three-body process contributing to $\tilde{U}_3$. Reference [26] subsequently showed that $\tilde{U}_3$ is negative, producing attractive three-body interactions, and is much smaller than $\tilde{U}_2$, i.e., the results are well within the perturbative regime. Similar ideas using virtual transitions to excited bands have been explored in Refs. [27–29]. These weak effective three-body interactions in optical lattices have been experimentally observed [30–33].

Recent proposals have centered around reducing the strength of the two-body term, thereby enhancing the role of three-body interactions. In fact, Ref. [34] by driving the lattice at rf frequencies and Ref. [35] by adding resonant radiation to couple internal states of an atom have proposed ways to turn off the two-body

interaction altogether. It was shown in [36] that arrays of superconducting Josephson junctions can also mimic a strong three-body interaction.

In chapter 2, I show that for ultracold atoms in an optical lattice with two local minima per unit cell, the low energy states of a multi-band BH Hamiltonian with only pair-wise interactions is equivalent to an effective single-band Hamiltonian with strong repulsive three-body interactions [9]. The results are obtained for a double-well optical lattice potential with a symmetric double well along the x axis and a sinusoidal potential along the perpendicular directions. First, tunneling and two-body interaction energies are obtained from an exact band-structure calculation. The numerically-constructed Wannier functions are used to construct a BH Hamiltonian spanning the lowest two bands. This numerical method is detailed in chapter 5.

Next, we construct the effective Hamiltonian from the ground state of the N-atom Hamiltonian for each unit cell obtained within the subspace spanned by the Wannier functions of the two lowest bands. Interestingly, the model allows for hopping between ground states of neighboring unit cells, and is thus, not limited to deep lattices. The effective Hamiltonian is shown to have strong three-body interactions that can be easily tuned by changing the lattice parameters. Relying on numerical mean-field simulations, we further show that the effective Hamiltonian is an excellent approximation of the two-band BH Hamiltonian over a wide range of lattice parameters, both in the superfluid and Mott insulator regions.

In chapter 3, I discuss a second way to create dominant attractive three-body interactions in Hubbard models. We derive that the effect of pair-wise interactions

can be made small or zero starting from the realization that collisions occur at the zero-point energy of an optical lattice site and the strength of the interactions is energy dependent from effective-range contributions. We determine the strength of the two- and three-body interactions for scattering from van-der-Waals potentials and near Fano-Feshbach resonances. For van-der-Waals potentials, which for example describe scattering of alkaline-earth atoms, we find that the pair-wise interaction can only be turned off for species with a small negative scattering length, leaving the ^{88}Sr isotope a possible candidate. Interestingly, for collisional magnetic Feshbach resonances this restriction does not apply and there often exist magnetic fields where the two-body interaction is small. We illustrate this result for several known narrow resonances between alkali-metal atoms as well as chromium atoms.

In conclusion to this section, I should draw the reader's attention to the fact that the effective three-body interactions discussed in this thesis are in the limit of small scattering length. In the strong scattering limit, three-body interactions have been studied through Efimov physics [37], which is detected through the measurement of three-body recombination, where three colliding atoms create a dimer and a free atom. Interestingly, there exist infinitely many three-body bound states, with the ratio of the binding energy between successive states approaching a universal constant.

1.4 Bose-Einstein condensation in an excited band

Bose-Einstein condensation or superfluidity of ultracold atoms in the lowest Bloch band of a periodic optical-lattice potential [1, 38] occurs at zero quasi-momentum. This condensation can be understood from a bosonic Hubbard model. According to Feynman's "no-node" theorem [39], the zero quasi momentum ground state wave function is positive definite and has time-reversal (TR) symmetry. However, the no-node theorem does not apply to excited bands and the lowest energy state within the band may have non-zero quasi momenta. Thus, we can obtain exotic states of bosons with complex-valued wave functions that spontaneously break the TR symmetry [40, 41]. Simultaneously, depending on the lattice parameters, two or more bands can become nearly degenerate realizing multiflavor Hubbard models where the atom-atom interaction strength is of the order of bandgaps. In addition, for these bands with nearly degenerate excited orbitals, tunneling can be "anisotropic" in that different orbitals tunnel preferably along different primitive lattice vectors. This has lead to several proposals of unconventional Bose-Einstein condensates in optical lattices and predictions of rich orbital physics in higher bands [40–45]. For example, Wirth *et al.* [46] explores orbital superfluidity in $sp-$hybridized orbital bands in which condensation occurs at non-zero quasi momentum at the edge of the first Brillouin zone. Interestingly, Refs. [40, 42] showed that Bose-Einstein condensates formed in excited Bloch bands may have very long lifetimes. Recently, such condensates have been experimentally observed [2, 46–48].

I study the formation and collision-aided decay of an ultra-cold atomic Bose-

Einstein condensate in the first excited band of a double-well 2D-optical lattice with weak harmonic confinement in the perpendicular z direction in chapter 4. This lattice geometry is based on an experiment by Wirth *et al.* [46]. The double well is asymmetric, with the local ground state in the shallow well nearly degenerate with the first excited state of the adjacent deep well. In order to obtain analytical results, I have used a tight-binding model with Wannier functions approximated as non-orthogonal localized harmonic-oscillator wave functions. A comparison of the band structure obtained from a tight-binding model with that obtained numerically using a plane wave basis shows the tight binding model to be in quantitative agreement for the lowest two bands, qualitative for next two bands, and inadequate for even higher excited bands. For the lattice considered, the band widths of the excited bands are much larger than the harmonic oscillator energy spacing in the z direction. A study of the thermodynamics of a non-interacting Bose gas in the first excited band gives an estimate of the condensate fraction and critical temperature, T_c as functions of lattice parameters. For typical atom numbers, the critical energy $k_B T_c$, with k_B the Boltzmann constant, is larger than the excited band widths and harmonic oscillator energy. Finally, I present an estimate of the time scale for two-body collision-aided decay of the condensate as a function of lattice parameters. The decay channels are shown in Fig. 1.5. It involves two processes, the dominant one in which both colliding atoms decay to the ground band, and a second involving excitation of one atom to a higher band. For this estimate, I have used tight-binding wave functions for the lowest four bands, and numerical estimates for higher bands. The decay rate rapidly increases with lattice depth [49]. Close to the critical temperature, however,

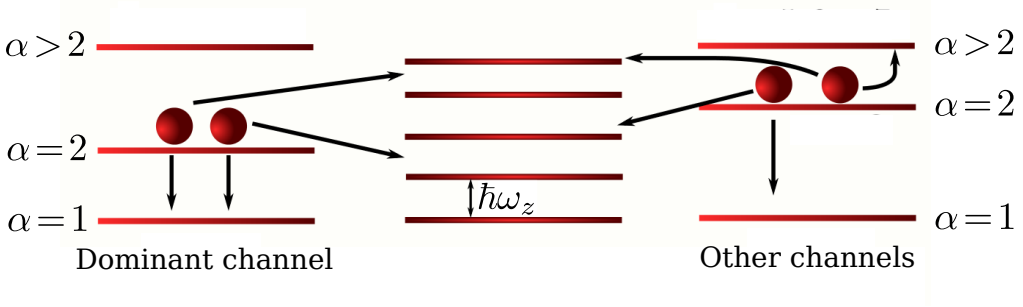

Figure 1.5: Decay channels for the collision aided decay of a condensate formed in the first excited band ($\alpha = 2$) of a double-well 2D optical lattice with weak harmonic confinement along z direction with energy spacing $\hbar\omega_z$. The dominant channel (left panel) involves both colliding atoms decaying to the ground band ($\alpha = 1$), while other channels (right panel) involve one of the atoms scattering to an excited band ($\alpha > 2$). To conserve energy, both atoms are simultaneously raised to appropriate oscillator levels along the z axis (middle panel). For details, see Ref. [49].

it stays smaller than the tunneling rate between adjacent wells, thus allowing the needed time for the formation of a condensate in an excited band.

1.5 Determining the Bose-Hubbard parameters

With the rapid expansion in the experimental realization of complex BH models, there has been a growing need to quantitatively model these systems with greater accuracy. The BH models are written in a single-particle basis of spatially localized wave functions, generally referred to as Wannier functions. The parameters of the BH model are obtained as integrals over these functions. Thus, the key to accurately model these systems is to first construct a set of properly localized orthonormal basis functions. For simple cubic lattices with inversion symmetry, the standard procedure is to construct Wannier functions as "simple" superpositions of the Bloch functions belonging to a *single* energy band [50, 51]. For more complex lattice geometries with either asymmetries or quasi-degenerate energy bands, this procedure, however, does not lead to basis functions localized at the potential minima within each unit cell.

A common approach to ensuring localized Wannier functions for atoms in optical lattices is to use non-orthogonal atomic orbitals, modeled as harmonic oscillator wave functions near the potential minima [49, 52]. This underestimates the tunneling energies even for deep lattices where the harmonic approximation is expected to work better. A more general approach developed within the solid-state community is due to Marzari and Vanderbilt [53, 54], where maximally localized Wannier

functions are constructed by minimizing its spread by a suitable gauge transformation of the Bloch functions. This scheme has been adapted for atoms in optical lattices [17,55–58]. Wannier functions obtained using this method, however, are not guaranteed to be real-valued and in turn depend on the choice of gauge transformation. An alternate method for constructing Wannier functions is by minimization of density-induced tunneling and density-density interactions between neighboring unit cells [59].

In chapter 5, I introduce a numerical method using the discrete variable representation (DVR) for constructing real-valued approximate Wannier functions localized in a unit cell for both symmetric and asymmetric periodic potentials. We apply these results to finding Wannier functions for ultracold atoms trapped in laser-generated optical lattices. Following Kivelson [60], for a symmetric lattice with inversion symmetry, we construct Wannier functions as eigenstates of the position operators $\hat{x}$, $\hat{y}$ and $\hat{z}$ restricted to single-particle Bloch functions belonging to one or more bands. To ensure that the Wannier functions are real-valued, we numerically obtain the band structure and real-valued eigenstates using a uniform Fourier grid DVR. We then show by a comparison of tunneling energies, that the Wannier functions are accurate for both inversion symmetric and asymmetric potentials to better than ten significant digits when using double-precision arithmetic. The calculations are performed for an optical lattice with double-wells per unit cell with tunable asymmetry along the x axis and a single sinusoidal potential along the perpendicular directions. Localized functions at the two potential minima within each unit cell are similarly constructed, but using a superposition of single-particle

solutions from the two lowest bands. We finally use these localized basis functions to determine the two-body interaction energies in the BH model, and show the dependence of these energies on lattice asymmetry.

1.6 Outline

The rest of the thesis is organized into five chapters. Results of chapter 2 have been published in Physical Review A in a paper titled "Large effective three-body interaction in a double-well optical lattice" [9]. The results of chapter 3 have been accepted for publication in Physical Review A in a paper is titled "Hubbard model for ultracold bosonic atoms interacting via zero-point-energy induced three-body interactions". The paper titled "Formation and decay of Bose-Einstein condensates in an excited band of a double-well optical lattice" [49] was published in Physical Review A and is based on chapter 4. A paper based on chapter 5 titled "Wannier function using a discrete variable representation for optical lattices" has been submitted to Physical Review A, and is currently being reviewed. I conclude in chapter 6.

Chapter 2

Three-body interaction in an optical lattice

2.1 Introduction

Ultracold atoms in optical lattices are highly tunable systems and are now increasingly used to simulate diverse quantum many-body Hamiltonians [1, 11]. In recent years, Hamiltonians with complex band structure have been experimentally realized, such as double-well lattices [2–5], honeycomb, triangular, one-dimensional stripe and Kagome lattices [6,7], and artificial graphene [8]. These experiments have extended the scope of the BH model to include excited bands and richer on-site interactions. Such Hamiltonians are being used to study collective phenomena ranging from modified quantum phases [16,61,62], topological matter [5,6,63,64], and to the formation of long-lived unconventional Bose-Einstein condensates in excited bands, which were theoretically studied in Refs. [40–42, 49] and observed in Refs. [46, 48].

Many-body Hamiltonians with three-body interactions are also being explored. Three-body interactions can lead to significantly modified quantum phases [18–20], and can yield Pfaffian-like ground states [21–24] that have promising uses in quan-

tum computation [25]. Following the proposals by Refs. [26–29], the first experiments confirmed the presence of weak effective three-body interactions in optical lattices [30–33]. These effective three-body interactions, due to the virtual transitions of atoms to higher bands, are smaller than the usual two-body interactions. Recent proposals have investigated ways to reduce the strength of this two-body term, thereby enhancing the role of three-body interactions. In fact, Ref. [34] by driving the lattice at rf frequencies and Ref. [35] by adding resonant radiation to couple internal states of an atom have proposed ways to turn off the two-body interaction altogether. It was shown in [36] that arrays of superconducting Josephson junctions can also mimic strong three-body interactions.

In this chapter we show that very strong effective three-body interactions can be created using optical lattice potentials with two local minima per unit cell. We study trapped atoms in a double-well optical lattice with three or less atoms per site, and show that over a wide range of lattice parameters, the on-site interactions can be described by an effective Hamiltonian of the form

$$H_{\text{eff}} = \sum_{m=1}^{3} \frac{1}{m!} \Gamma_m b^{\dagger m} b^m, \tag{2.1}$$

where $b^\dagger(b)$ are creation(annihilation) operators, and Γ_m represents the effective m-body interaction energy. We show that tuning the lattice parameters can create situations when $\Gamma_3 \gg \Gamma_2$, i.e., a system with a strong effective three-body interaction energy.

The remainder of this chapter is setup as follows. In Sec. 2.2 we introduce the double-well optical lattice potential and numerically obtain the band structure

and Wannier functions. We then introduce the multi-band BH Hamiltonian and calculate hopping and interactions parameters of this Hamiltonian. In Sec. 2.3 we perform a mean-field calculation to determine its phase diagram and discuss the Superfluid-Mott insulator transition. The effective Hamiltonian model is introduced in Sec. 2.4 and constructed in a three-step process. In Sec. 2.4.1 we discuss the initial step of obtaining a many-particle basis and energy levels for each unit cell. The effective Hamiltonian in a unit cell of the form (2.1) is determined in Sec. 2.4.2. We also show how Γ_3/Γ_2 can be optimized by tuning the lattice parameters. In Sec. 2.4.3 we study the coupling between the many-particle states in adjacent unit cells and introduce the effective tunneling Hamiltonian. We discuss the validity of the effective Hamiltonian by comparing the numerical mean-field results obtained for the effective Hamiltonian picture and the full BH Hamiltonian in Sec. 2.5. Finally, we summarize our results and present conclusions in Sec. 2.6.

2.2 Hamiltonian for the double-well optical lattice

We are interested in atoms in optical lattice potentials that have two nearly degenerate local minima in an unit cell. In particular, we focus on a lattice with a double-well structure along the x axis and single-well structure along the perpendicular y and z axes. Such a lattice can be constructed by using a laser with wave vector k_L and its first higher harmonic. We focus on

$$V(\vec{x}) = -V_0 \cos^2(k_L x) - V_1 \cos^2\left[2k_L(x+b)\right] - V_2\left[\cos^2(2k_L y) + \cos^2(2k_L z)\right], \quad (2.2)$$

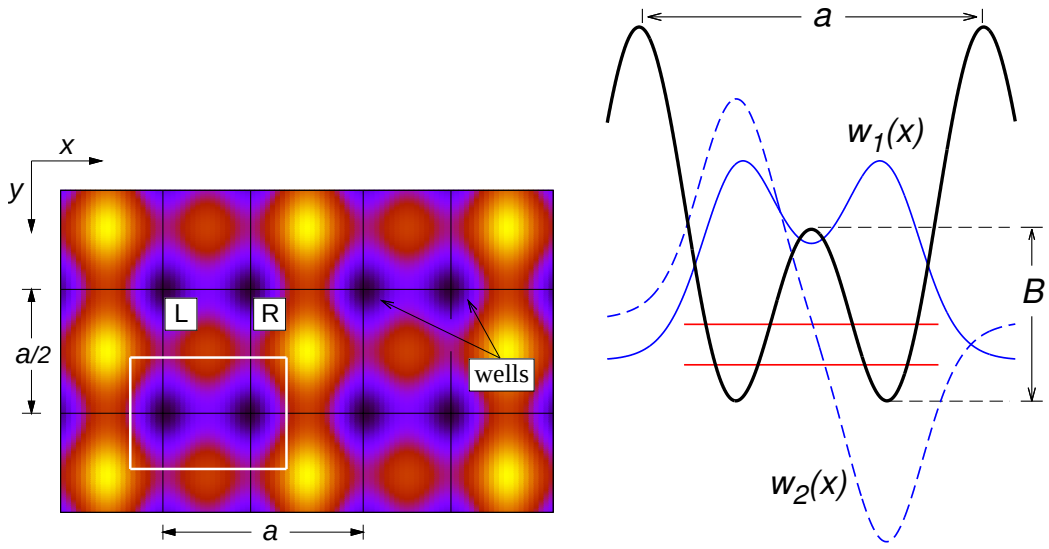

(a) (b)

Figure 2.1: (a) Contour plot of the optical lattice potential in the xy plane, where the potential minima are in dark blue. The white box encloses a unit cell of length a and $a/2$ along x and y, respectively. Each unit cell has a double well along the x axis, labeled L and R, and a single well along the y and z axes. (b) Schematic of a symmetric double-well potential (thick solid black curve) in a unit cell along the x axis. The barrier height between the left and right wells is B. The Wannier functions for the ground and first-excited band, $w_1(x)$ and $w_2(x)$, are shown as blue curves. They are computed for a lattice with $V_0/E_R = 17.0$, $V_1/V_0 = 1.3$, $V_2/E_R = 40.0$ and $bk_L = \pi/4$. The two horizontal red curves represent their energies with splitting δ.

where $V_{0,1,2}$ are lattice depths and b is a parameter that determines whether the lattice has a symmetric or asymmetric double-well. The lattice has a periodicity of $a = \pi/k_L$ along x axis, and $a/2$ along the perpendicular directions. Throughout, we express energies in units of the recoil energy along the x axis, $E_R = \hbar^2 k_L^2/2m_a$, where m_a is the atomic mass. We note that the recoil energy along the perpendicular directions is $E_{R,\perp} = 4E_R$. Figure 2.1a shows a contour plot of the optical-lattice potential in the xy plane, while Fig. 2.1b shows a symmetric double-well for $k_L b = \pi/4$ along the x axis.

In this chapter, we solely focus on the symmetric double-well lattice with $k_L b = \pi/4$ and allow the lattice depths to vary. The barrier height between the left and right wells is $B = (V_1 - V_0/4)^2/V_1$. The barrier disappears when $V_1/V_0 < 1/4$. In the limit $V_1/V_0 \to \infty$, the potential approaches a single-well potential with period $a/2$ along all directions. Some remarks about the case $k_L b \neq \pi/4$ are made at the end of Sec. 2.4.2.

The band structure and corresponding Bloch functions are obtained numerically. They are independently computed for the x, y and z directions and lead to a band dispersion $\epsilon_{\vec{\alpha}}(\vec{k}) = \epsilon_{x,\alpha_x}(k_x) + \epsilon_{y,\alpha_y}(k_y) + \epsilon_{z,\alpha_z}(k_z)$, where $\vec{\alpha} = (\alpha_x, \alpha_y, \alpha_z)$ are the band indices and $\vec{k}$ is the quasi-momentum in the first Brillouin zone. The lowest two bands, $\alpha_x = 1, 2$, along the x axis are quasi-degenerate for deep lattices. Along the perpendicular directions, the ground band $\alpha_y = \alpha_z = 1$ is far removed from the first excited band. The Wannier functions, labeled by unit cell $\mathbf{i} = (i_x, i_y, i_z)$ and $\vec{\alpha}$, are a product of one dimensional Wannier functions, one for each axis, i.e., $w_{\mathbf{i},\vec{\alpha}}(\vec{x}) = w_{\mathbf{i},\alpha_x}(x) w_{\mathbf{i},\alpha_y}(y) w_{\mathbf{i},\alpha_z}(z)$. These functions can be obtained

with the Marzari-Vanderbilt scheme [54] of constructing maximally localized Wannier functions. This was used for a double-well optical lattice in Ref. [17]. Here, we follow Refs. [8, 60] and Wannier functions are found as eigenstates of the position operators $\hat{x}$, $\hat{y}$ and $\hat{z}$ within the subspace of all the Bloch functions with band index $\vec{\alpha}$. To ensure real-valued Wannier functions, a real-valued discrete variable representation with periodic boundary conditions [65] over $\vec{M} = (M_x, M_y, M_z)$ unit cells is used. Figure 2.1b shows the Wannier functions $w_{\mathbf{i},\alpha_x}(x)$ for the lowest two bands along the x axis for a symmetric lattice. We see that the Wannier functions are exponentially suppressed between unit cells, but that they are extended over the barrier between the left and right well. This is typical for the lattice parameters that are the focus of this paper.

Since the lowest two bands along x axis are quasi-degenerate for deep lattices, we construct a multi-band Bose-Hubbard (BH) Hamiltonian H spanning the lowest two bands along the x axis, and only the ground band along the perpendicular directions. For simplicity, we drop the band indices $\alpha_y = \alpha_z = 1$, and use $\alpha = 1, 2$ to refer to the band index along the x axis. We find $H = \sum_{\mathbf{i}} \left\{ H^{\text{hop}}_{\mathbf{i}} + H^{\text{cell}}_{\mathbf{i}} \right\}$, where the nearest-neighbor hopping Hamiltonian is

$$H^{\text{hop}}_{\mathbf{i}} = -\sum_{\alpha\in 1,2} \left\{ J_\perp \left(a^\dagger_{\mathbf{i},\alpha} a_{\mathbf{i}+1_y,\alpha} + a^\dagger_{\mathbf{i},\alpha} a_{\mathbf{i}+1_z,\alpha} + h.c. \right) + J_\alpha \left(a^\dagger_{\mathbf{i},\alpha} a_{\mathbf{i}+1_x,\alpha} + h.c. \right) \right\}. \quad (2.3)$$

The operators $a^\dagger_{\mathbf{i},\alpha}$ and $a_{\mathbf{i},\alpha}$ create and annihilate a particle in the Wannier function of unit cell $\mathbf{i}$ and band $\alpha = 1, 2$, respectively. The abbreviation $h.c.$ is the hermitian conjugate. The location $\mathbf{i}+1_x$ denotes the unit cell (i_x+1, i_y, i_z). A similar notation is used for the other directions. The nearest-neighbor (NN) tunneling energy in band

α along the x axis is $J_\alpha = (1/M_x)\sum_{k_x}\cos(ka)\epsilon_{x,\alpha}(k_x)$, where the sum is over the M_x allowed quasi-momenta k_x. Along the perpendicular directions the NN tunneling energy in the ground band is $J_\perp$. There is no cross-tunneling between separate bands as the Wannier functions are orthogonal. We have not included next-nearest neighbor tunneling since our numerical computation show that they are nearly two orders of magnitude smaller than the NN tunneling for the lattice depths on which we focus in this paper.

The Hamiltonian $H_{\mathbf{i}}^{\text{cell}}$ for unit cell $\mathbf{i}$ is

$$H_{\mathbf{i}}^{\text{cell}} = \frac{\delta}{2}\left(\hat{n}_{\mathbf{i},2} - \hat{n}_{\mathbf{i},1}\right) + \frac{1}{2}\sum_{\alpha\in 1,2} U_\alpha \hat{n}_{\mathbf{i},\alpha}(\hat{n}_{\mathbf{i},\alpha} - 1) + 2U_{12}\hat{n}_{\mathbf{i},1}\hat{n}_{\mathbf{i},2} + \frac{1}{2}U_{12}\left(a_{\mathbf{i},1}^\dagger a_{\mathbf{i},1}^\dagger a_{\mathbf{i},2}a_{\mathbf{i},2} + a_{\mathbf{i},2}^\dagger a_{\mathbf{i},2}^\dagger a_{\mathbf{i},1}a_{\mathbf{i},1}\right), \tag{2.4}$$

where $\hat{n}_{\mathbf{i},\alpha} = a_{\mathbf{i},\alpha}^\dagger a_{\mathbf{i},\alpha}$ and the band-gap between bands $\alpha = 1$ and 2 is given by $\delta = (1/M_x)\sum_{k_x}\{\epsilon_{x,2}(k_x) - \epsilon_{x,1}(k_x)\}$. The on-site interaction terms U_1, U_2 and U_{12} are obtained from the local Wannier functions $w_{\mathbf{i},\alpha}$ by a numerical integration as $U_\alpha = g\int w_{\mathbf{i},\alpha}(\vec{x})w_{\mathbf{i},\alpha}(\vec{x})w_{\mathbf{i},\alpha}(\vec{x})w_{\mathbf{i},\alpha}(\vec{x})d\vec{x}$ and $U_{\alpha\beta} = g\int w_\alpha(\vec{x})w_\alpha(\vec{x})w_\beta(\vec{x})w_\beta(\vec{x})d\vec{x}$, where $g = 4\pi\hbar^2 a_s/m_a$ and a_s is the s-wave scattering length. As a consequence of the nature of the Wannier functions, the term U_{12} is comparable to U_1 and U_2 giving rise to strong density-density and pair-tunneling terms. It is the interplay between this pair-tunneling term and the band gap contribution that will enable us to achive a large effective three-body interaction.

For a symmetric double-well lattice, other atom-atom interaction terms between Wannier functions in bands 1 and 2 within a unit cell are strictly zero due to the parity of the Wannier functions. For small asymmetries, these other terms are

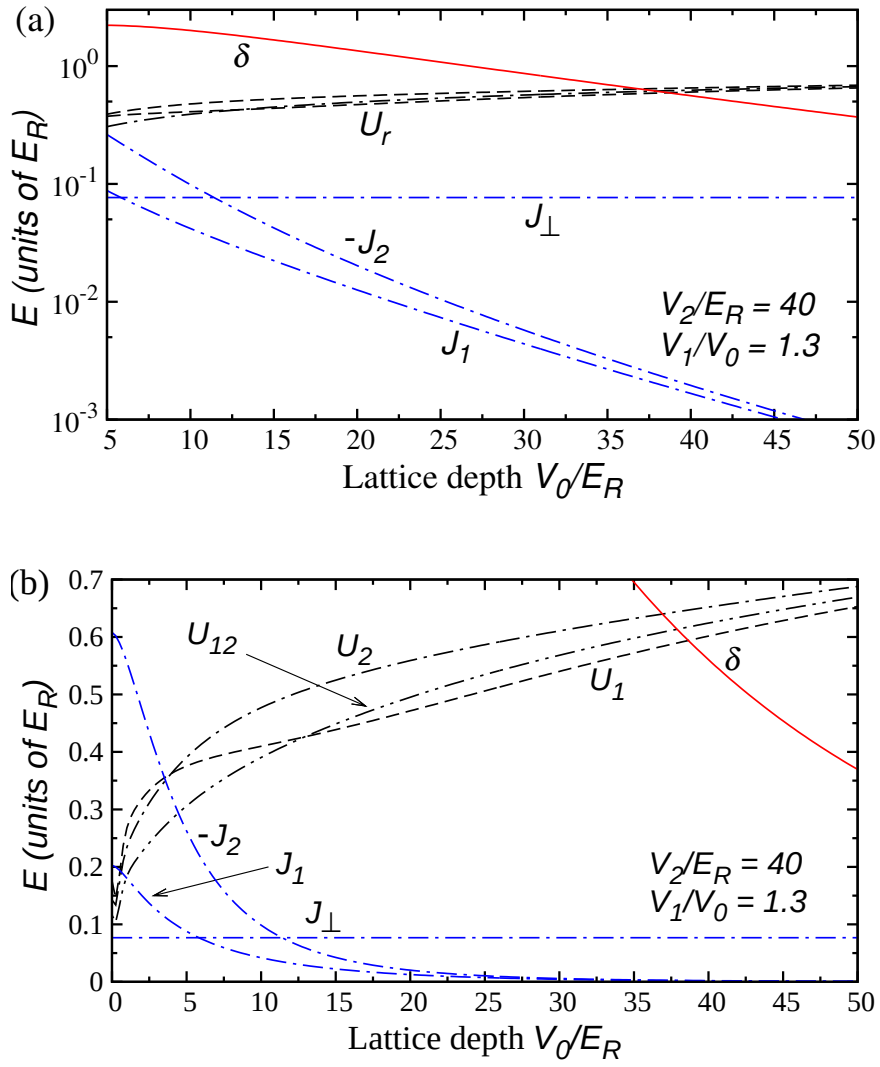

Figure 2.2: Numerical parameters for the BH Hamiltonian for ^{87}Rb on a log-linear scale (a) and linear-linear scale (b) plotted as functions of lattice depth V_0 in units of E_R, at $V_1/V_0 = 1.3$, $V_2/E_R = 40.0$ and $bk_L = \pi/4$. The tunneling energies $J_1, -J_2$ and $J_\perp$ are shown as dot-dashed blue curves. The band-gap δ is plotted as a solid red curve. The interaction energies $U_r = U_1, U_2$ and U_{12} are shown as dashed black curves. They are calculated for a scattering length of $a_s = 100a_0$, where $a_0 = 0.0529\,\text{nm}$ is the Bohr radius.

small and can be neglected. Finally, we have not included terms due to atom-atom interactions between Wannier functions in neighboring unit cells, because they are an order of magnitude or more smaller than those in Eq. (2.4).

Figures 2.2a and 2.2b show parameters of the BH Hamiltonian as a function of lattice depth V_0 for ^{87}Rb atoms at a fixed ratio of V_1/V_0 and fixed V_2. The plot shows that the interaction energies U_1, U_2 and U_{12} are of equal importance, satisfy $U_2 > U_{12} > U_1$, and are of the order of the band gap δ. The tunneling energies are much smaller than the interaction energies. The tunneling energy J_2 for band 2, as expected, is negative and $|J_2| > |J_1|$. Our choice of $V_2/E_R = 40.0$ is such that, as shown in the next section, our Hubbard Hamiltonian has a superfluid region.

2.3 Phase diagram using decoupling approximation

In this section, we obtain the mean-field phase diagram for the BH Hamiltonian. A knowledge of the quantum phases as a function of lattice parameters is essential to prepare the system in the required many-body ground state. In addition, the results will be used in Sec. 2.5 to discuss the validity of the effective Hamiltonian model. The phase diagram is obtained in the mean-field decoupling approximation [13] by introducing a real-valued homogeneous superfluid order parameter for each band $\alpha = 1, 2$, i.e., $\psi_\alpha = \langle a^\dagger_{\mathbf{i},\alpha} \rangle = \langle a_{\mathbf{j},\alpha} \rangle$ and approximate $a^\dagger_{\mathbf{i},\alpha} a_{\mathbf{j},\alpha}$ by $\psi_\alpha \left(a^\dagger_{\mathbf{i},\alpha} + a_{\mathbf{j},\alpha} \right) - \psi^2_\alpha$ for $\mathbf{i} \neq \mathbf{j}$. In the grand-canonical ensemble, this leads to the grand-canonical potential or Hamiltonian $H^{\mathrm{MF}} = \sum_{\mathbf{i}} (H^{\mathrm{MF}}_{\mathbf{i}} - \mu a^\dagger_{\mathbf{i},\alpha} a_{\mathbf{i},\alpha})$, where

$$H^{\mathrm{MF}}_{\mathbf{i}} = H^{\mathrm{cell}}_{\mathbf{i}} - \sum_{\alpha \in 1,2} \left(a^\dagger_{\mathbf{i},\alpha} + a_{\mathbf{i},\alpha} \right) (2J_\alpha + z_\perp J_\perp) \psi_\alpha + \sum_{\alpha \in 1,2} (2J_\alpha + z_\perp J_\perp) \psi^2_\alpha \qquad (2.5)$$

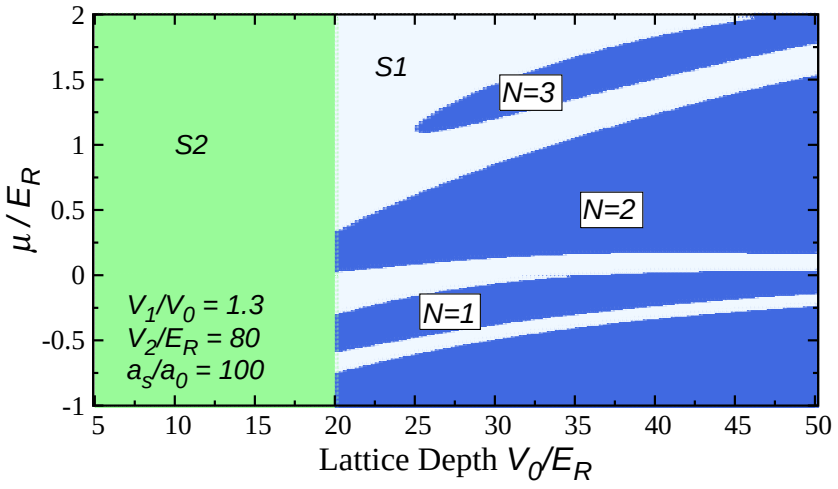

Figure 2.3: Phase diagram for ^{87}Rb in a symmetric double-well lattice as a function of lattice depth V_0 in units of E_R at $V_2/E_R = 80.0$, $V_1/V_0 = 1.3$ and scattering length $a_s = 100a_0$. The dark blue lobes are the Mott lobes for $N = 1, 2$ and 3 atoms per unit cell. All other regions represent SF phases, with $S1$ denoting the case $\psi_1 \neq 0, \psi_2 = 0$ and $S2$ denoting $\psi_2 \neq 0$, $\psi_1 = 0$.

and $z_\perp$ is the number of neighboring unit cells along the perpendicular directions. In our case, $z_\perp = 4$. The ground state of the grand-canonical potential H^{MF} at a given chemical potential μ corresponds to order parameters (ψ_1, ψ_2) that minimize its ground state energy. We have performed these calculations in a basis of Fock states $|n_1, n_2\rangle$, where n_α is the number of atoms in band α in an unit cell. We reach numerical convergence for $n_1, n_2 \leq N_{\max} = 10$. A Mott insulator (MI) state corresponds to $\psi_1 = \psi_2 = 0$, while a superfluid (SF) state is obtained when either $\psi_1, \psi_2 \neq 0$.

Figure 2.3 shows the mean-field phase diagram for our symmetric double-well lattice. The figure shows Mott lobes up to $N = 3$ atoms per unit cell. We find

that the Mott lobes with odd N are reduced in size compared to adjacent lobes with even N, a feature also noted and discussed in [62]. For the SF phase $S1$, the order parameter $\psi_1 \neq 0$, but $\psi_2 = 0$, while for the SF phase $S2$ $\psi_2 \neq 0$ but $\psi_1 = 0$. Both the order parameters have a jump at the $S1$-$S2$ phase-boundary corresponding to a first-order phase transition. For the relatively shallow depths used in all directions in Fig. 2.3, superfluidity extends over all dimensions. For larger depths along either x or y and z, the superfluid can be localized to fewer dimensions. A further stability analysis around the mean-field solution is then required to identify this distinction [66–68]. Such knowledge, however, is not crucial for deriving the effective Hamiltonian model.

A cutting off of the Mott lobes for $N = 1$ and 2 at the phase-boundary to phase $S2$ is apparent in Fig. 2.3. From a separate analytical calculation of the phase-boundary of H^{MF}, excluding the interaction induced pairing terms, we find that this cut-off occurs when $2J_2 + z_\perp J_\perp = 0$. For the lattice parameters used in Fig. 2.3 this occurs when $V_0/E_R \approx 20$, consistent with our numerical simulations including the pairing term.

The lattice parameters in Fig. 2.3 were particularly chosen so as to have a good representation of all the three quantum phases. Since our primary aim in this paper is to show the presence of large effective three-body interactions in double-well optical lattices, we do not provide phase diagrams for a wider set of lattice parameters. Instead, we note that in our case, we are mainly interested in the phase $S1$ and the corresponding SF-Mott phase-boundary. Also, the region $S1$ grows relative to those of other phases as we decrease the lattice depth along the

perpendicular directions.

2.4 Effective Hamiltonian

We now show that the low energy states of the multi-band BH Hamiltonian defined in Eqs. (2.3) and (2.4) can be obtained from an effective Hamiltonian H_{eff} that has strong three-body interactions. Constructing H_{eff} is a three-step process. The first step is discussed in Sec. 2.4.1 and involves diagonalizing the on-site Hamiltonian $H_{\mathbf{i}}^{\text{cell}}$ in unit cell $\mathbf{i}$ to obtain many-particle (MP) energy levels. Using these MP levels an effective on-site interaction Hamiltonian is constructed in Sec. 2.4.2. Finally, in Sec. 2.4.3 we calculate the effective tunneling Hamiltonian that couples the MP states of adjacent unit cells.

2.4 Many-particle energy levels

We are interested in lattice parameters for which the average band gap δ and interaction energies U_1, U_2 and U_{12} are much larger than the tunneling energies J_1, J_2 and $J_\perp$. We thus diagonalize the on-site Hamiltonian $H_{\mathbf{i}}^{\text{cell}}$ in the Fock state basis $|n_1, N-n_1\rangle$ for N atoms in unit cell $\mathbf{i}$ with n_1 atoms in band $\alpha = 1$. This gives the many-particle (MP) eigenenergies $\mathcal{E}_N^{(\nu)}$ and eigenstates $|\nu, N\rangle$ with $\nu = \{1, \ldots, N+1\}$. We refer to these ν states as vibrational states. The MP eigenstates in terms of the Fock states are

$$|\nu, N\rangle = \sum_{n_1=0}^{N} \mathcal{C}_{n_1}^{(\nu)}(N)|n_1, N-n_1\rangle, \tag{2.6}$$

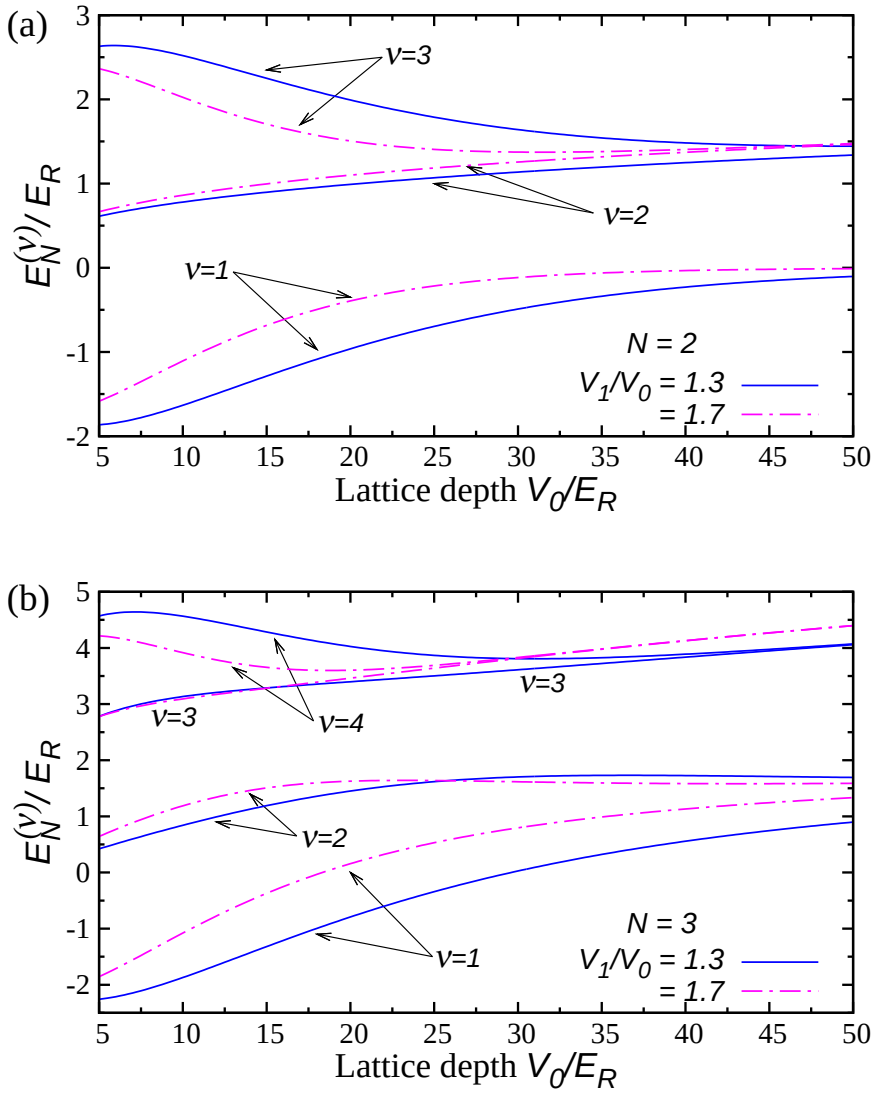

Figure 2.4: (a) Many-particle energy levels $\mathcal{E}_N^{(\nu)}$ for two atoms per unit cell, as functions of lattice depth V_0 in units of E_R. The solid blue lines are for $V_1/V_0 = 1.3$, while the dot-dashed magenta curves are for $V_1/V_0 = 1.7$. (b) Similar plot for three atoms per unit cell. Plots are for ^{87}Rb in a symmetric lattice with $V_2/E_R = 40.0$ and scattering length $a_s = 100a_0$.

with real coefficients $\mathcal{C}_n^{(\nu)}(N)$. It is good to note that the many-body ground state of the Hamiltonian in Eq. (2.3) in a Mott lobe is a product of $|\nu, N\rangle$ states with $\nu = 1$, one for each site.

For $N = 1$ the eigenstates are simply the Fock states $|1, 0\rangle$ and $|0, 1\rangle$ with energy $\mathcal{E}_1^{(1)} = -\delta/2$ and $\mathcal{E}_1^{(2)} = \delta/2$. A plot of the band gap δ as a function of lattice depth V_0 is shown in Fig. 2.2a. Figures 2.4a and 2.4b show the MP energy levels $\mathcal{E}_N^{(\nu)}$ as a function of lattice depth V_0 and at fixed V_1/V_0 and V_2 for two and three atoms, respectively. Their behavior can be understood by noting that the band gap δ decreases with increasing lattice depth V_0, and for larger depths $\delta/U \ll 1$ with $U \approx U_1 \approx U_2 \approx U_{12}$. Consequently, we can show using perturbation theory that for $N = 2$, $\mathcal{E}_2^{(1)} = -\delta^2/(2U)$, $\mathcal{E}_2^{(2)} = 2U$ and $\mathcal{E}_2^{(3)} = 2U + \delta^2/(2U)$. For $N = 3$ atoms, $\mathcal{E}_3^{(1)} = 2U - \delta - 3\delta^2/6U$, $\mathcal{E}_3^{(2)} = 2U + \delta - 3\delta^2/6U$, and $\mathcal{E}_3^{(3)} = \mathcal{E}_3^{(4)} = 6U + 3\delta^2/6U$. In conjunction with Fig. 2.2b these expressions give a fair estimate of $\mathcal{E}_N^{(\nu)}$ for large V_0. We also note that the energy of the ground-vibrational $\nu = 1$ state is well separated from that of the state $\nu = 2$ with a spacing much larger than J_1, J_2 or $J_\perp$. For the effective Hamiltonian picture, we assume that the atoms only populate the $\nu = 1$ states.

We should further note that interactions in Eq. (2.4) mix the Fock states $|n_1, N - n_1\rangle$ and the vibrational ground states $|\nu = 1, N\rangle$ at large lattice depths have considerable contribution from Fock states with atom population in the first excited band.

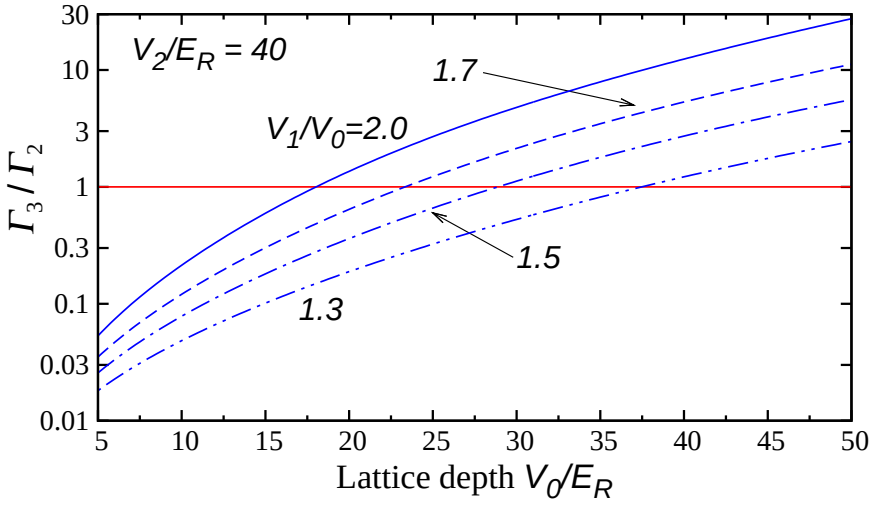

Figure 2.5: Log-linear plot of the ratio of three- to two-body interaction strength Γ_3/Γ_2 as a function of lattice depth V_0 in units of E_R for various ratios of V_1/V_0. The horizontal red line denotes $\Gamma_3/\Gamma_2 = 1$. The plot is for ^{87}Rb in a symmetric lattice at $V_2/E_R = 40.0$ and scattering length $a_s = 100a_0$.

2.4 Effective interaction Hamiltonian

We can now construct the effective on-site interaction Hamiltonian similar to Eq. (2.1) in unit cell $\mathbf{i}$ based on the large energy separation between the $\nu = 1$ and 2 vibrational states for each N. In other words we assume that the atoms only populate the ground vibrational states with energies $\mathcal{E}_N^{(1)}$ that are reproduced by the effective on-site interaction Hamiltonian

$$H_{\rm eff}^{\rm int} = \sum_{\mathbf{i}} \sum_{m=1}^{3} \frac{1}{m!} \Gamma_m b_{\mathbf{i}}^{\dagger m} b_{\mathbf{i}}^{m}, \tag{2.7}$$

where $b_{\mathbf{i}}$ and $b_{\mathbf{i}}^{\dagger}$ are effective bosonic annihilation and creation operators for unit cell $\mathbf{i}$ and state $\nu = 1$. The coefficients Γ_m are the $m-$body interaction strengths, which we restrict to $m \leq 3$, and are found by mapping $\mathcal{E}_N^{(1)}$ to the eigenenergies of $H_{\rm eff}^{\rm int}$.

Some algebra shows $\Gamma_1 = \mathcal{E}_1^{(1)}$, $\Gamma_2 = \mathcal{E}_2^{(1)} - 2\mathcal{E}_1^{(1)}$ and $\Gamma_3 = \mathcal{E}_3^{(1)} - 3(\mathcal{E}_2^{(1)} - \mathcal{E}_1^{(1)})$.

Figure 2.5 shows Γ_3/Γ_2 as a function of lattice depth V_0 for various V_1/V_0. We observe that Γ_3/Γ_2 increases with V_0 and V_1/V_0, i.e. with increasing lattice depth. In fact, choosing appropriate lattice parameters can produce a three-body strength that is larger than the two-body one. Using the same approximations as used in Sec. 2.4.1 for large lattice depths, we find $\Gamma_2 \approx \delta - \delta^2/(2U) + \mathcal{O}(\delta^3)$ and $\Gamma_3 \approx 2U - 2.5\delta + 1.3\delta^2 + \mathcal{O}(\delta^3)$. Consequently, δ and $\Gamma_2 \to 0$ while Γ_3 remains finite for larger lattice depths and $\Gamma_3 \gg \Gamma_2$.

For an asymmetric double-well lattice with $k_L b \neq \pi/4$, δ and equivalently Γ_2 depend on the asymmetry and remain finite for a large lattice depth. A symmetric lattice is therefore the most favorable case with which to reach sizeable Γ_3. We should also note that it is not possible to obtain $\Gamma_2 \ll \Gamma_3$ for a single-well lattice since the band gap increases with lattice depth.

2.4 Effective tunneling Hamiltonian

In this section we study the coupling between the MP states $|\nu, N\rangle$ of neighboring unit cells. Since tunneling involves two adjacent unit cells, we label states as $|\nu, N\rangle_{\mathbf{i}}|\nu', M\rangle_{\mathbf{i}+1}$, where N and M are the atom numbers in unit cell $\mathbf{i}$ and $\mathbf{i}+1_x$, $\mathbf{i}+1_y$ or $\mathbf{i}+1_z$, respectively. As in the previous subsection, we restrict our discussion to the $\nu = 1$ ground state and simply write the initial and final states as $|N, M; \mathbf{i}, \mathbf{i}+1\rangle\rangle \equiv |\nu = 1, N\rangle_{\mathbf{i}}|\nu' = 1, M\rangle_{\mathbf{i}+1}$.

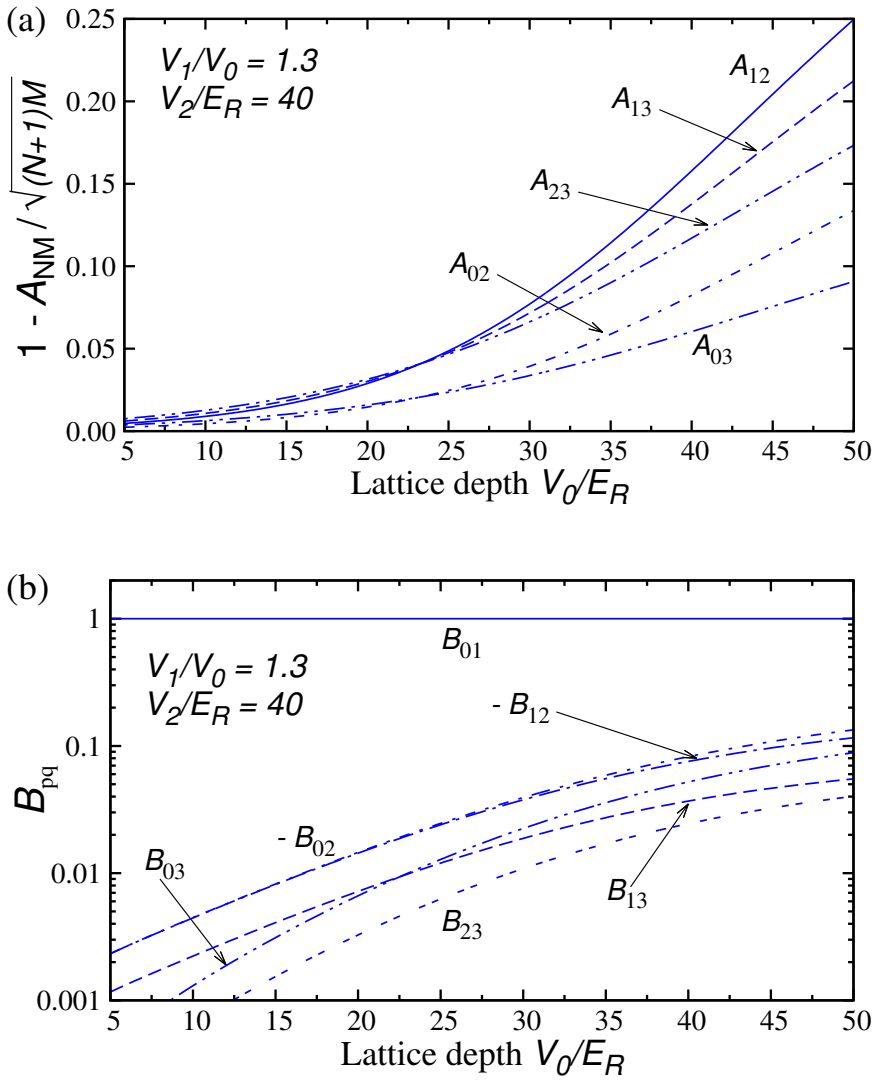

Figure 2.6: (a) Plot of ratio $1 - \mathcal{A}_{NM}/\sqrt{(N+1)M}$ as a function of lattice depth V_0. The coefficient $\mathcal{A}_{01}$ is not shown because the corresponding ratio is zero. (b) Plot of $\mathcal{B}_{pq}$ as a function of lattice depth V_0. Both the panels are for ^{87}Rb with $k_L b = \pi/4$, $V_1/V_0 = 1.3$, $V_2/E_R = 40.0$ and $a_s = 100a_0$.

With these definitions we can express nearest-neighbor tunneling along x axis,

$$H^{\rm hop}_{x,\rm eff} = -J_1 \sum_{\mathbf{i}} {\sum_{N,M}}' \Big\{ \mathcal{A}_{NM} |N+1, M-1; \mathbf{i}, \mathbf{i}+1_x\rangle\rangle\langle\langle N, M; \mathbf{i}, \mathbf{i}+1_x| + h.c. \Big\}, \quad (2.8)$$

where $0 \leq N < M$, and using Eqs. (2.3) and (2.6),

$$\begin{aligned} -J_1 \mathcal{A}_{NM} &= \langle\langle N+1, M-1; \mathbf{i}, \mathbf{i}+1_x | H^{\rm hop}_{\mathbf{i}} | N, M; \mathbf{i}, \mathbf{i}+1_x\rangle\rangle \quad (2.9) \\ &\approx -J_1 \sum_{n=0}^{N} \sum_{m=1}^{M} \sqrt{(n+1)m}\, \mathcal{C}^{(1)}_n(N)\, \mathcal{C}^{(1)}_{n+1}(N+1) \mathcal{C}^{(1)}_m(M)\, \mathcal{C}^{(1)}_{m-1}(M+1), \end{aligned}$$

are unit-cell-independent dimensionless real coefficients. Here, we only include tunneling through the term proportional to J_1 in Eq. (2.3), since the $\nu = 1$ vibrational level is predominantly determined by the $|N, 0\rangle$ Fock state. Thus, the contribution from tunneling through the J_2 term is negligible. We limit ourselves to $N, M \leq 3$, i.e. up to three atoms per site, and only require the six independent $\mathcal{A}_{01}$, $\mathcal{A}_{02}$, $\mathcal{A}_{12}$, $\mathcal{A}_{03}$, $\mathcal{A}_{13}$ and $\mathcal{A}_{23}$. In Fig. 2.6a we plot the ratio $1-\mathcal{A}_{NM}/\sqrt{(N+1)M}$ for these six coefficients as a function of lattice depth V_0. The expression $\sqrt{(N+1)M}$ corresponds to the coefficient expected for a simple single-well BH Hamiltonian. The coefficients $\mathcal{A}_{NM}$ deviate only slightly from these values for $V_0/E_R < 30$ in Fig. 2.6a. More generally, we find that the correction becomes larger for larger lattice depth.

The effective tunneling Hamiltonian $H^{\rm hop}_{x,\rm eff}$ has atom-number dependent parameters. We find it convenient to write $H^{\rm hop}_{x,\rm eff}$ in an alternative form as a sum of multi-body hopping operators

$$H^{\rm hop}_{x,\rm eff} = -J_1 \sum_{\mathbf{i}} {\sum_{q,p}}' \Big\{ \mathcal{B}_{pq} \left(b^\dagger_{\mathbf{i}}\right)^{p+1} \left(b^\dagger_{\mathbf{i}+1_x}\right)^{q-1} (b_{\mathbf{i}})^p \, (b_{\mathbf{i}+1_x})^q + h.c. \Big\}, \quad (2.10)$$

where the sums over p and q are restricted to $0 \leq p < q$. An m-body hopping operator corresponds to terms where $p+q=m$. The six coefficients $\mathcal{B}_{pq}$ are found

from solving the linear system

$$\mathcal{A}_{NM} = \sum_{q=1}^{3} \sum_{p=0}^{q-1} \mathcal{B}_{pq} \mathcal{F}(N, M, p, q), \text{ with } \mathcal{F}(N, M, p, q) = \frac{\sqrt{(N+1)M}(M-1)!N!}{(M-q)!(N-p)!}.$$

Figure 2.6b shows a plot of $\mathcal{B}_{pq}$ as a function of lattice depth V_0. The most important term is $\mathcal{B}_{01} = 1$, the usual single-particle tunneling term between adjacent unit cells. The next two leading terms are the two- and three-body operators with strength $\mathcal{B}_{02}$ and $\mathcal{B}_{12}$, respectively. Their values are negative. Other terms are a factor of two or more smaller and positive.

Figure 2.4b shows that the energy separation between the $\nu = 1$ and 2 vibrational states for $N = 3$ atoms decreases with increasing ratio V_1/V_0. This might seem to invalidate the assumption that the atoms only populate the ground vibrational state for larger lattice depths. For such a scenario with large V_1/V_0, however, we can choose a smaller lattice depth V_0 to ensure that the ground vibrational state is well separated, and still have a large $\Gamma_3 > \Gamma_2$. Moreover, the coupling between the ground and excited vibrational states in neighboring unit cells are of the order of the tunneling energies with strength proportional to $J_1^2/\sqrt{U^2 + \delta^2}$, which decrease with increasing V_1/V_0, and stay much smaller than the energy separation between the ground and excited vibrational states.

The effective tunneling Hamiltonians along perpendicular directions are obtained by replacing J_1 by $J_\perp$. The numerical values for the coefficients $\mathcal{B}_{pq}$ are the same as those along the x axis. This finally leads to the effective tunneling Hamiltonian $H_{\text{eff}}^{\text{hop}} = H_{x,\text{eff}}^{\text{hop}} + H_{y,\text{eff}}^{\text{hop}} + H_{z,\text{eff}}^{\text{hop}}$ and the total effective Hamiltonian $H_{\text{eff}} = H_{\text{eff}}^{\text{int}} + H_{\text{eff}}^{\text{hop}}$.

2.5 Validity of the effective Hamiltonian

In this section, we discuss the validity of the effective Hamiltonian developed in Sec. 2.4. It was obtained by assuming that the atoms only occupy the ground vibrational ($\nu = 1$) states and coupling to excited ν states is negligible. This assumption is justified as the energy gap between the ground and excited vibrational states (see Figs. 2.4a and 2.4b) is much larger than the coupling strengths, which are of the order of the tunneling energies. We now verify this assumption further by comparing mean-field phase diagrams.

For our purposes it is sufficient to further simplify H_{eff} to

$$H_{\text{eff}} = \sum_{\mathbf{i}} \left\{ \sum_{m=1}^{3} \frac{1}{m!} \Gamma_m b_{\mathbf{i}}^{\dagger m} b_{\mathbf{i}}^{m} - J_1 b_{\mathbf{i}}^{\dagger} b_{\mathbf{i}+1_x} - J_\perp \left(b_{\mathbf{i}}^{\dagger} b_{\mathbf{i}+1_y} + b_{\mathbf{i}}^{\dagger} b_{\mathbf{i}+1_z} \right) + h.c. \right\}, \quad (2.11)$$

where we have only kept the leading-order single-body tunneling terms in Eq. (2.10). Thus, H_{eff} is a single-band BH Hamiltonian with an added effective three-body term proportional to Γ_3. Similar to Sec. 2.3, we introduce a real order parameter $\psi = \langle b_{\mathbf{i}} \rangle = \langle b_{\mathbf{i}}^{\dagger} \rangle$ and determine the ground-state energy, E_g, for the corresponding mean-field Hamiltonian in the grand-canonical ensemble by self-consistently minimizing the energy with respect to the order parameter ψ.

We first confirm that H_{eff} is a good model for lattice parameters where the full Hamiltonian in Eqs. (2.3) and (2.4) has a superfluid ground state in the $S1$ region. Figure 2.7a compares the ground-state energy E_g of the full mean-field and the effective Hamiltonian as a function of lattice depth V_0 for various values of μ. This graph is computed for $V_2/E_R = 40$, half the size used in Fig. 2.3. The mean-field

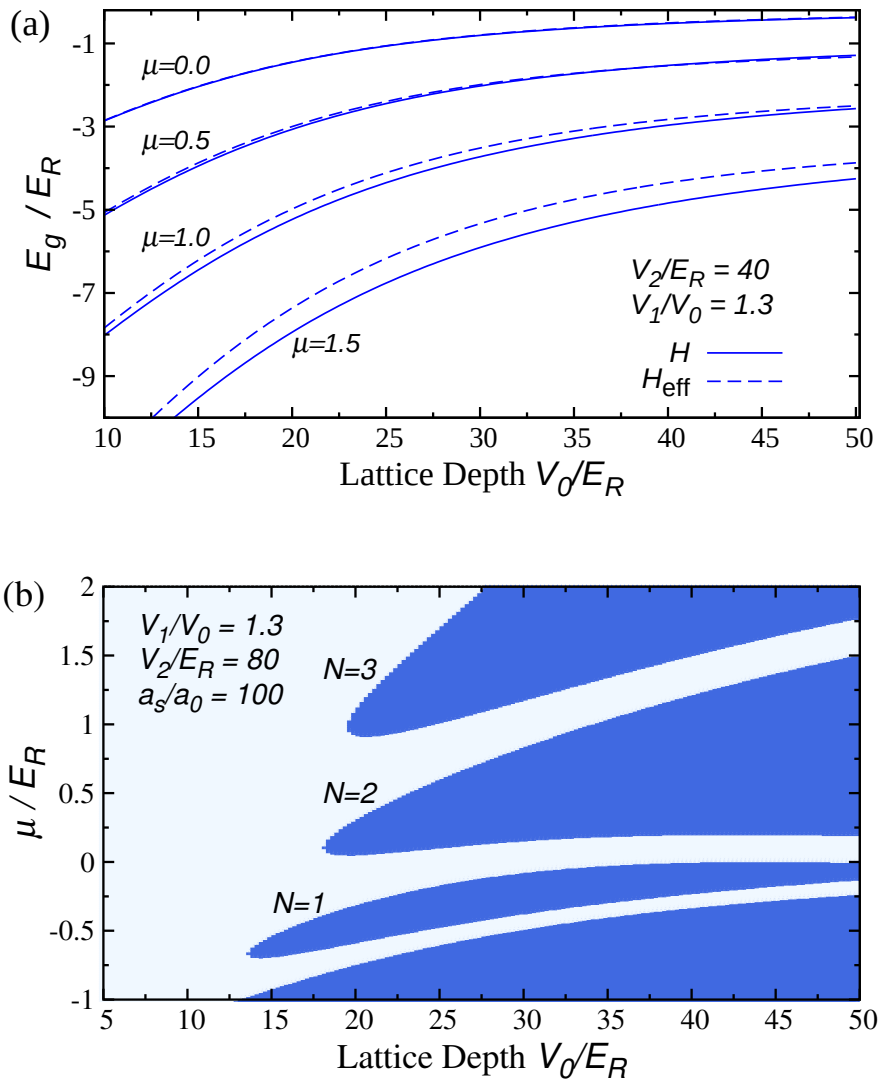

Figure 2.7: (a) Plot of the mean-field ground-state energy E_g as a function of lattice depth V_0 in units of E_R and $V_2/E_R = 40$ for different chemical potentials μ. The solid lines represent the results for the full Hamiltonian, while the dashed lines show those for the effective Hamiltonian. Lattice parameters are chosen such that the system is in the SF region $S1$. (b) Mean-field SF-Mott phase diagram for H_{eff} as a function of lattice depth V_0/E_R at $V_2/E_R = 80$. The deep blue areas are Mott lobes surrounded by a SF region. Other parameters are the same as those used in Fig. 2.3

.

ground state of the full Hamiltonian is then in the $S1$ region, with order parameter $\psi_2 = 0$, for the entire parameter space (μ, V_0) shown in Fig. 2.7a. Similarly, the ground state of the effective Hamiltonian is superfluid. The mean atom number per unit cell for the four values of the chemical potential, μ, shown in Fig. 2.7a are $\bar{n} = 1.56$, 2.37, 3.19 and 4.01 at a lattice depth of $V_0/E_R = 30$, respectively.

The ground-state energies for the two models show similar trends, have differences that are nearly independent of V_0 and agree better for smaller chemical potentials. The larger discrepancy for larger $\bar{n}$ is not due to virtual excitations to higher ν vibrational states or $m > 1$ hopping terms since $J_1\mathcal{B}_{pq}$ or $J_\perp\mathcal{B}_{pq}$ with $p, q \neq 0, 1$ are much smaller than the recoil energy. For $\bar{n} > 3$ we need to include four- or higher-body interaction terms to get better agreement.

Next, we study whether H_{eff} is valid as we approach the SF-Mott phase-boundary. Unlike the ground state energy, the mean-field phase boundary can be analytically obtained within second-order perturbation theory [13], treating $-(2J_1 + z_\perp J_\perp)\left(b_{\mathbf{i}}^\dagger + b_{\mathbf{i}}\right)\psi$ as a perturbation, and is given by

$$0 = J_{\text{eff}}\left\{1 + \frac{(g+1)J_{\text{eff}}}{-\Gamma_1 + \frac{1}{2}g(\Gamma_3 - 2\Gamma_2) - \frac{1}{2}g^2\Gamma_3 + \mu} + \frac{gJ_{\text{eff}}}{(\Gamma_3 - \Gamma_2 + \Gamma_1) + \frac{1}{2}g(2\Gamma_2 - 3\Gamma_3) + \frac{1}{2}g^2\Gamma_3 - \mu}\right\},$$

with $J_{\text{eff}} = (2J_1 + z_\perp J_\perp)$ and the Fock state $|g\rangle$ is the zeroth-order ground state of the grand-canonical potential. Figure 2.7b shows the corresponding SF-Mott phase diagram for $V_2/E_R = 80$ and can thus be directly compared with the phase diagram shown in Fig. 2.3 for the full Hamiltonian. For $V_0/E_R > 20$ the Mott lobes for $N = 0$, 1 and 2 are nearly identical. The $N = 3$ lobe for the effective Hamiltonian,

however, is significantly larger than that of the full Hamiltonian. In fact, the tip of the Mott lobe has shifted to smaller lattice depth. We have to include Γ_4 to correctly model this lobe. Finally, our effective Hamiltonian does not describe $S2$ for $V_0/E_R < 20$. In this phase, the full Hamiltonian has a non-zero order parameter in the second band. Our effective Hamiltonian assumes no population in the second band and can not represent these states.

2.6 Conclusion

We have shown that the low energy states of a system of trapped atoms in a double-well optical lattice can emulate a Hubbard model with strong three-body interactions. The optical lattice with a double-well potential along one direction and single period lattice along the remaining directions has two nearly degenerate bands. The Hamiltonian has a strong pair-tunneling contribution between the two Wannier functions within a unit cell. The interplay between this interaction and the band gap plays an important role in determining the behavior of the system. In particular, we find that the low energy states of such a system are quite accurately described by an effective single-band Hamiltonian with a strong three-body interaction, whose strength can be easily tuned by changing the lattice parameters. Surprisingly, tunneling between the neighboring unit cells in the effective Hamiltonian has, to good approximation, the same structure as that for a particle hopping in a single-band BH model. By comparing the numerically obtained ground state energy and phase diagram of the full and effective Hamiltonians, we verified that

the effective Hamiltonian model is an excellent approximation over a wide range of lattice parameters, both in the superfluid and Mott insulator phases.

Chapter 3

Hubbard model for ultracold bosonic atoms interacting via zero-point-energy induced three-body interactions

In 1998 Jaksch *et al.* [69] suggested that laser-cooled atomic samples can be held in optical lattices, periodic potentials created by counter-propagating laser beams. These three-dimensional lattices have spatial periods between 400 nm and 800 nm and depths V_0 as high as $V_0/h \sim 1$ MHz, where h is Planck's constant. An ensemble of atoms then realize either the fermionic or bosonic Hubbard model, where atoms hop from site to site and interact only when on the same site. The interaction driven quantum phase transition of this model was first realized by Ref. [70].

Today, optical lattices are seen as a natural choice in which to simulate other many-body Hamiltonians. These include Hamiltonians with complex band structure such as double-well lattices [71–74], two-dimensional hexagonal lattices [74–77], as well as those with spin-momentum couplings possibly leading to topological matter [78, 79]. Quantum phase transitions in these Hamiltonians enable ground-state

wavefunctions with unusual order parameters, such as pair superfluids and striped phases [80–82]. Phase transitions in Hamiltonians with long-range dipole-dipole interactions using atoms or molecules with large magnetic or electric dipole moments can also be studied. Finally, atoms in optical lattices can be used to measure gravitational acceleration (little-g) [83–85], shed light on non-linear measurements [86–89], and be used for quantum information processing.

Over the last ten years ultra-cold atom experiments have also investigated few-body phenomena. In particular, three-body interactions have been studied through Efimov physics of strongly interacting atoms observed as resonances in three-body recombination, where three colliding atoms create a dimer and a free atom [37,90,91]. Here, recent developments include the prediction of a minimum in the recombination rate coefficient K_3 for scattering of a van-der-Waals potential with a d-wave shape resonance [92]. Moreover, Ref. [93] presented advanced numerical simulations that can quantitatively model observed recombination rates, while Ref. [94] showed empirically that for a broad ^{7}Li Feshbach resonance, K_3 is controlled by the effective range correction of the atom-atom scattering.

Proposals that suggest ways to create atomic gasses dominated by elastic three-body interactions have also been made. In Refs. [95,96] this was achieved by adding resonant radiation to couple internal states of an atom or by driving the lattice at rf frequencies. Some of us showed that the low-energy behavior of atoms in complex lattice geometries (i.e. double-well optical lattices) can also be engineered to lead to large three-body interactions [97]. Interestingly, after the observation of the formation of droplets [98] in a ferromagnetic atomic dysprosium condensate

induced by a rapid quench to attractive pair-wise interactions Refs. [99, 100] have independently suggested that the origin of this instability are large repulsive elastic three-body collisions

In this chapter I propose a novel way to create dominant three-body interactions in Hubbard models. I rely on two ingredients. The first relies on the analytical analysis of scattering from a van-der-Waals potential [101, 102] as well as analytical modeling of Fano-Feshbach resonances, where the energy of molecular states is tuned with a magnetic-field [103]. This analysis confirms that ultra-cold scattering is describable in terms of a scattering length a and effective range r_e that are uniquely specified by the van-der-Waals coefficient and resonance parameters. The second ingredient is the realization that two-, three-, and higher-body interaction energies of atoms in an optical lattice site can under certain assumptions be computed analytically [104, 105].

We will show that for two atoms in a lattice site, with a non-negligible zero-point energy, a cancellation of the contribution from the scattering length and effective range contribution can occur while simultaneously three atoms have a finite inseparable three-body interaction that is of sufficient magnitude that an experimental observation is possible.

This chapter is organized as follows. In section 3.1 we introduce delta-function interactions between atoms with strength defined by the scattering length and effective range and review results for the ground-state energy of a few atoms held in a site of an optical lattice. We also examine the quality of a harmonic approximation of the lattice site potential. In Sec. 3.2 we derive the relationship between

a and r_e for which the two-body interactions cancel and three-body interactions remain. Sections 3.3 and 3.4 describe how this relationship can be met for a van-der-Waals potential and for Feshbach resonances, respectively. For scattering from a van-der-Waals potential we show that the ^{88}Sr isotope is a promising candidate. For Feshbach resonances we work out four cases, one each for ^{23}Na, ^{39}K, ^{52}Cr, and ^{133}Cs scattering. We also compare the expected three-body interaction energies with tunneling energies between lattice sites. Section 3.5 describes two methods to determine lattice parameters for which there are no on-site two-body interactions and discusses limits set by three-body recombination.

3.1 Pseudo-potential for low-energy collisions, optical lattices, and effective field theory

In 1957 K. Huang [106] showed that the low-energy scattering of two neutral atoms of mass m with an isotropic inter-atomic potential can be modeled by the equivalent three-dimensional delta-function pseudo-potential

$$V_{\text{pseudo}}(\vec{R}) = 4\pi\frac{\hbar^2}{2\mu}(a - \frac{1}{2}r_e a^2\nabla^2)\delta(\vec{R})\frac{\partial}{\partial R}R\,, \tag{3.1}$$

where $\vec{R}$ describes the separation and orientation of the atom pair, ∇ is the gradient operator for the relative motion, $\mu = m/2$ is the reduced mass, and $\hbar = h/(2\pi)$. The scattering length a and the effective range r_e parametrize the effect of the physical interaction potential. (This derivation was revisited in Refs. [107–109].) Crucial for this chapter is that a and r_e have a simple relationship and can be tuned near Feshbach resonances.

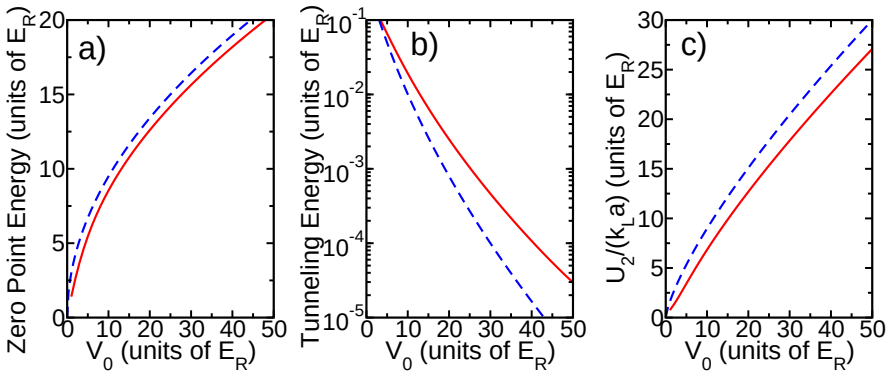

Figure 3.1: Zero-point energy (panel a), tunneling energies (panel b), and the scaled first-order two-body interaction strength $U_2/(k_L a)$ with no effective-range correction (panel c) as a function of lattice depth V_0 for a cubic, three-dimensional optical lattice. Solid red curves are based on exact band-structure calculations and exact Wannier functions. Dashed blue lines are based on oscillator solutions of the isotropic harmonic approximation around the lattice minima [110].

Our atoms are held in a three-dimensional periodic potential created by counter-propagating laser beams with wavevectors k_L. For simplicity we assume a cubic lattice with potential $V(\vec{x}) = V_0 \sum_i \cos^2(k_L x_i)$, where $\vec{x} = (x_1, x_2, x_3)$ is the atomic location and V_0 is the lattice depth. The potential has periodicity π/k_L and a minimum in each unit cell with harmonic frequency and single-atom oscillator length given by

$$\hbar\omega = 2\sqrt{V_0 E_R} \quad \text{and} \quad \ell = \sqrt{\hbar/(m\omega)} = 1/(k_L \sqrt[4]{V_0/E_R}) \,,$$

respectively. Here $E_R = \hbar^2 k_L^2/(2m)$ is the recoil energy.

We will rely on this harmonic approximation near the lattice minima. Figures 3.1(a) and (b) show that for sufficiently large V_0 this is qualitatively correct.

Panel (a) compares the zero point energy of the harmonic approximation, $3\hbar\omega/2$, with that of the on-site energy of the lowest band obtained from our exact band-structure calculation. The exact on-site energy is always smaller since anharmonic corrections are attractive. Similarly, panel (b) shows a comparison of the tunneling energies between nearest-neighbor unit cells. Here, the perturbative (harmonic) result underestimates the tunneling energy because anharmonic corrections delocalize the Wannier functions.

The harmonic approximation also simplifies the calculation of the interaction energies between atoms. Non-perturbative eigenenergies for two atoms interacting via a delta-function potential were derived in Ref. [111]. Moreover, Refs. [104, 105] perturbatively calculated the ground-state energy $E_{n=2,3,\cdots}$ of two, three, or more atoms based on effective-field theory [112]. In fact, up to second-order perturbation theory when $a \ll \ell$ and $r_e a^2/2 \ll \ell^3$ they showed $E_n = 3n\hbar\omega/2 + U_2 n(n-1)/2 + U_3 n(n-1)(n-2)/6$, where U_2 and U_3 are the two- and three-body interaction strengths

$$U_2/\hbar\omega = \xi + \frac{3}{2}\epsilon + (1-\log 2)\xi^2 + 2\left(2 - \frac{3}{2}\log 2\right)\xi\epsilon + \left(\frac{15}{4} - \frac{9}{4}\log 2\right)\epsilon^2\,, \quad (3.2)$$

and

$$U_3/\hbar\omega = \left\{6 - 4\sqrt{3} - 6\log\left(\frac{4}{2+\sqrt{3}}\right)\right\}\xi^2 + \left\{24 - \frac{52}{3}\sqrt{3} - 18\log\left(\frac{4}{2+\sqrt{3}}\right)\right\}\xi\epsilon + \left\{\frac{45}{2} - \frac{55}{3}\sqrt{3} - \frac{27}{2}\log\left(\frac{4}{2+\sqrt{3}}\right)\right\}\epsilon^2\,, \quad (3.3)$$

with dimensionless quantities $\xi = \sqrt{\frac{2}{\pi}}\frac{a}{\ell}$ and $\epsilon = \sqrt{\frac{2}{\pi}}\frac{r_e a^2}{2\ell^3}$, and $\log z$ is the natural logarithm. Four- and higher-body interaction strengths are zero at this order of

field theory. Reference [113] performed similar calculations for a box with periodic boundary conditions. We ignore small corrections from non-zero partial wave and anisotropic magnetic dipole-dipole scattering.

For completeness Fig. 3.1(c) compares the two-body interaction strength in a harmonic trap evaluated to first-order in a and $r_e = 0$ (i. e. $U_2 = \sqrt{2/\pi}(a/\ell)\hbar\omega$) with the corresponding matrix element based on the energetically-lowest Wannier function of the three-dimensional optical lattice. The curves are in sufficiently good agreement such that a harmonic approximation with analytical results up to second-order perturbation theory can be confidently used for the analysis of U_2 and U_3.

3.2 Cancellation of the two-body interaction

We can now search for parameter regimes where U_2 is small compared to U_3 and, in particular, look for the case $U_2 = 0$. In fact, by factorizing U_2 and requiring that $\xi \ll 1$ and $\epsilon \ll 1$ we realize that if we can achieve

$$\epsilon = -\frac{2}{3}\xi \quad \text{or} \quad \frac{1}{2}r_e a^2 = -\frac{2}{3}a\ell^2 \tag{3.4}$$

the two-body interaction strength U_2 vanishes as the contributions from the scattering length and the effective range cancel. Equation 3.4 can be shown to hold to all orders in a and r_e from Ref. [111] (by making the replacement $a \to a + r_e a^2(2\mu E/\hbar^2)/2$ in Eq. 16 of that article). More importantly, the three-body interaction strength does not vanish and is

$$U_3/\hbar\omega = -\frac{16}{9}\frac{1}{\sqrt{3}}\xi^2 = -\frac{32}{9\pi\sqrt{3}}\frac{a^2}{\ell^2}\,, \tag{3.5}$$

which is always attractive and remains of the same order of magnitude as in Eq. 3.3. The next two sections describe ways in which we can achieve this cancellation.

3.3 Van der Waals potential

Ultra-cold scattering between structureless ground-state atoms, such as the alkaline-earth atoms, or between more-complex atoms away from any scattering resonance, such as alkali-metal atoms in an external magnetic field, is controlled by its long-range isotropic $-C_6/R^6$ potential, where C_6 is the van-der-Waals coefficient. This follows from the fact that for separations where deviations from this van-der-Waals potential due to electron bonding are significant, its depth is already orders of magnitude larger than the initial kinetic energy of the atoms [101, 103]. References [114, 115] then showed that when the potential has a scattering length a its effective range is

$$\frac{1}{2}r_e a^2 \;=\; \frac{1}{3c_e^2}\bar{a}\left((a-\bar{a})^2+\bar{a}^2\right)\,, \tag{3.6}$$

where $\bar{a} = c_e(2\mu C_6/\hbar^2)^{1/4}$ is the mean scattering length [102] and $c_e = 2\pi/[\Gamma(1/4)]^2 = 0.4780\cdots$, and $\Gamma(z)$ is the Gamma function. For typical atoms $\bar{a}$ lies between $30a_0$ and $100a_0$, where $a_0 = 0.0529$ nm is the Bohr radius. Figure 3.2 shows the effective range volume $r_e a^2/2$ as a function of a. It is always positive, has a minimum at $a = \bar{a}$, and for $a \to 0$ equals $r_e a^2/2 = 2.918\cdots\bar{a}^3$, which implies that r_e diverges for a zero scattering length.

In order to find regimes where U_2 is small compared to U_3, we investigate whether Eq. 3.4 can hold. This equality is graphically solved in Fig. 3.2 for two

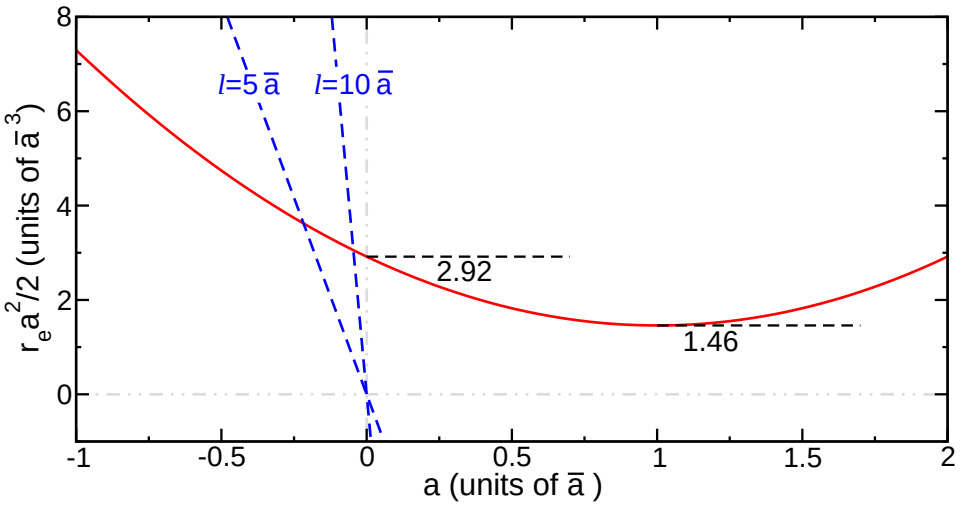

Figure 3.2: The effective range volume $r_e a^2/2$ (solid red curve) as a function of scattering length a for a van der Waals potential. All lengths are expressed in units of the mean scattering length $\bar{a}$. The dashed blue curves correspond to $-2a\ell^2/3$ for two values of ℓ. At intersections of $r_e a^2/2$ and $-2a\ell^2/3$ the effective two-body interaction is tuned to zero.

ratios $\ell/\bar{a} \gg 1$, corresponding to typical circumstances in current experiments. We immediately observe that solutions exist for negative scattering lengths that are small compared to $\bar{a}$. In fact, a Taylor expansion for large $\ell/\bar{a}$ gives

$$\frac{a}{\bar{a}} = -\frac{1}{c_e^2}\left(\frac{\bar{a}}{\ell}\right)^2 + O(1/\ell^4) \tag{3.7}$$

and thus $|a/\bar{a}| \ll 1$ and $|a/\ell| \ll 1$ consistent with our assumptions.

For a van-der-Waals potential a is fixed. Hence, Eq. 3.7 is a constraint on ℓ or the trapping frequency ω (and thus on the lattice depth V_0). Moreover, there exist only a few atomic species with the small negative scattering length needed to have a small or vanishing U_2. In fact, we are only aware of the strontium isotope ^{88}Sr to

satisfy $|a/\bar{a}| \ll 1$, since it has a scattering length of $a = -2.0(3)a_0$ and $\bar{a} = 71.76a_0$ [116]. (Numbers in parenthesis are one-standard-deviation uncertainties.) Hence, we find that $U_2 = 0$ requires $\ell = 900a_0$ and thus $\omega/(2\pi) = 50$ kHz. Assuming a realistic Sr optical lattice with a photon recoil energy of $E_R/h = 4.0$ kHz, we read from Fig. 3.1a) that $V_0 \approx 40E_R$ and that from Fig. 3.1b) the tunneling energy $J \approx 10^{-4}E_R$ or $J/h \approx 0.4$ Hz. This tunneling energy is comparable to the three-body strength $U_3/h \approx -0.15$ Hz calculated from Eq. 3.5.

3.4 Feshbach resonances

Ultracold scattering of alkali-metal atoms [103] in a magnetic field B contains collisional resonances, where the scattering length can be tuned. Recently, interest has also focused on resonances with atoms with large magnetic moments, such as Cr [117], Er [118], and Dy [119, 120], as the long-range magnetic dipole-dipole interaction influences their collective behavior.

At ultra-cold collision energies $E = \hbar^2k^2/(2\mu)$ resonant scattering is described by the scattering amplitude [121–123]

$$f(k) = f_{\rm bg}(k) - e^{2i\delta_{\rm bg}(k)}\frac{\Gamma(E)/2}{E - E_{\rm res}(B,E) + i\Gamma(E)/2}\,, \tag{3.8}$$

where $f_{\rm bg}(k) = e^{i\delta_{\rm bg}(k)}\{\sin\delta_{\rm bg}(k)\}/k$ is the background scattering amplitude away from the resonance and $\delta_{\rm bg}(k)$ is the background phase shift. We assume that the low-energy behavior of $f_{\rm bg}(k)$ is that of a van-der-Waals potential with scattering length $a_{\rm bg}$ as discussed in Sec. 3.3. The dispersive second term of Eq. 3.8 describes the resonance with a magnetic-field and energy-dependent resonance loca-

tion $E_{\rm res}(B,E) = \mu_e(B-B_0) + \beta E$ and positive energy width $\Gamma(E) = 2(ka_{\rm bg})\Gamma_0 \times (1+\alpha E/\Gamma_0)$, where μ_e is the magnetic moment of the resonant state, B_0 is the magnetic field at resonance, and Γ_0 is the resonance strength. Finally, the field-independent coefficients α and β describe additional energy dependencies of $\Gamma(E)$ and $E_{\rm res}(E)$ and will affect the effective range.

We note that by definition $\mathrm{Re}f(k) = -a - \{r_e a^2/2 - a^3\}\,k^2 + \cdots$ and a Taylor expansion of Eq. 3.8 in k then leads to the scattering length $a = a_{\rm bg} - a_{\rm bg}\Gamma_0/E_{\rm res}(B,0)$ and effective range volume

$$\frac{1}{2}r_e a^2 = \frac{1}{2}r_{\rm bg}a_{\rm bg}^2 + a a_{\rm bg}(a-a_{\rm bg}) - \frac{(1-\beta)(a-a_{\rm bg})^2\bar{a}}{s_{\rm res}} + \frac{\alpha(a-a_{\rm bg})\bar{a}a_{\rm bg}}{s_{\rm res}} \tag{3.9}$$

$$\equiv\; V_{\rm q} + g_{\rm q}(a-a_{\rm q})^2\,, \tag{3.10}$$

where $r_{\rm bg}$ is the background effective range given in Eq. 3.6 when evaluated at scattering length $a_{\rm bg}$. We have eliminated the dependence on $E_{\rm res}(B,0)$ in favor of a and the dimensionless $s_{\rm res} \equiv a_{\rm bg}\Gamma_0/(\bar{a}\bar{E}) > 0$ characterizes the resonance strength in terms of the mean scattering length $\bar{a}$ and energy $\bar{E} = \hbar^2/(2\mu\bar{a}^2)$ of a van-der-Waals potential [103]. A resonance is narrow when $s_{\rm res} \ll 1$ and broad otherwise. Moreover, the volume $r_e a^2/2 \to r_{\rm bg}a_{\rm bg}^2/2$ when $a \to a_{\rm bg}$ as expected and

$$\frac{1}{2}r_e a^2 \to \frac{1}{2}r_{\rm bg}a_{\rm bg}^2 - (1-\beta+\alpha)\bar{a}a_{\rm bg}^2/s_{\rm res}$$

for $a \to 0$ showing that $r_e a^2/2$ can be negative. For narrow resonances this was already noted in Ref. [124].

The effective-range volume near a resonance is a quadratic polynomial in a with coefficients defined by Eq. 3.10. This dependence agrees with the coupled-channels calculations with rigorous interatomic potentials of Ref. [125]. Their $V_{\rm q}$,

Table 3.1: Parameters for five Feshbach resonances. Columns represent the atomic species, B_0 in Gauss, the background scattering length $a_{\rm bg}$, resonance strength $s_{\rm res}$, coefficients $V_{\rm q}$, $g_{\rm q}$ and $a_{\rm q}$, where available from Ref. [125], and dimensionless α and β found from a fit to $V_{\rm q}$, $g_{\rm q}$, and $a_{\rm q}$ in Eq. 3.10. Lengths and volumes are in units of $\bar{a}$ and $\bar{a}^3$, respectively, and 1 G= 0.1 mT. (Finally, $\bar{a} = 42.95a_0$, $61.65a_0$, $43.63a_0$, and $96.51a_0$ for ^{23}Na, ^{39}K, ^{52}Cr, and ^{133}Cs, respectively.)

	B_0	$a_{\rm bg}$	$s_{\rm res}$	$V_{\rm q}$	$g_{\rm q}$	$a_{\rm q}$	α	β
^{39}K	745	-0.541	0.00062	4.7	-1540	-0.55	0.0354	0.0468
^{133}Cs	227	21.34	0.19	1000	-4.19	29	-3.55	-3.85
^{23}Na	853	1.47	0.0002	-	-	-	0	0
^{52}Cr	500	2.45	0.03	-	-	-	0	0
^{133}Cs	19.8	1.66	0.002	-	-	-	0	0

$g_{\rm q}$, and $a_{\rm q}$ for a narrow ^{39}K and broad Cs resonance are tabulated in Table 3.1. The corresponding effective range volume as well as that for a narrow Na resonance based on Eq. (3.9) with $\alpha = \beta = 0$ are shown in Fig. 3.3 as a function of a as it is tuned with a magnetic field. For narrow resonances $\alpha, \beta \ll 1$ and α, β have negligible effect on $r_e a^2/2$. For broad resonances with larger α, β their effect is large. For both cases $r_e a^2/2$ is negative and orders of magnitude larger than that for van-der-Waals potentials.

The model for the effective range volume now enables us to find scattering

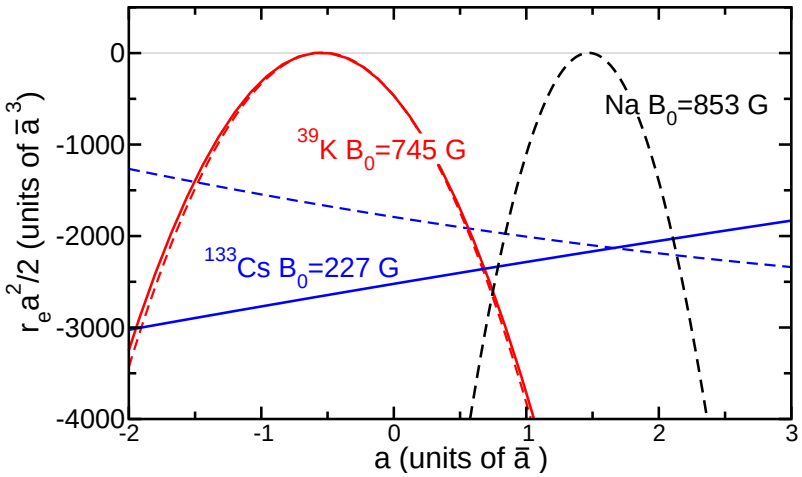

Figure 3.3: Effective volume $r_e a^2/2$ of the Feshbach resonances listed in Table 3.1 as a function of scattering length a with lengths in units of $\bar{a}$. Solid lines correspond to volumes based on Eq. (3.9) with $\alpha, \beta \neq 0$ or equivalently the coupled-channels calculation of [125]. Dashed lines follow from Eq. (3.9) with $\alpha = \beta = 0$.

lengths where U_2 is small compared to U_3. We set $U_2 = 0$ and Eq. 3.4 gives

$$V_{\rm q} + g_{\rm q}(a - a_{\rm q})^2 = -\frac{2}{3} a \ell^2 \,, \tag{3.11}$$

where both a and ℓ can be tuned. Coefficients $V_{\rm q}$, $g_{\rm q}$, and $a_{\rm q}$ are fixed by the resonance. Consequently, choosing a fixes the harmonic trapping frequency and vice versa. Crucially, and unlike for a van-der-Waals potential, $r_e a^2/2$ is mostly negative and large compared to $\bar{a}^3$ so that $U_2 = 0$ can occur for positive a on the order of $\bar{a}$. We must, however, also require that $|r_e a^2/2| \ll \ell^3$. This can not be guaranteed for all resonances. For example, Fig. 3.3 implies that for the narrow ^{39}K resonance and $a > \bar{a}$ the volume $|r_e a^2/2| \geq \ell^3$ assuming typical ℓ between $10\bar{a}$ and $100\bar{a}$. The narrow Na and broader Cs resonance show more promise.

In Fig. 3.4 we make these observations more precise by plotting U_2 and U_3

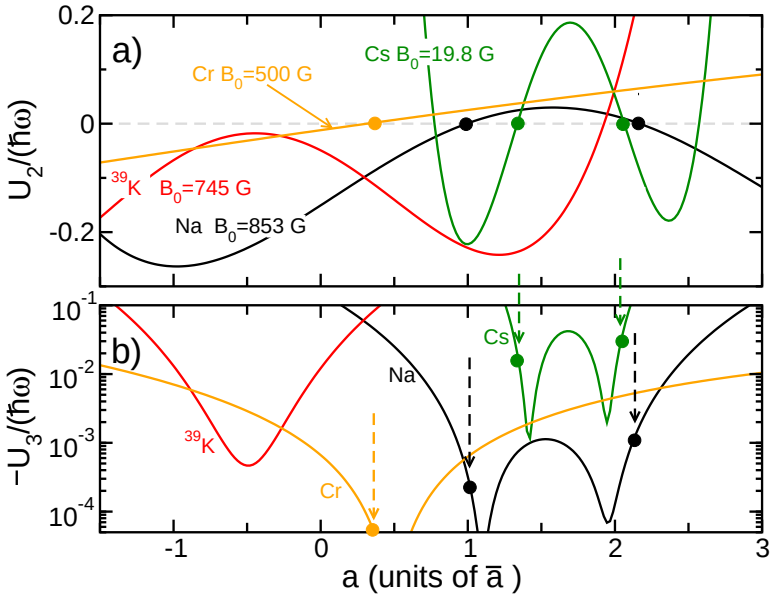

Figure 3.4: Two-body interaction strength U_2 (panel a) and minus one times the three-body strength $-U_3$ (panel b) in a harmonic trap with $\omega/(2\pi) = 50$ kHz as a function of the scattering length a for a narrow ^{23}Na (black lines), ^{39}K (red lines), ^{52}Cr (orange lines), and ^{133}Cs (green lines) Feshbach resonance tabulated in Table 3.1. Filled circles in both panels and arrows in panel (b) indicate where $U_2 = 0$.

as a function of a for four narrow Feshbach resonances (with $s_{\rm res} \ll 0.1$) tabulated in Table 3.1 and assuming a harmonic trap with frequency $\omega/(2\pi) = 50$ kHz. For all four resonances $U_2 = 0$ for at least one value of a. The second, broader ^{133}Cs resonance with $B_0 = 227$ G and $s_{\rm res} = 0.19$ has no such point and is not shown. The cases where both $U_2 = 0$ and $|U_3|/(\hbar\omega) \ll 1$ are indicated in the figure with markers. For the Na and Cs resonance $U_2 = 0$ when $a \approx \bar{a}$ or $2\bar{a}$ and $-U_3/(\hbar\omega) \geq 0.001$. For the ^{39}K resonance a zero crossing occurs at $a \approx 2\bar{a}$ but $U_3/(\hbar\omega) \gg 1$, outside the validity range of the theory.

Finally, we compare the expected value of U_3 with the tunneling energy J, depicted in Fig. 3.1, in an optical lattice. Noting that for commonly-used lasers in and near the optical domain the recoil energy E_R/h lies between 2 kHz and 10 kHz for alkali-metal atoms, we find that for $\omega/(2\pi) = 50$ kHz the tunneling energy J is about ten times smaller than $|U_3|$. For a shallower lattice and thus smaller ω the tunneling energy increases exponentially, while U_3, maintaining the condition that $U_2 = 0$, decreases much more slowly.

3.5 Detection and three-body recombination

Several observations can be made about the feasibility and limitations of the proposal. These range from the detection of the point where $U_2 = 0$, the behavior of Bose-Hubbard models to three-body recombination. The next two subsections will briefly address these points.

3.5 Detection of $U_2 = 0$?

We can locate lattice parameters where $U_2 = 0$ with two types of experiments. The simplest is to perform vibrational spectroscopy on two or three isolated bosonic atoms held in a dipole trap or in an optical lattice where tunneling is negligible. For pairs of fermionic alkali-metal atoms as well as for one fermion and one boson in an optical lattice site this has been shown to work near a Feshbach resonance by Refs. [126, 127]. Based on predictions of [128] they found a new class of confinement-induced bound states for large scattering lengths. An accurate study for smaller scattering lengths on the order of the mean scattering length or less, however, is lacking for both fermionic and bosonic alkali-metal atoms. For ^{88}Sr with its small, negative scattering no such measurements have been performed. Finally, no spectroscopic experiments for three-atoms exist.

A second type of experiments that can locate $U_2 = 0$ are so-called collapse-and-revival experiments in optical lattices, where changes of the lattice parameters induce non-equilibrium dynamics. Specifically, realizations where after a sudden and large increase of the lattice depth tunneling is negligible, the values for U_2 and U_3 can be inferred from measurements of the momentum distribution as a function of delay after the ramp [104, 129–131]. In these experiments the initial state is a superfluid and, hence, to good approximation each site contains a superposition of atomic Fock states in the lowest trap level. After the sudden lattice-depth increase this superposition starts to evolve and measurement of the momentum distribution is sensitive to differences of the energies E_n for different n. These measurements

have not been repeated near Feshbach resonances.

3.5 Three-body recombination

Atom loss from the lattice can limit the realization of our proposal. Loss of one atom at a time, due to collisions with background molecules in the vacuum or light-induced loss from the lattice lasers, can be mitigated by improving the vacuum pressure and a careful choice of laser frequencies. Two-body loss can always be removed by choosing the hyperfine state with the lowest internal energy. This leaves inelastic three-body recombination as an intrinsic loss mechanism. An ultracold homogeneous thermal gas with number density n loses atoms according to rate equation $dn/dt = -3K_3n^3$. For scattering from short-range potentials [37, 132] the event rate coefficient $K_3 \leq C_{\max}\hbar a^4/m$ with $C_{\max} = 67$ when the scattering length $|a| \gg \bar{a}$, while $K_3 \approx C_0\hbar\bar{a}^4/m$ with $C_0 = 25$ for $|a| \sim \bar{a}$. Recently, Refs. [92, 93] showed that for longer-ranged van-der-Waals potentials and near collisional resonances C_0 depends on atomic species and resonance, and can be much larger than 25. Finally, Ref. [94] showed empirically that for a broad ^{7}Li resonance with a negative effective range $K_3 \approx C_{\max}\hbar(a^3 - r_e a^2/2)^{4/3}/m$ gives a reasonable description of experimental data close to the resonance.

In a lattice site recombination can be included as an imaginary contribution to U_3. That is we use $U_3 \to U_3 - i\Gamma_3/2$, where $\Gamma_3 = \hbar K_3 \int d^3\vec{x}|\Psi(\vec{x})|^6$ and $\Psi(\vec{x})$ is the normalized single-atom ground-state wavefunction in a lattice site. For an

isotropic harmonic trap and $|a| \sim \bar{a}$ this leads to

$$\Gamma_3 = \frac{C_0}{3\pi^3}\frac{\bar{a}^4}{\ell^4}\hbar\omega \tag{3.12}$$

when $U_2 = 0$. Losses are acceptable when $\Gamma_3 \ll |U_3|$ and thus

$$\frac{|a|}{\bar{a}} \gg \sqrt{\frac{3\sqrt{3}C_0}{32\pi^2}}\frac{\bar{a}}{\ell} = 0.64\frac{\bar{a}}{\ell} \tag{3.13}$$

for $C_0 = 25$. Since typically $\ell > 10\bar{a}$, a scattering length on the order of $\bar{a}$ is required. This condition can be met with Feshbach resonances, but also indicates that an experiment with ^{88}Sr will be hard. A similar analysis with more restrictive estimate of Ref. [94] suggests that weaker trapping potentials with $\ell \gg 10\bar{a}$ will be required.

3.6 Conclusion

We have proposed a means to create an ultra-cold gas of bosonic atoms in an optical lattice that only interacts via on-site three-body interactions. This is achieved by a careful cancellation of two contributions in the pair-wise interaction between two atoms, one proportional to the zero-energy scattering length and a second proportional to the effective range. We predict that this cancellation can occur for the strontium-88 isotope as well as near narrow magnetic Feshbach resonances in alkali-metal atom or chromium collisions.

For optical lattice depths and/or magnetic field strengths where the pair-wise interaction has been cancelled, i.e. $U_2 = 0$, we have also shown that the three-body interaction strength can be of the same order of magnitude as the tunneling energy

of atoms hopping between neighboring lattice sites. Three-body recombination can limit the practical duration of coherent atom evolution.

Although the purpose of this chapter has not been the characterization of the many-body ground state or the dynamical properties of a system near $U_2 = 0$, a brief remark is in order. For a small number of atoms per lattice site we predict that the three-body interaction is attractive. For a Hubbard model with finite tunneling J on the order of U_3 this can indicate that the ground state corresponds to a state with all atoms in one site and, in essence, the system would "collapse", similar to the instability of systems with a negative two-body strength U_2. To prevent this collapse a weak global trapping potential must be added. On the other hand, we expect that it is realistic to perform dynamical experiments where initially the ground state for positive U_2 is prepared and, subsequently, the lattice parameters are changed to ones where $U_2 = 0$.

3.7 Acknowledgments

This work has been supported by the National Science Foundation Grant No. PHY-1506343.

Chapter 4

Bose-Einstein condensation in an excited band

4.1 Introduction

Bose-Einstein condensation of ultracold atoms in the lowest Bloch band of a periodic optical-lattice potential [1, 38] occurs at zero quasi-momentum. This condensation can be understood from a bosonic Hubbard model. By varying the relative strength of tunneling energy and atom-atom interaction strength, this model predicts a quantum phase transition between a delocalized compressible superfluid state and a localized incompressible Mott state [12, 13]. This was first observed by Greiner *et al.* [14].

According to Feynman's "no-node" theorem [39], the zero quasi momentum ground state wave function is positive definite and has time-reversal (TR) symmetry. However, the no-node theorem does not apply to excited bands and the lowest energy state within the band may have non-zero quasi momenta. Thus, we can obtain exotic states of bosons with complex valued wave functions that spontaneously break the TR symmetry [40, 41]. Simultaneously, depending on the lattice param-

eters, two or more bands can become nearly degenerate and multiflavor Hubbard models can be realized where the atom-atom interaction strength can become of the order of bandgaps. In addition, for these bands with nearly degenerate excited orbitals, tunneling can be "anisotropic" in that different orbitals tunnel preferably along different primitive lattice vectors. This has lead to several proposals of unconventional Bose-Einstein condensates in optical lattices and predictions of rich orbital physics in higher bands [40–45]. For example, Wirth *et al.* [46] explores orbital superfluidity in $sp-$hybridized orbital bands in which condensation occurs at non-zero quasi momentum at the edge of the first Brillouin zone. Interestingly Refs. [40, 42] showed that Bose-Einstein condensates formed in excited Bloch bands may have very long lifetimes. Recently, such condensates have been experimentally observed [2, 46–48].

Optical lattices of two or more dimensions can have band crossings either at zero or non-zero quasi momentum. The band crossing at zero quasi momentum must occur between excited bands by virtue of the no-node theorem while the crossing at non-zero quasi momentum can occur between the ground and excited band. An example of the latter case occurs for a two-dimensional hexagonal lattice structure such as seen in Dirac cones of graphene [6, 133]. In fact, more than two bands can intersect [46]. The topological significance of band crossing points is now an area of active research [63, 64] (and references therein).

Optical lattices can be changed in real time and are thus tunable. The simplest example of this was the observation of the superfluid to Mott insulator transition of a cubic lattice by adiabatically increasing the lattice depth [14]. More advanced

examples are the ability to dynamically change lattice geometries from triangular to hexagonal [6,7]. Independent tunability of the sign of the nearest-neighbor tunneling energies has also been demonstrated [134,135]. Finally, we note that this tunability can enable us to study Berry's phases [136] when band crossing of ground and/or excited bands occur for a particular choice of lattice depth and geometry. Adiabatic change of lattice parameters around this degeneracy point induce such phases.

In this chapter, I discuss the formation of a Bose-Einstein condensate in a 2D optical lattice, with a weak confinement along the z axis. This work is directly motivated by the experiment of Wirth *et al.* [46], in which Bose condensation is observed in the p band of a quasi 2D double-well optical lattice. The lattice in the xy plane consists of a checkerboard pattern of alternate deep and shallow wells, whose relative well depth can be controlled in real time by changing the phase difference θ between the counter-propagating lasers forming the optical lattice. Exciting atoms to higher bands is a two step process. Initially, as shown in Fig. 4.1a, an angle θ is chosen such that one of the wells is much deeper than the other, and the atoms are largely confined to the local ground state of these deep wells. There is very little tunneling between the wells and the atoms form an array of one dimensional tubes along the z axis.

The angle θ is now rapidly changed such that the ground s state becomes degenerate or nearly degenerate with the first excited p state of adjacent wells, which are now the deeper wells as shown in Fig. 4.1b. This change must be fast with respect to tunneling energies between adjacent wells, but adiabatic or slow with respect to the onsite energies of the well to which the atoms have been confined.

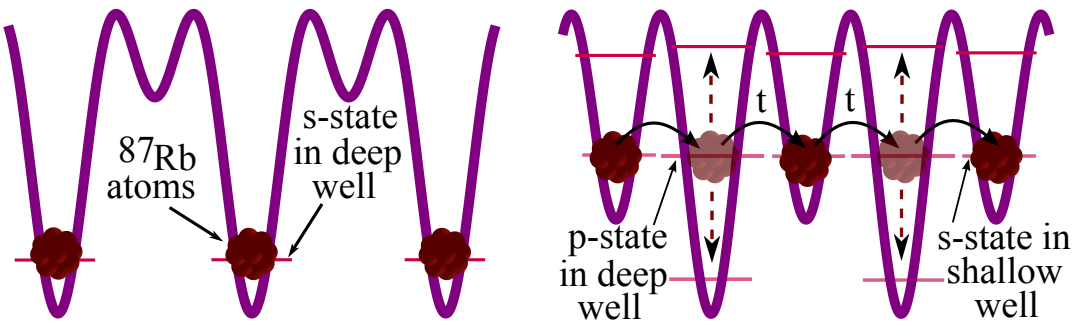

(a) (b)

Figure 4.1: A one-dimensional schematic of lattice transformation to populate atoms in excited bands. Panel (a) shows the initial lattice configuration with atoms confined to the ground s state of the deeper wells. The atoms form an array of one dimensional tubes where tunneling between adjacent tubes is negligible. Panel (b) shows the final lattice configuration, with θ chosen such that the s state in the shallow well is nearly degenerate to the p state of the deeper well. The well that was initially the deepest is now the shallower of the two. The hopping energy t now distributes the atoms in the excited bands of the 2D optical lattice. The vertical dashed lines represent a collisional decay process in which one of the atoms decays to the ground band, while the other jumps to an excited band. The decay processes largely involve vertical atom transitions within the deep sites.

After the change, the atoms can tunnel and populate the excited bands of the optical lattice. We thus observe a transition from a quasi one dimensional geometry to a three dimensional one, with atoms initially confined to one dimensional wells getting distributed over the entire 2D lattice due to tunneling and elastic collision. Wirth *et al* [46] saw that in this process, a Bose condensation is formed in the quasi momenta of lowest energy in the (first) excited band of the optical lattice. Interestingly, these quasi momenta are at the edge of the first Brillouin zone.

To model this physics, we perform a numerically exact as well as a tight binding calculation of the single particle band structure. A comparison shows that for the first four bands, the tight binding model gives a sufficient description of the band structure. We then performed a calculation for the thermodynamic quantities for both cases in Fig. 4.1, assuming that the atoms do not interact. In particular, we estimate the critical atom number and critical temperature at which a Bose-Einstein condensate appears. We find that these quantities crucially depend on the detuning between the closely resonant s and p orbitals in adjacent wells. We also justify the assumption of non-interacting bosons.

Simultaneously, these atoms undergo collisional de-excitation to the ground band. De-excitation occurs when one or more atoms make a transition to the ground band in the xy plane. This energy release is accompanied by an increase in energy along the z direction. An example of such a process is shown in Fig. 4.1b. We will show that the dominant decay process is that one in which both colliding atoms decay to the ground band. We estimate the rate for this transition in the tight binding model as well as numerically, and find qualitative agreement. We provide

an analytical expression for the rate as a function of lattice depth and θ. With increasing lattice depth, processes where one of the colliding atoms decays to the ground band, and the other to an excited band become important. These rates can only be evaluated numerically, as the tight binding model is inadequate for multiply-excited bands. At lattice parameters where adjacent s and p orbitals are resonant, the total decay rate is significantly smaller than the tunneling time scales, consistent with the observations of the experiment [46].

The chapter is set up as follows. In Section 4.2, we set up the Hamiltonian. In Section 4.3 we discuss the tight binding calculation of the band structure followed by a numerical estimate of the same in Section 4.4. We also compare both the models in this section. Section 4.5 uses the tight binding results to estimate the thermodynamic properties of the condensate. In section 4.6 we study the lattice transformation used to excite atoms to the excited bands, and estimate the relationship between the initial and final temperatures. Section 4.7 deals with the interaction processes that lead to the decay of the condensate. We conclude in Section 4.8.

4.2 Optical lattice Hamiltonian

Our starting point is the second-quantized Hamiltonian for bosonic atoms in an external trapping potential $H = H_0 + H_{\rm int}$, where

$$H_0 = \int d^3x\, \psi^\dagger(\mathbf{x}) \left(\frac{-\hbar^2}{2m_a}\nabla^2 + V_{op}(x,y) + V_z(z) \right) \psi(\mathbf{x})$$

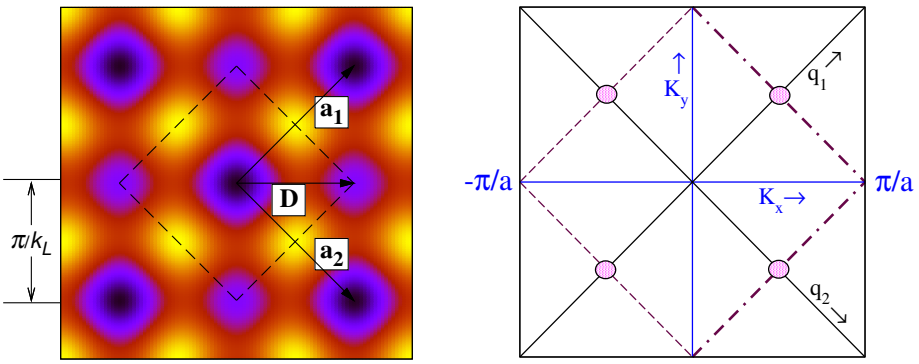

(a) (b)

Figure 4.2: Panel(a) shows the contour graph of the 2D double-well optical lattice at $V_0 = 6E_R$ and $\theta = \pi/2.2$. The darker and brighter colors represent lower and higher energies, respectively. An alternating array of deeper and shallower wells are clearly visible. The origin of our coordinate system is at the central deep well. The primitive lattice vectors are $\mathbf{a}_1$ and $\mathbf{a}_2$ and the vector $\mathbf{D} = a\hat{\mathbf{x}}$ connects neighboring deep and shallow wells.The dashed lines enclose a unit cell. Panel(b) shows the first two Brillouin zones of the optical lattice as a function of quasi momentum (K_x, K_y). The area inside the dashed region including the dashed-dotted edge represents the first zone. Moreover we define $q_1 = K_x + K_y$ and $q_2 = K_x - K_y$. The circles represent the atoms at the four non-zero quasi momenta, where the second band has the minimum of energy.

and $H_{\text{int}} = (g/2)\int d^3x\, \psi^\dagger(\mathbf{x})\psi^\dagger(\mathbf{x})\psi(\mathbf{x})\psi(\mathbf{x})$, where $\psi(\mathbf{x})$ is the field operator at position $\mathbf{x}$, m_a is the atomic mass and $\hbar$ is the reduced Planck's constant. The optical-lattice potential in the x-y plane is given by

$$V_{op}(x,y) = -V_0\left(\cos^2 k_L x + \cos^2 k_L y + 2\cos\theta\cos k_L x\cos k_L y\right), \tag{4.1}$$

with k_L the magnitude of the laser wave-vector and θ the phase difference between the counter propagating laser beams forming the optical lattice. The positive V_0 determines the lattice depth and $V_{op}(x,y) \leq 0$ for all x and y.

In addition, there is also a weak harmonic potential in the z direction, $V_z(z) = m_a\omega_z^2 z^2/2$, with frequency ω_z. The Hamiltonian H_{int} describes the atom-atom interaction where $g = 4\pi\hbar^2 a_s/m_a$, which is proportional to the s-wave scattering length a_s. It is convenient to define the recoil energy $E_R = \hbar^2 k_L^2/(2m_a)$. We study near degeneracies between the various excited bands. They occur when V_0 is between $5E_R$ and $10E_R$. A weak harmonic trap corresponds to $\hbar\omega_z \ll E_R$.

The optical lattice potential $V_{op}(x,y)$ gives rise to a double-well optical-lattice, with adjacent wells of unequal well depth, depending on the value of θ. Figure 4.2a shows an example of the 2D double well optical lattice formed by V_{op}. The two primitive lattice vectors are $\mathbf{a}_1 = a\,(\hat{\mathbf{x}} + \hat{\mathbf{y}})$ and $\mathbf{a}_2 = a\,(\hat{\mathbf{x}} - \hat{\mathbf{y}})$, where $a = \pi/k_L$ is the distance between neighboring shallow and deep wells. The reciprocal lattice vectors are $\mathbf{G} = \mathbf{G}_{m,n} = m\mathbf{b}_1 + n\mathbf{b}_2$, with integers m, n, and primitive reciprocal lattice vectors $\mathbf{b}_1 = k_L(\hat{\mathbf{x}} + \hat{\mathbf{y}})$ and $\mathbf{b}_2 = k_L(\hat{\mathbf{x}} - \hat{\mathbf{y}})$. Figure 4.2b shows the first Brillouin zone as a function of quasi momentum $\mathbf{K} = (K_x, K_y)$. For convenience we define the quasi momenta $q_1 = K_x + K_y$ and $q_2 = K_x - K_y$. In this basis the first

Brillouin zone is the square region $-\pi/a < q_1, q_2 \leq \pi/a$.

4.3 Band structure in the tight binding model

An approximate band structure for the 2D single particle Hamiltonian, $H_{op} = -(\hbar^2/2m_a)(\partial_x^2 + \partial_y^2) + V_{op}(x, y)$ in the xy plane is found from a tight binding model using localized harmonic oscillator wave functions as basis functions [137]. We first expand $V_{op}(x, y)$ to second order in the coordinates around the minima of the deep and shallow well. To this order, the wells are isotropic and have harmonic oscillator energy $\hbar\omega_{d,s} = \sqrt{4V_0E_R(1 \pm \cos\theta)}$ and harmonic length $l_{d,s} = \sqrt{\hbar/m_a\omega_{d,s}}$. Here, the subscripts d and s stand for deep and shallow well, respectively. For $\theta < \pi/2$, an example of which is shown in Fig. 4.2a, the deep well is located at the origin $(x, y) = (0, 0)$ and the shallow well is located at $\mathbf{D} = a\hat{\mathbf{x}}$.

The harmonic oscillator wave functions for the deep and shallow wells based on frequencies ω_d and ω_s are the local wave functions in our tight binding model. We choose $\phi_j(\mathbf{r})$ to represent wave functions in the shallow well and $\chi_j(\mathbf{r})$ for wave functions in the deep well. The subscript $j = s, p_x, p_y, d_{x^2}, d_{y^2}, d_{xy}, \ldots$, where s stands for the ground state and p_x and p_y represent the first two degenerate excited states with excitations along the x and y directions, respectively. The states d_{x^2}, d_{y^2}, d_{xy} represent the doubly-excited d orbitals, with two excitations along the x direction, two excitation along the y direction and one excitation in each direction, respectively. For lattice depths relevant in this chapter, orbitals with higher excitations are not important.

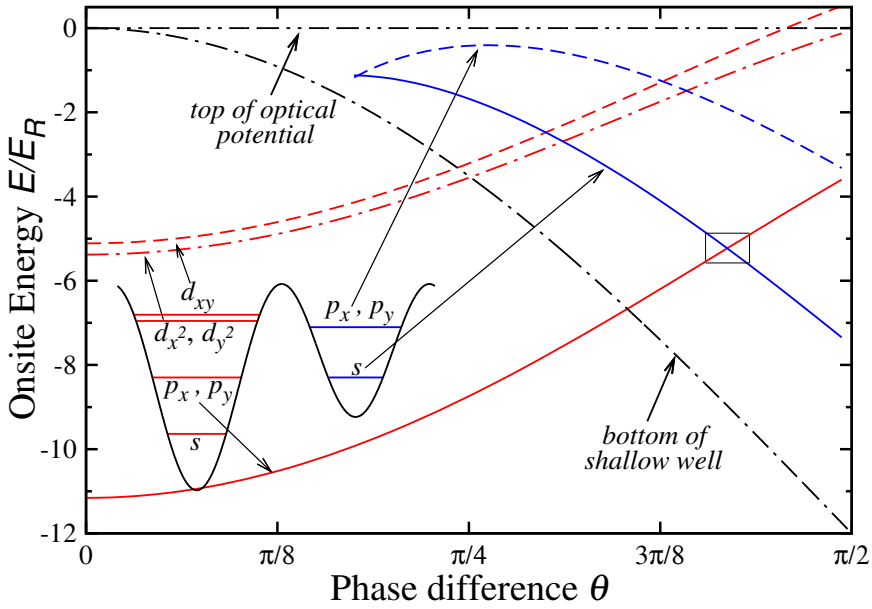

Figure 4.3: Onsite energy in each well from tight binding model in units of E_R as a function of the phase difference θ at $V_0 = 6E_R$. The energies are estimated in the harmonic oscillator approximation. The inset is a one-dimensional schematic of the asymmetric double well lattice, where horizontal lines in the wells represent the onsite energy levels. The various arrows map these lines to the corresponding onsite energies. The zero of energy is at the maximum energy of the optical potential. For the deep well, s, p and d orbitals exist, except for $\theta \approx \pi/2$ where the d orbital no longer exist. The s orbital in the deep well has an energy below $-12E_R$. The dashed line indicates the bottom of the shallow well. This well does not support bound states for $\theta < 0.18\pi$. The box denotes the point of degeneracy, $\theta = \theta_{res} \approx 0.42\pi$, between the s state in the shallow well and the p state in the adjacent deep well.

In the tight binding model, the local onsite energies $\langle\psi_j|H_{op}|\psi_j\rangle$ and $\langle\chi_j|H_{op}|\chi_j\rangle$ are expectation values of the total optical-lattice Hamiltonian, an improvement over solely using the harmonic oscillator approximation. A schematic of the local onsite energies in these wells is shown in the inset of Fig. 4.3. The onsite energy for the p_x or p_y state in the deep well is

$$E_p = \hbar\omega_d - V_0\left\{1 + \left(1 - k_L^2 l_d^2\right)e^{-k_L^2 l_d^2} + 2\cos\theta\left(1 - \frac{k_L^2 l_d^2}{2}e^{-k_L^2 l_d^2/2}\right)\right\}, \tag{4.2}$$

and onsite energy of the $s-$orbital in the shallow well is

$$E_s = \hbar\omega_s/2 - V_0\left\{1 + e^{-k_L^2 l_s^2} - 2e^{-k_L^2 l_s^2/2}\cos\theta\right\}. \tag{4.3}$$

We are interested in (V_0, θ) where E_p and E_s are degenerate or nearly degenerate.

Figure 4.3 shows five onsite energies as a function of θ for $V_0 = 6E_R$. Only energies close to E_s and E_p are shown. For this lattice depth and for $0 < \theta < \pi/2$, the degeneracy occurs at $\theta = \theta_{res} \approx 0.42\pi$. For other values of V_0, the degeneracy shifts to a different θ. We also note that the onsite energy of the d_{xy} state is larger than that of the d_{x^2} or d_{y^2} state.

From these local wave functions, we can construct extended basis functions of definite quasi-momentum $\mathbf{K}$, $\langle\mathbf{x}|j,\mathbf{K}\rangle_s$ and $\langle\mathbf{x}|j,\mathbf{K}\rangle_d$ [137], which involves a sum over the total number of unit cells M. Here, $\mathbf{K}$ is restricted to the first Brillouin zone, and the subscripts s and d on the kets stand for shallow and deep wells, respectively. The Hamiltonian H_{op} conserves $\mathbf{K}$.

Close to the degeneracy point shown in Fig. 4.3, we can write down a tight binding Hamiltonian only taking into account the three basis functions $|s,\mathbf{K}\rangle_s$,

$|p_x, \mathbf{K}\rangle_d$ and $|p_y, \mathbf{K}\rangle_d$. The Hamiltonian is

$$\begin{pmatrix} E_s & -2it\sin K_x a & -2it\sin K_y a \\ 2it\sin K_x a & E_p & 0 \\ 2it\sin K_y a & 0 & E_p \end{pmatrix} \begin{matrix} |s, \mathbf{K}\rangle_s \\ |p_x, \mathbf{K}\rangle_d \\ |p_y, \mathbf{K}\rangle_d, \end{matrix} \tag{4.4}$$

with tunneling energy $t = \int d\mathbf{r}\varphi_s(\mathbf{r} - \mathbf{D})H_{op}\chi_{px}(\mathbf{r})$ between the adjacent wells. For V_0 between $5E_R$ and $10E_R$, the tunneling t between neighboring deep and shallow wells is less than E_R. Simultaneously, we will require t to be equal to or larger than $\hbar\omega_z$. The eigenenergies of Eq. (4.4) are $\epsilon_{2,4}(\mathbf{K}) = (E_s + E_p \mp \sqrt{\Delta^2 + 4b(\mathbf{K})^2})/2$ and $\epsilon_3(\mathbf{K}) = E_p$, where detuning $\Delta = E_s - E_p$ and $b(\mathbf{K}) = 2t(\sin^2 K_x a + \sin^2 K_y a)^{1/2}$ is quasi-momentum dependent. The corresponding Bloch or eigenfunctions are $\Phi_{\alpha\mathbf{K}}(\mathbf{x}) = \langle \mathbf{x}|\alpha, \mathbf{K}\rangle$, where the label $\alpha = 2, 3$ and 4 stands for $2^{nd}, 3^{rd}$ and 4^{th} bands, respectively. The first band $\alpha = 1$ has Bloch functions constructed from the local ground state in the deep well. The Bloch functions for the second band are $|2, \mathbf{K}\rangle = i\cos\theta_{\mathbf{K}}|s, \mathbf{K}\rangle_s + \sin\theta_{\mathbf{K}}|+, \mathbf{K}\rangle_d$, where $\tan\theta_{\mathbf{K}} = 2b(\mathbf{K})/(-\Delta + \sqrt{\Delta^2 + 4b(\mathbf{K})^2})$ and

$$|+, \mathbf{K}\rangle_d = \frac{\sin K_x a|p_x, \mathbf{K}\rangle_d + \sin K_y a|p_y, \mathbf{K}\rangle_d}{\sqrt{\sin^2 K_x a + \sin^2 K_y a}}. \tag{4.5}$$

4.4 Band structure using plane wave basis

The 2D band structure for the single particle Hamiltonian H_{op} can be numerically solved in the plane wave basis $|\mathbf{k}\rangle$, where the non-zero matrix elements between $|\mathbf{K} + \mathbf{G}_{m,n}\rangle$ and $|\mathbf{K} + \mathbf{G}_{m',n'}\rangle$ are $E_R\left\{(K_x/k_L + m + n)^2 + (K_y/k_L + m - n)^2\right\} - V_0$

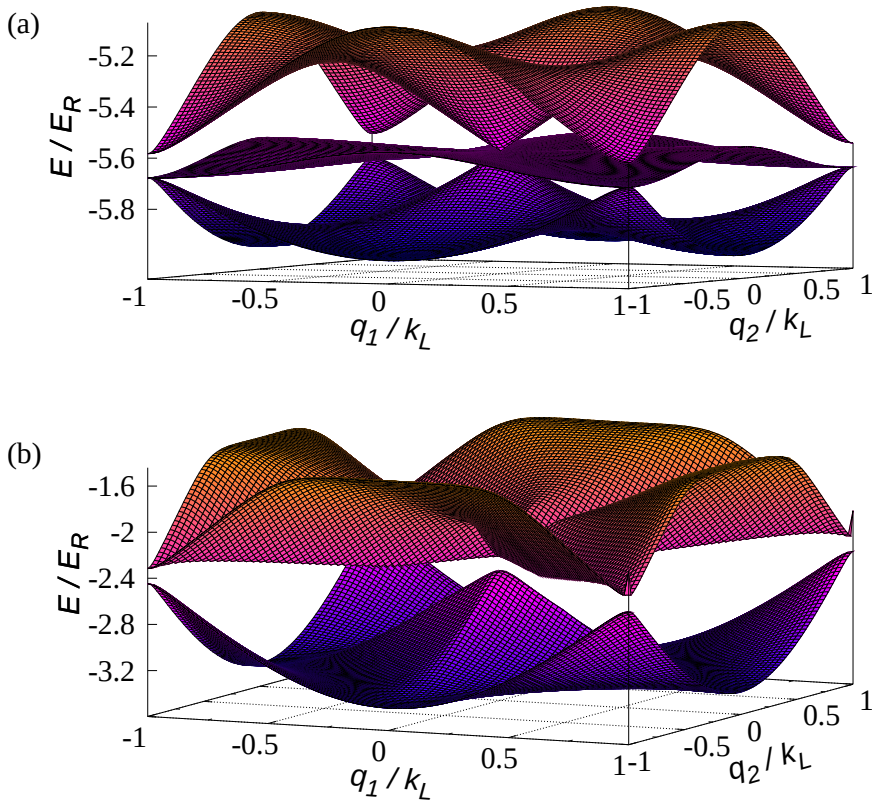

Figure 4.4: Band structure and hopping parameters. Panel(a) shows the numerical band structure at $|V_0| = 6E_R$ and $\theta = 0.42\pi$ for the 2^{nd}, 3^{rd} and 4^{th} bands as a function of the quasi momenta $\mathbf{q} = (q_1, q_2)$ in the first Brillouin zone. The second band has four degenerate minima at $(\pm k_L/2, \pm k_L/2)$, at the edge of the Brillouin zone. For the above set of parameters, the three bands touch at $\mathbf{K} = 0$. Panel(b) shows the numerical band structure for the 5^{th} and 7^{th} bands, which provide decay channels for collision-aided decay of the condensate.

for $m, n = m', n'$, $-V_0/4$ for $m = m' \pm 1$, $n = n' \pm 1$, and $-(V_0/2)\cos\theta$ for either of $m = m' \pm 1, n = n'$ or $m = m', n = n' \pm 1$.

It has energies $\epsilon_\alpha(\mathbf{K})$ and Bloch functions $\Phi_{\alpha\mathbf{K}}(\mathbf{x}) = \sum_{\mathbf{G}} e^{i(\mathbf{K}+\mathbf{G}).\mathbf{r}} C^{\alpha}_{\mathbf{G},\mathbf{K}}$. These energies $\epsilon_\alpha(\mathbf{K})$ for the 2^{nd}, 3^{rd} and 4^{th} band are shown in Fig. 4.4a for parameter set V_0 and θ where these three bands are degenerate at $\mathbf{K} = 0$. The 2^{nd} band has a maximum at $\mathbf{K} = 0$ and has band minima at $(\pm k_L/2, \pm k_L/2)$, the points where a Bose-Einstein condensate forms, also shown in Fig. 4.2b. Unlike in the tight binding model, the energy of the third band has a small momentum dependence. The band width of the 4^{th} band is significantly larger than what is predicted by the tight binding model. Figure 4.4b shows the higher 5^{th} and 7^{th} bands, which will provide collision-aided decay channels for the condensate formed in the second band. We have omitted other bands for clarity.

We ascertain the validity of the tight binding approximation by a comparison of the tunneling energy between unit cells with that obtained from the numerical band structure calculation. In particular, we compare the tunneling energy for band α between neighboring unit cells along the x axis, given by $J_\alpha = -(1/M)\sum_{\mathbf{K}} \epsilon_\alpha(\mathbf{K}) e^{i2a\mathbf{K}\cdot\hat{\mathbf{x}}}$ and the sum is over the quasi-momenta $\mathbf{K}$ in the first Brillouin zone. Results for bands $\alpha = 2, 3$ and 4 and $\theta = 0.42\pi$ are shown in Fig. 4.5 over the relevant range of lattice depths where the bands can touch. We find that the two methods agree to within 10% for the 2^{nd} band at lattice depth of $V_0 = 6E_R$ which is the point of degeneracy between the s and p states in adjacent wells. For other θ close to 0.42π, the results are similar. For the two higher bands the agreement is less satisfactory as we have restricted ourselves to a tight binding model

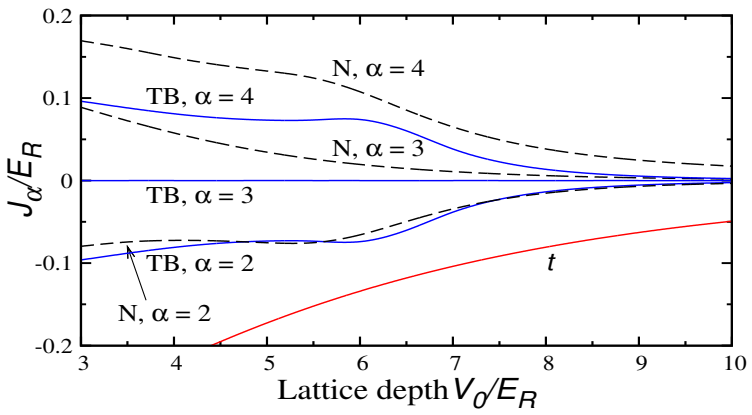

Figure 4.5: Tunneling energies J_α and t as a function of lattice depth V_0 at $\theta = 0.42\pi$. The solid blue and dashed black lines correspond to J_α between neighboring unit cells along the x axis for $\alpha = 2, 3, 4$ based on tight binding (TB) and exact numerical (N) plane wave simulations, respectively. Tunneling for $\alpha = 1$ is negligible, and the solid red line shows the tunneling energy t between the two wells in an unit cell.

comprising of three localized states only. As we will show later, for the main results of this chapter, the tight binding model is nevertheless sufficient. For example, the contribution of the 3^{rd} and 4^{th} bands to the thermodynamics of the problem will be small, and they do not provide channels for the condensate decay from the 2^{nd} band. Finally, we find that for larger well depths, the tunneling energy from the tight binding model is always smaller than the numerical estimate. This is because the dominant contribution to the hopping energy occurs in the classically forbidden region where the wave functions drop off exponentially. In these regions between the lattice sites, the anharmonic corrections to the potential, correctly treated in the numerical model, decrease the drop-off of the wave functions and give rise to larger tunneling energies.

4.5 Thermodynamics for the non-interacting Bose gas

We discuss the formation of a Bose-Einstein condensate for non-interacting bosons in the first excited or second band of the optical lattice. We study temperatures T such that $k_BT > t \gg \hbar\omega_z$, but k_BT is much less than the large band gap between the 4^{th} and 5^{th} band. Thus, for our parameters, we only need to consider population in the 2^{nd}, 3^{rd} and 4^{th} bands. As we will show, the fraction of condensed atoms is then small and therefore the picture of non-interacting bosons is appropriate. Furthermore, we will only present results using the tight binding model. This is sufficient as it gives a good representation of the second band and most atoms are in this band. Also, with realistic approximations the model leads to analytic expressions which allows us to study the parameter dependencies in detail.

Following Ref. [38], the total atom number $N = N_0 + \sum_{\alpha=2,3,4} \mathcal{N}_\alpha$, where N_0 is the number of atoms in the condensate at the minima of the second band, and

$$\mathcal{N}_\alpha = 2M\frac{a^2}{(2\pi)^2}\sum_{k=1}^{\infty}\sum_{n=0}^{\infty} z^k \int \frac{\mathrm{d}^2\mathbf{q}}{2} e^{-k\beta(\epsilon_\alpha(\mathbf{q})+n\hbar\omega_z)} \tag{4.6}$$

is the number of (non-condensed) atoms in band α excluding the condensed atoms. Here z is the fugacity, satisfying $0 \leq z \leq 1$ and $\beta = 1/k_BT$. The sum n is over all harmonic oscillator levels in the z direction and the integral over quasi momentum $\mathbf{K}$ or equivalently $\mathbf{q}$ is over the first Brillouin zone. The sum over k originates from a series expansion of the Bose distribution. We have set the zero of energy of the dispersion $\epsilon_\alpha(\mathbf{q}) = \epsilon_\alpha(\mathbf{K})$ at the minimum of the second band. Similarly the zero of energy of the harmonic oscillator is at the $n = 0$ level.

The maximum number of non-condensed atoms $\mathcal{N}_\alpha$ occurs at $z = 1$. Hence, condensation occurs when N is larger than the sum of the maximum non-condensed atom number in each band and thus for the remainder of the chapter we will assume $z = 1$ in Eq. (4.6). The integral over $\mathbf{q}$ is straightforward for the third band as its energy is independent of $\mathbf{q}$, but requires more thought for the other two bands. We are interested in the number of atoms occupying energy levels close to the bottom of the second band where $1 + \cos q_1 a \cos q_2 a = 0$. Taylor expanding the energy of both the 2^{nd} and 4^{th} bands to first order in $1+\cos q_1 a \cos q_2 a$ gives $\epsilon_2(\mathbf{q}) \approx [t/F(\Delta/t)](1+\cos q_1 a \cos q_2 a))$ and $\epsilon_4(\mathbf{q}) \approx 4tF(\Delta/t) - [t/F(\Delta/t)](1 + \cos q_1 a \cos q_2 a))$, where $F(x) = \sqrt{2 + x^2/16}$. The integrand $\exp(-k\beta\epsilon_\alpha(\mathbf{q}))$ is separated into a momentum dependent and an independent part. The momentum independent part becomes a simple pre-factor. Using that $\beta t/F(\Delta/t) \ll 1$, the momentum dependent part of the integral is solved to $O([\beta t/F(\Delta/t)]^2)$. We have checked that this approximation to the integral over $\mathbf{q}$ is comparable to a numerical estimate of the same. We can perform the sum over n exactly. Then assuming that $\hbar\omega_z \ll k_B T$, the sum over k can be performed.

Finally, we have

$$\mathcal{N}_2 \approx M\frac{k_B T}{\hbar\omega_z}\log\left[\frac{1}{1-e^{-\frac{\beta t}{F(\Delta/t)}}}\right], \tag{4.7}$$

$$\mathcal{N}_3 \approx M\frac{k_B T}{\hbar\omega}\log\left[\frac{1}{1-e^{-2\beta t F(\Delta/t)}}\right], \tag{4.8}$$

$$\mathcal{N}_4 \approx M\frac{k_B T}{\hbar\omega}\log\left[\frac{1}{1-e^{-\beta t\left(4F(\Delta/t)-\frac{1}{F(\Delta/t)}\right)}}\right], \tag{4.9}$$

which are even functions of Δ.

Figure 4.6a shows the dependence of the condensate fraction N_0/N on the

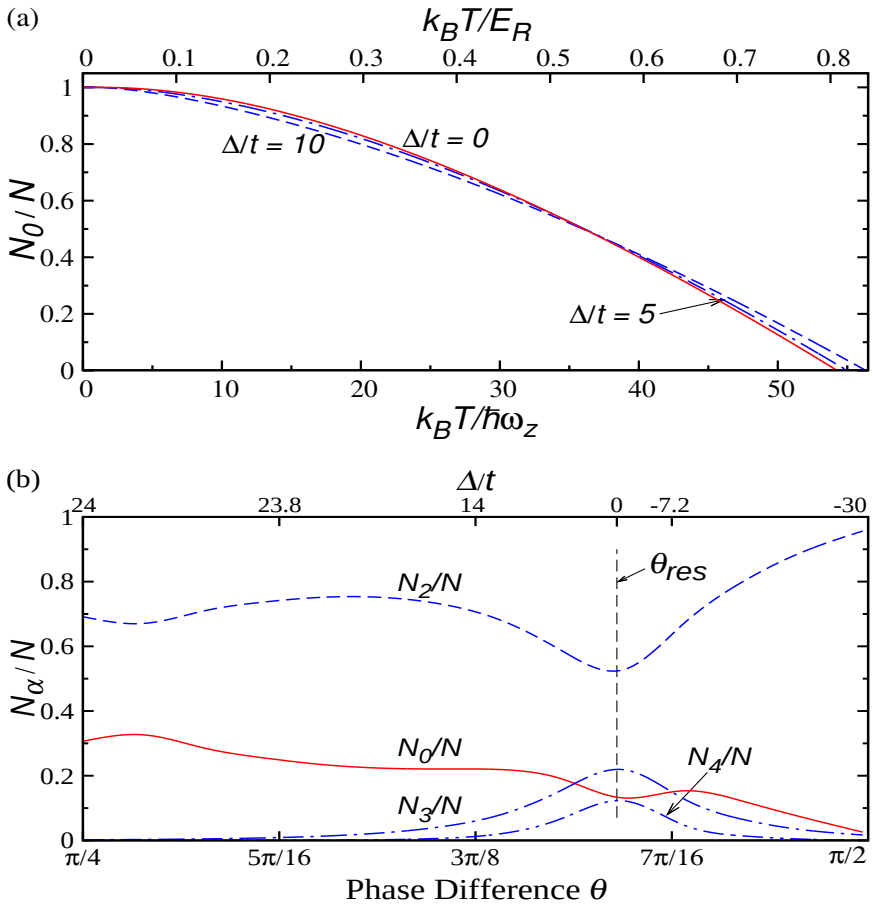

Figure 4.6: Panel (a) shows the condensate fraction as a function of $k_BT/\hbar\omega_z$ (bottom axis) and k_BT/E_R (top axis), for three values of Δ/t. We used $V_0 = 6E_R$ and the values of Δ/t correspond to $\theta = 0.420\pi, 0.405\pi$, and 0.389π for increasing Δ. The frequency of the harmonic trap along the z direction is 30Hz or $\hbar\omega_z = 0.015E_R$, which is a typical experimental value, leading to $t = 10\hbar\omega_z$ for $\Delta = 0$. Finally, $\nu = N/M = 200$. Panel (b) shows N_0/N and the non-condensed fractions $\mathcal{N}_\alpha/N$ as a function of θ and Δ/t for $k_BT = 50\hbar\omega_z = 0.74E_R$. The non-linear x axis on the top of the figure shows the corresponding Δ/t values. Between $\theta = \pi/4$ and $5\pi/16$ the value of Δ/t do not change significantly. Other parameters are as in Panel (a). The value of $|\Delta|/t$ is zero at the point of degeneracy with $\theta = \theta_{res}$, and increases as we move away from resonance.

temperature for various values of detuning Δ/t, where the s orbital in the shallow well is or is nearly degenerate with the p orbitals in the deep well. For a lattice depth V_0, the different ratios of Δ/t can be obtained by appropriately choosing θ. The temperature at which $N_0/N \to 0$ is the critical temperature T_c. We see that $k_B T_c \gg \hbar\omega_z$ for reasonable Δ/t and, thus, is consistent with the approximations that we have made. Moreover, our assumption of non-interacting atoms is valid for T near T_c where the fraction of atoms in the condensate is much smaller than one.

Figure 4.6b shows the dependence of N_0/N and $\mathcal{N}_\alpha/N$ on θ and Δ/t for T just below T_c. We first note that for θ close to θ_{res}, the dependence of Δ/t with θ is linear. This linearity persists for $\theta_{res} \leq \theta \leq \pi/2$, but for $\theta < \theta_{res}$, Δ/t increases and then saturates. For the parameters shown the number of atoms in the second band $N_0 + \mathcal{N}_2$ is larger than 60% of all atoms. At the degeneracy point, $\Delta = 0$ and $N_0 + \mathcal{N}_2$ is smallest. At this point, the bands touch, and consequently the atom population in the 3^{rd} and 4^{th} bands are highest. Nevertheless, the populations in bands $\alpha = 3$ and 4 are sufficiently small such that the tight binding approximation remains valid.

4.6 Lattice transformation and final temperature

As discussed in Section 4.1, populating the higher bands is a two step process. In step 1, the angle θ is chosen such that the deep wells are significantly deeper than the neighboring shallow wells, and the atoms are confined to the local ground states of these deep wells, as shown in Fig. 4.1a. The atoms are confined in the transverse

directions, but distributed in the z harmonic oscillator states with a temperature T_i. In step 2, θ is changed to reach the final lattice configuration. We model this change to be fast with respect to tunneling energies between adjacent wells, but adiabatic with respect to the onsite energies of the well to which the atoms have been confined. Thus, just after the final θ is reached, the atoms are still confined to the ground s state of these wells, which now happen to be the shallow wells (Fig. 4.1a). We refer to this state as the initial state just after the lattice transformation, and the temperature for this state is still T_i. With the s orbitals now tuned to resonance with the adjacent p orbitals, the atoms gets distributed to the entire 2D lattice as well as to harmonic levels in the transverse direction due to tunneling and elastic collisions. The atoms thermalize, and condense to the four quasi-momenta at the edges of the first Brillouin zone of the second band. We refer to this state as the final state, and the temperature reached after thermalization as T_f.

We have calculated the final temperature using conservation of total number of atoms and total energy, and find an analytic expression between T_i and T_f. Figure 4.7 shows the dimensionless final temperature $k_B T_f/\hbar\omega_z$ as a function of the phase difference θ. We see that for the two initial temperatures shown in the figure the final temperature T_f is a monotonically decreasing function of θ, can lie either above or below the critical temperature T_c, but is nearly always larger than T_i. At the point of degeneracy between the adjacent s and p orbitals, T_f lies just below the critical temperature T_c, and the gas remains condensed. Nevertheless, this temperature is larger than the corresponding initial temperature. We have $T_f > T_i$ since the energy of the initial state E_s is greater than the bottom of the

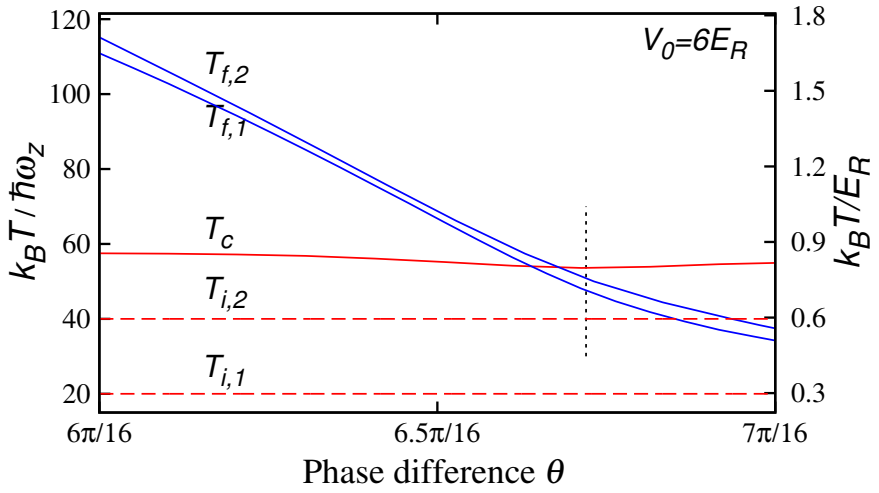

Figure 4.7: The final temperature $T_{f,1}$ and $T_{f,2}$ (solid blue lines) in units of $\hbar\omega_z/k_B$ (left axis) or E_R/k_B (right axis) after the lattice transformation as a function of the phase difference θ for two initial temperatures, $T_{i,1} = 20\hbar\omega_z/k_B$ and $T_{i,2} = 40\hbar\omega_z/k_B$, respectively. (Equivalently, we have $T_{i,1} = 0.3E_R/k_B$ and $T_{i,2} = 0.6E_R/k_B$, respectively). We use atom number per lattice site $\nu = N/M = 200$ and lattice depth $V_0 = 6E_R$. The initial temperatures are shown as dashed horizontal lines. The vertical dotted lines represent the angle θ at which the s and p orbitals of adjacent wells are degenerate. For fixed atom number the critical temperature T_c (solid red line) of the final lattice weakly depends on the lattice parameters but is independent of T_i.

second band, $\epsilon_2(\mathbf{K_0})$ at quasi-momentum $\mathbf{K_0}$. Elastic collisions then redistribute this excess energy over the harmonic oscillator levels as well as the different quasi momenta in the $2D$ plane and the temperature will increase. On the other hand the energy difference $E_s - \epsilon_2(\mathbf{K_0})$ decreases with θ so that T_f decreases with θ.

Thus the lattice transformation typically leads to heating of the atom cloud. For a given atom number ν and initial temperature T_i, there is a limited range of final lattice parameters V_0 and θ for which the final temperature T_f lies below the corresponding critical temperature T_c. At the point of degeneracy of the adjacent s and p orbitals, even for significantly low initial temperatures T_i, the final temperature T_f is large and lies close to the corresponding critical temperature T_c. At this final temperature, the fraction of condensed atoms will be small, and thus our picture of non-interacting atoms should hold.

4.7 Lifetime estimate of the condensate

The atoms in the higher bands decay to the ground band by atom-atom collisions. In this section we will determine the rate for these processes. To obtain the decay rates, we use the picture of a discrete level coupled to a continuum as discussed in Complement $\mathrm{C_I}$ in Ref. [138]. These rates can also be obtained using the Fermi Golden rule. First, we rewrite our interaction Hamiltonian H_{int} in terms of the eigenstates or modes of H_0. In other words, we expand bosonic operators $\psi(\mathbf{x}) = \sum_{\alpha\mathbf{K}m} \Phi_{\alpha\mathbf{K}}(\mathbf{x})\varphi_m(z)a_{\alpha\mathbf{K}m}$, where $a_{\alpha\mathbf{K}m}$ is the annihilation operator of an atom in Bloch function $\Phi_{\alpha\mathbf{K}}(\mathbf{x})$ and the m^{th} harmonic oscillator wave function $\varphi_m(z)$

along the z direction.

Our initial state is an incoherent thermal mixture of normalized discrete states $|\Phi\rangle = (\sum_{\mathbf{K_0}} \eta_{\mathbf{K_0}} a^\dagger_{2,\mathbf{K_0},0})^{N_0} (a^\dagger_{2,\mathbf{K},m'})^{n(\mathbf{K},m')}|0\rangle/Z$ where $|0\rangle$ is the vacuum of no atoms and $Z = \sqrt{N_0! n(\mathbf{K},m')!}$. These states $|\Phi\rangle$ only contain atoms in the second band. Decay from atoms in other bands is less important as in Section V we showed that most atoms are in the second band. Atoms in modes $2, \mathbf{K_0}, 0$ are the condensed atoms while atoms in modes $2, \mathbf{K}, m'$ with $\mathbf{K}, m' \neq \mathbf{K_0}, 0$ are non-condensed atoms. The superposition $\sum_{\mathbf{K_0}} \eta_{\mathbf{K_0}} a^\dagger_{2,\mathbf{K_0},0}$ is over the two quasi-momenta $\mathbf{K_0} = (k_L/2, k_L/2)$ and $\mathbf{K_0} = (k_L/2, -k_L/2)$, where the energy of the 2^{nd} band is minimal, and the coefficient $\eta_{\mathbf{K_0}} = 1/\sqrt{2}$ when the momentum in the x and y direction has the same sign and is $i/\sqrt{2}$ otherwise [46], [45]. The positive integer $n(\mathbf{K}, m')$ is the number of atoms in quasi momentum $\mathbf{K}$ and harmonic oscillator level m' given by the Bose distribution.

Each of the normalized discrete states decays to the continuum states $|\mathbf{Q}\rangle$ given by $a^\dagger_{1,\mathbf{K}_1,m} a^\dagger_{\alpha,\mathbf{K}_2,n} (\sum_{\mathbf{K}_0} \eta_{\mathbf{K}_0} a_{2\mathbf{K_0},0})^2 |\Phi\rangle/\sqrt{N_0(N_0-1)}$ and $a^\dagger_{1,\mathbf{K}_1,m} a^\dagger_{\alpha,\mathbf{K}_2,n} a_{2\mathbf{K_0},0}\, a_{2,\mathbf{K},m'}$ $|\Phi\rangle/\sqrt{N_0 n(\mathbf{K},m')}$, which corresponds to states where either two atoms or one atom decays from the condensate, respectively, to other allowed modes. Energy conservation requires that at least one of the atoms in the continuum state occupies the ground $\alpha = 1$ band, while the second atom can either be in the ground or any higher band. Discrete states $|\Phi\rangle$ and $|\Phi'\rangle$ decay to different orthogonal continuum states $|\mathbf{Q}\rangle$ and $|\mathbf{Q}'\rangle$, respectively.

Certain decay processes involving matrix elements with bands $\alpha > 2$ are only energetically allowed for sufficiently large lattice depths or large detuning Δ between

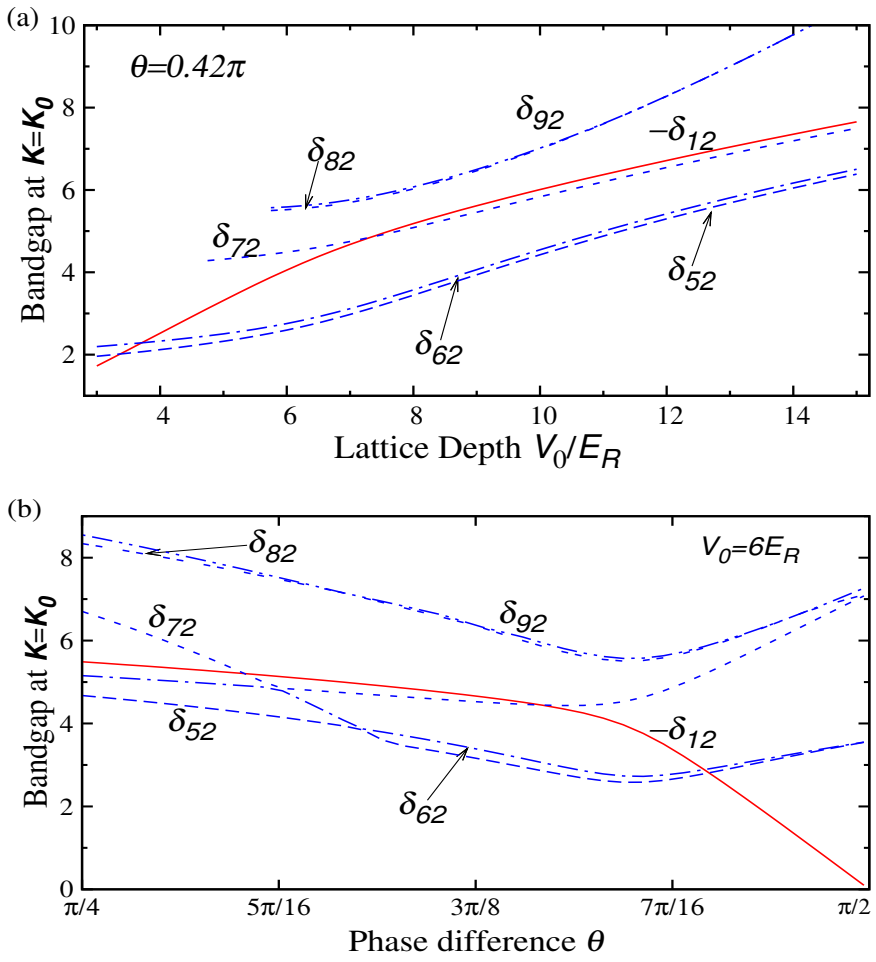

Figure 4.8: Band gaps $\delta_{\alpha 2} = \epsilon_\alpha(\mathbf{K_0}) - \epsilon_2(\mathbf{K_0})$ between band α and the 2^{nd} band at one of the condensate momenta. Panel (a) shows the band gaps as a function of lattice depth at $\theta = 0.42\pi$. For $\alpha = 1$ (solid red line) we plot the negative of the band gap. Energy conservation requires that allowed decay processes satisfy $\delta_{\alpha 2} \leq -\delta_{12}$. In other words, for allowed processes, curves $\delta_{\alpha 2}$ with $\alpha > 2$ must lie below the solid red line. The excess energy $\delta_{12} + \delta_{\alpha 2}$ is lost to the oscillator in the z direction. Bands $\alpha \geq 7$ only exist for sufficiently deep wells. The angle θ is chosen such that for $V_0 = 6E_R$, the s and p orbitals in adjacent wells are degenerate. Panel (b) shows the band gaps as a function of the phase difference θ at lattice depth $V_0 = 6E_R$. Depending on the value of θ, there are one or more allowed decay processes.

adjacent s and p orbitals. In Fig. 4.8a we plot the band gap $\delta_{\alpha 2} = \epsilon_\alpha(\mathbf{K_0}) - \epsilon_2(\mathbf{K_0})$ as a function of the lattice depth V_0 for a certain angle θ. Due to energy conservation, decay is only allowed when $\delta_{12} \geq -\delta_{\alpha 2}$. For typical θ and V_0, decay processes involving bands $\alpha > 7$ do not exist, and those involving the 7^{th} band are allowed only beyond a certain lattice depth. Decay process involving bands $\alpha = 2, 3$ and 4 are ruled out by parity considerations, and hence not shown in Fig. 4.8a. Using similar arguments, we can check which decay processes contribute at a particular θ from Fig. 4.8b, where we plot $\delta_{\alpha 2}$ as a function of phase difference θ for a certain lattice depth V_0.

The interaction Hamiltonian takes the form

$$H_{int} = \frac{g}{2} \sum I^{mnm'n'}_{\alpha\beta\alpha'\beta'}(\mathbf{K}_1, \mathbf{K}_2, \mathbf{K}_3, \mathbf{K}_4) a^\dagger_{\alpha \mathbf{K}_1 m} a^\dagger_{\beta \mathbf{K}_2 n} a_{\alpha' \mathbf{K}_3 m'} a_{\beta' \mathbf{K}_4 n'}, \tag{4.10}$$

where the sum is over all indices and quasi-momenta. We can write down the matrix element as $I^{mnm'n'}_{\alpha\beta\alpha'\beta'}(\mathbf{K}_1, \mathbf{K}_2, \mathbf{K}_3, \mathbf{K}_4) = O^{mn}_{m'n'} P^{\alpha\beta}_{\alpha'\beta'}(\mathbf{K}_1, \mathbf{K}_2, \mathbf{K}_3, \mathbf{K}_4)$, where $O^{mn}_{m'n'}$ is an integral over four harmonic-oscillator wave functions along the z axis, and $P^{\alpha\beta}_{\alpha'\beta'}(\mathbf{K}_1, \mathbf{K}_2, \mathbf{K}_3, \mathbf{K}_4)$ involves an integral over four Bloch functions.

The function $O^{mn}_{m'n'}$ can be found exactly [139] and is non-zero only when $n + m + m' + n'$ is even. For our calculations, we only require matrix elements with $n' = 0$ and $0 \leq m' \ll m, n$ and an approximate form of the result proves to be more useful for summing up the contributions to the loss rate. For the square of the function, we find $(O^{mn}_{00})^2 \approx e^{-s^2/r}/(2\pi^2 l_z^2 r)$ for $m' = 0$, and

$$(O^{mn}_{m'0})^2 \approx \frac{1}{2\pi^2 l_z^2 r \Gamma(m'+1)} \left(\frac{s^2}{r}\right)^{m'} e^{-s^2/r}, \tag{4.11}$$

for $m' \geq 1$. Here $2r = m + n$ and $2s = m - n$. The selection rules for $O^{mn}_{m'0}$

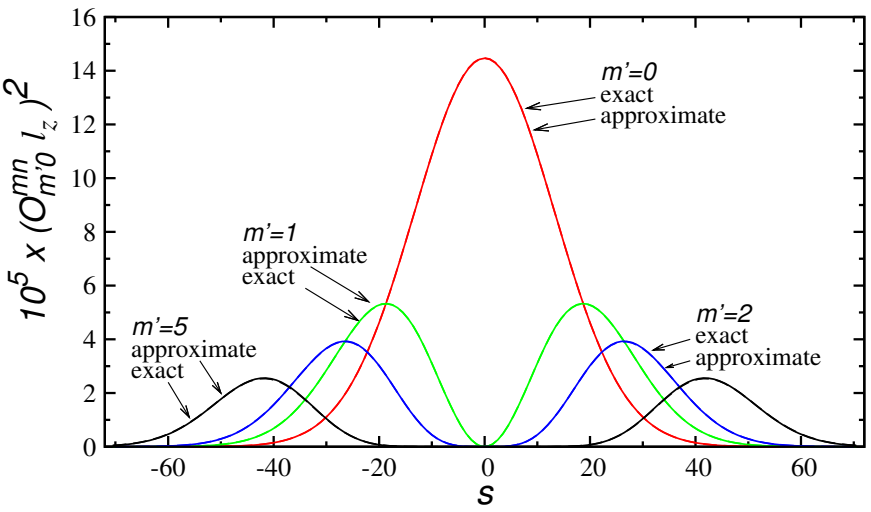

Figure 4.9: The square of the matrix element $O^{mn}_{m'0}$ as a function of $s = (m-n)/2$ with $r = (m+n)/2 = 350$. This large value for r is typical for both atoms decaying from the second to the lowest band. The curves are for $m' = 0, 1, 2$, and 5. The solid curves are exact analytic evaluation of $O^{mn}_{m'0}$ while the indistinguishable dashed curves correspond to approximate evaluations assuming $n + m \gg m'$.

require that r and s are integers when m' is even and half-integers when m' is odd. Figure 4.9 shows a comparison of the exact and approximate form of the function $O^{mn}_{m'0}$ for a fixed large r. For all m', the approximate form is in good quantitative agreement with the exact. Furthermore, we see that $O^{mn}_{m'0}$ is significant only when $s \ll r$, i.e. when n and m are relatively close. The function peaks at $s = \pm\sqrt{m'r}$.

The function $P^{\alpha\beta}_{\alpha'\beta'}(\mathbf{K}_1, \mathbf{K}_2, \mathbf{K}_3, \mathbf{K}_4)$ is either numerically evaluated in the plane wave basis or is analytically determined in the tight binding model. Bands $\alpha \leq 4$ are always treated in the tight binding model while higher bands are treated numerically in the plane wave basis. The function $P^{\alpha\beta}_{\alpha'\beta'}$ is non-zero when $\mathbf{K}_1 + \mathbf{K}_2 = \mathbf{K}_3 + \mathbf{K}_4$

mod $\mathbf{G}$. For our calculations, we only require matrix elements with $\alpha' = \beta' = 2$ and one or both of $\mathbf{K}_3$, $\mathbf{K}_4$ equal the condensate momenta $\mathbf{K_0}$. We then find

$$P_{22}^{\alpha\beta}(\mathbf{K}_1, \mathbf{K}_2, \mathbf{K}, \mathbf{K}_0) = \frac{\sin\theta_{\mathbf{K_0}} \sin\theta_{\mathbf{K}}}{4\sqrt{2}M\pi l_d^2} f^{\alpha\beta}(\mathbf{K}_1, \mathbf{K}_2, \mathbf{K}).$$

We find analytically $f^{11}(\mathbf{K}_1, \mathbf{K}_2, \mathbf{K}) = (\sin K_x a \pm \sin K_y a)/\sqrt{\sin^2 K_x a + \sin^2 K_y a}$ for $\alpha, \beta = 1, 1$, and the $\pm$ sign corresponds to the case $\mathbf{K_0} = (\pi/2a, \pi/2a)$ and $(\pi/2a, -\pi/2a)$, respectively. This matrix element is independent of $\mathbf{K}_1$ and $\mathbf{K}_2$ as $\alpha = 1$ is a flat band in the tight binding approximation. If $\mathbf{K}_0 = (\pi/2a, \pi/2a)$ and $\mathbf{K} = (\pi/2a, -\pi/2a)$, the matrix element is zero and vice-versa. Thus, collisions involving atoms in two inequivalent condensate quasi-momenta do not lead to condensate decay.

The matrix elements $P_{22}^{1\alpha}$ with $\alpha = 2, 3, 4$ are zero because of parity considerations, and this has also been checked numerically. For $P_{22}^{1\alpha}$ with $\alpha > 4$, the integral is solved numerically using the tight binding wave functions for bands 1 and 2 but the numerical wave functions for band α expressed in terms of the $C_{\mathbf{G},\mathbf{K}}^{\alpha}$ defined in Sec. 4.4. We find that $P_{22}^{11} > P_{22}^{1\alpha}$ for $\alpha \neq 1$, independent of quasi-momenta $\mathbf{K}$. This is also confirmed by the tight binding model. Finally, close to $\theta = \theta_{res}$, for bands $\alpha > 4$, P_{22}^{17} is the most dominant term.

After having evaluated the matrix elements, we are now ready to estimate the collisional loss rates for a condensed gas of atoms at temperature T and total atom number N. This loss is dominated by pairs of atoms in the second band decaying to bands $\alpha = 1$ and $\beta > 4$. Following the discussion in Complement C_I in Ref. [138] and summing over all populated discrete states $|\Phi\rangle$, these rates per unit cell are

given by

$$\Gamma_{22\to 1\alpha} = \frac{N_0(N_0-1)}{2M^2}\gamma_{22\to 1\alpha}(\mathbf{K_0},0) + \sum_{\mathbf{K},m'}\frac{N_0 n(\mathbf{K},m')}{M^2}\gamma_{22\to 1\alpha}(\mathbf{K},m'), \tag{4.12}$$

where

$$\gamma_{22\to 1\alpha}(\mathbf{K},m') = \frac{E_R}{\hbar}(k_L a_s)^2\frac{\pi M\Gamma(m'+1/2)}{\Gamma(m'+1)}\sum_{\mathbf{K}_1,\mathbf{K}_2}{}' \left[P_{22}^{1\alpha}(\mathbf{K}_1,\mathbf{K}_2,\mathbf{K},\mathbf{K}_0)/k_L^2\right]^2 \times \frac{\Gamma(-\delta/(2\hbar\omega_z)+1/2)}{\Gamma(-\delta/(2\hbar\omega_z)+1)}, \tag{4.13}$$

$\delta = \epsilon_1(\mathbf{K}_1)+\epsilon_\beta(\mathbf{K}_2)-\epsilon_2(\mathbf{K}_0)-\epsilon_2(\mathbf{K})$, and the prime in the momentum sum indicates that it has to conserve quasi-momentum. The rates $\gamma_{22\to 1\alpha}(\mathbf{K},m')$ are independent of M and sums over harmonic oscillator indices have been performed analytically using the approximate form of $O^{mn}_{m'0}$.

The first term in Eq. (4.12) describes loss processes where two condensed atoms at quasi momentum $\mathbf{K_0}$ and harmonic oscillator level $m'=0$ are lost. The second term describes the sum of loss processes where one condensed atom and another non-condensed atom at quasi momentum $\mathbf{K}$ and harmonic oscillator level m' from the second band are lost.

For the decay process where both atoms are removed from the condensate and decay to the ground band $\alpha,\beta = 1$, we can write down an analytical expression using the tight binding model. For $\Delta > 0$ it is

$$\gamma_{22\to 11}(\mathbf{K_0},0) = \frac{V_0}{\hbar}(k_L a_s)^2(1+\cos\theta)\frac{\sin^4\theta_{\mathbf{K_0}}}{16\sqrt{\pi}}\sqrt{\frac{\omega_z}{\omega_d}},$$

where we have used $\delta \approx 2\hbar\omega_d$ and $\omega_z \ll \omega_d$. For $\Delta < 0$, we have to replace $\sin\theta_{\mathbf{K_0}}$ by $\cos\theta_{\mathbf{K_0}}$.

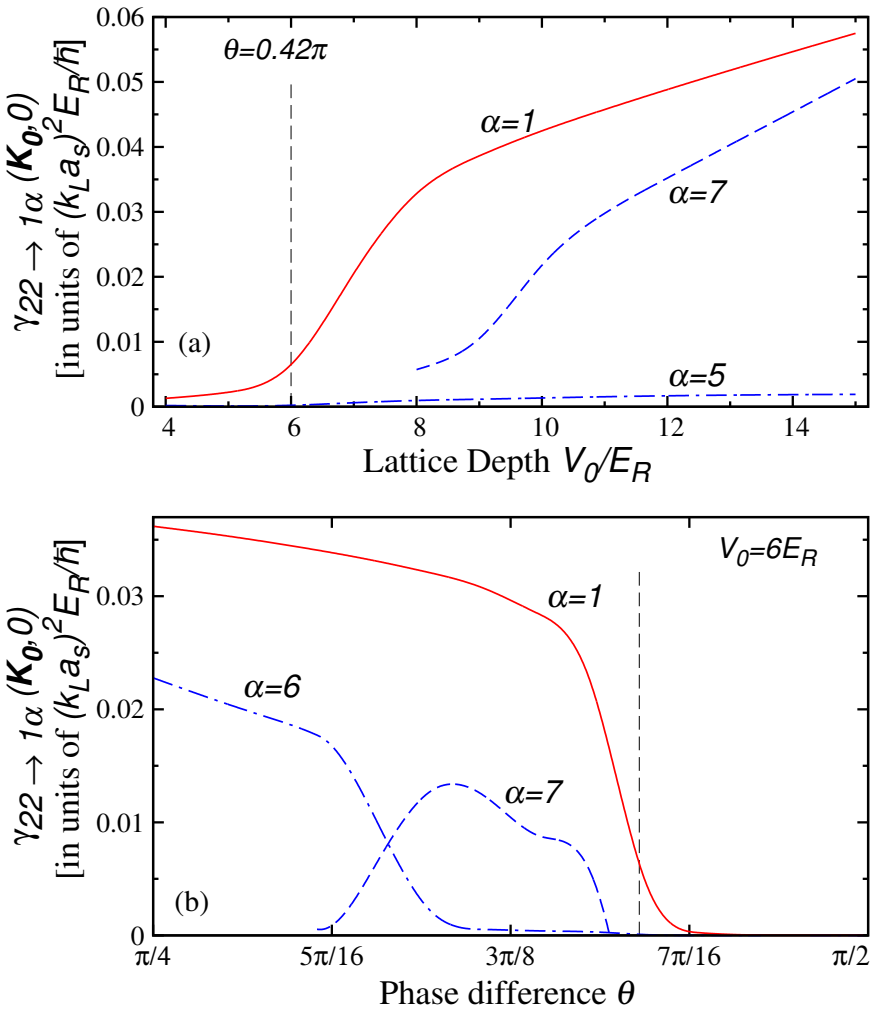

Figure 4.10: Decay rates $\gamma_{22\to 1\alpha}(\mathbf{K_0}, 0)$ for various bands α, where two atoms are lost from the condensate, one going to the ground band and another to band β. Panel (a) shows the decay rates as a function of lattice depth V_0/E_R at $\theta = 0.42\pi$. The decay rate to band $\alpha = 6$ is negligible and not shown in the figure. Decay processes involving still higher bands are energetically disallowed. The vertical dashed line indicates the lattice depth where the adjacent s and p orbitals are degenerate. Panel (b) shows the decay rates as a function of θ at lattice depth $V_0 = 6E_R$. Depending on the value of θ, decay to higher bands $\alpha = 6$ and 7 becomes important. The vertical dashed line indicates the angle θ where the adjacent s and p orbitals are degenerate.

Figure 4.10a shows $\gamma_{22\to 1\alpha}(\mathbf{K_0}, 0)$ based on Eq. (4.13) as a function of lattice depth V_0/E_R at $\theta = 0.42\pi$. The decay to the ground band is largest, followed by decay to the 7^{th} band, which is energetically allowed at lattice depths $V_0 > 8E_R$. For $V_0 > 8E_R$ within the tight binding model, the local orbitals d_{x^2}, d_{y^2} and d_{xy} in the deep well form the basis for the $5^{th}, 6^{th}$ and 7^{th} bands. Moreover, only the 7^{th} band has significant d_{xy} character at $\theta = 0.42\pi$. We can then show that decay contributions to these three bands are significant only when the final state involves d_{xy} orbitals and, hence, only the 7^{th} band has significant losses. Also, with increasing lattice depth, the harmonic-oscillator length in the deep well increases, leading to a much tighter confinement of the atoms. Thus, the decay rate increases with increasing lattice depths.

Figure 4.10b shows $\gamma_{22\to 1\alpha}(\mathbf{K_0}, 0)$ as a function of the phase difference θ at lattice depth $V_0 = 6E_R$. Decay to the ground band is again the dominant term, followed by contribution to the 6^{th} and 7^{th} bands, depending on the phase difference θ. The steep decrease in the $\alpha = 1$ decay rate near $\theta = \theta_{res}$ with increase of θ is due to the change in character of the condensate wave function from predominantly p state in the deep well to s state in the shallow well. (The sharp increase of the $\alpha = 1$ rate in Fig. 4.10a has a similar origin.) The behavior of the loss rates of the 6^{th} and 7^{th} bands can be understood from studying Figs.4.3 and 4.8b. Between $\theta = \pi/4$ and $3\pi/8$ the three d orbitals in the deep wells and the s orbital in the shallow well are in resonance near $\theta = 0.3\pi$ with tunneling energies that are of order of the splittings. For $\theta < 0.3\pi$, the 6^{th} band has predominant d_{xy} character and is the only band that has a significant loss rate. For $\theta > 0.3\pi$, it is the 7^{th} band that has significant

d_{xy} character. For $\theta > 0.4\pi$, loss to $\alpha = 7$ is not energetically allowed. Also with decreasing θ, the harmonic-oscillator length in the deep well increases, and thereby the decay rate increases with decreasing θ.

The total decay rate Γ is obtained by summing over contributions from all bands α. To a good approximation, this is given by

$$\Gamma \approx \sum_{\alpha} \left(\frac{\nu^2}{2} + \nu \frac{k_B T}{\hbar\omega_z} \sqrt{\frac{\pi\hbar\omega_z}{t/F\,(\Delta/t)}} \right) \gamma_{22\to 1\alpha}(\mathbf{K_0}, 0), \tag{4.14}$$

where $\nu = N/M$, the total number of atoms per unit cell. The above result is reached by first performing the sums over $\mathbf{K}_1$ and $\mathbf{K}_2$ in Eq. 4.13 neglecting the quasi momentum dependence of the first and second band in δ, since their band widths are negligible compared to the band gaps. We then find

$$\frac{\gamma_{22\to 1\alpha}(\mathbf{K}, m')}{\gamma_{22\to 1\alpha}(\mathbf{K_0}, 0)} = \frac{\Gamma(m'+1/2)}{\sqrt{\pi}\Gamma(m'+1)} \frac{\sin^2\theta_{\mathbf{K}}(\sin(K_x a) + \sin(K_y a))^2}{\sin^2\theta_{\mathbf{K_0}}(\sin(K_{0x} a) + \sin(K_{0y} a))^2}, \tag{4.15}$$

which separates its $\mathbf{K}$ and m' dependence. We further note that $n(\mathbf{K}, m') = \sum_{k=1}^{\infty} z^k \exp[-k\beta(\epsilon_2(\mathbf{K}) + m'\hbar\omega_z)]$, and using this, we can perform the sum over m' analytically. The sum over $\mathbf{K}$ can be performed in a manner similar to that used in determining the total atom number in section 4.5 and noting that $\epsilon_2(\mathbf{K})$ is an even function of both K_x and K_y so that only the even part of $\gamma_{22\to 1\alpha}(\mathbf{K}, m')$ contributes to the sums. The energy $\epsilon_2(\mathbf{K})$ is Taylor expanded as before around $\mathbf{K} = \mathbf{K_0}$ and the exponential $\exp[-k\beta(\epsilon_2(\mathbf{K})]$ separated into a momentum dependent and independent part leading to an integral that is solved to $O([\beta t/F\,(\Delta/t)]^2)$. Finally, we find the result of Eq. 4.14.

Figure 4.11 shows the total decay rate in units of the tunneling energy defined in section 4.3 as a function of the phase difference θ for various temperatures below

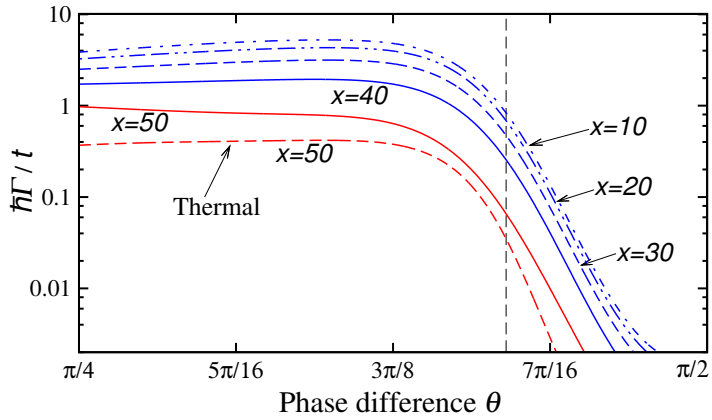

Figure 4.11: Dimensionless decay rate $\hbar\Gamma/t$ as a function of phase difference θ for ^{87}Rb atoms at $V_0 = 6E_R$ and $\nu = 200$. Curves correspond to various values of dimensionless temperature $x = k_BT/\hbar\omega_z$. Vertical dashed line represent $\theta = \theta_{res}$ at which the neighboring s and p orbitals are degenerate. Dashed red curve shows the thermal contribution to the decay rate at $x = 50$.

the critical temperature T_c. The red curve is at $k_BT = 50\hbar\omega_z$, which is closest to the critical temperature. For $\theta < \theta_{res}$, the loss rates are large but weakly dependent on θ while for large θ the loss rates rapidly decrease. Qualitatively the curves follow the behavior of $\alpha = 1$ loss rates shown in Fig. 4.10b. The slight deviations between the curves at different temperatures are due to a non-trivial redistribution of atoms between the condensate and the thermal component. Figure 4.11 also shows the loss rate from the thermal atoms for $k_BT/\hbar\omega_z = 50$. Near $\theta = \theta_{res}$, it corresponds to about 50% of the total loss. For smaller temperatures, the contribution from the thermal atoms becomes smaller.

We want to make a final observation about the use of the tight binding model. The decay rates involving bands $\alpha = 3$ and 4 are zero both in the tight binding

approximation and for the exact evaluation of their wavefunctions. Hence, the fact that the tight binding model is insufficient for bands $\alpha = 3$ and 4 does not affect the decay rates. For bands $\alpha \geq 5$, we have used the numerical wavefunctions.

4.8 Conclusion

We have studied two aspects of Bose-Einstein condensates formed in the second band of a 2 dimensional optical lattice with weak harmonic confinement in the third direction. The first aspect relates to the lattice transformation process that leads to atom population in excited bands, and the subsequent thermalization process in the excited bands. A non-interacting Bose gas picture provides analytic expressions for the condensed fraction of atoms and the corresponding critical temperature T_c as a function of lattice parameters reached after the lattice transformation. These crucially depend on Δ, the detuning between the adjacent s and p orbitals. The analysis shows that $k_B T_c > t \gg \hbar\omega_z$ and the condensed fraction is minimal at $\Delta = 0$. We also show that the lattice transformation process, in general, leads to a heating of the atom cloud. For large positive detuning Δ, this heating is significant, and the final temperature $T_f \gg T_c$. At $\Delta = 0$, which is the case of interest since the adjacent s and p orbitals are degenerate at this detuning, even for $T_i \approx 0$, T_f is large but still just below the corresponding T_c. Thus, after thermalization, the condensed fraction in the excited band is small.

The second aspect deals with the lifetime of the condensate formed in the second band of the optical lattice, which is determined by atom-atom elastic collisions.

All such decay processes only involve the deep wells, since one or both of the colliding atoms decay to quasi momentum states in the ground band, which in the tight binding picture are predominantly determined by the localized ground states in the deep well. The available oscillator states along the z axis ensure that for all lattice parameters, there exist a dominant decay process in which two atoms from the second band, undergoing elastic collisions, both decay to the ground band. The excess energy is released into excitations in the z oscillator levels. At detuning $\Delta \leq 0$, the above process is then the only energetically-allowed decay process. We provide analytical results for this process as function of lattice parameters, atom number and temperature using the tight binding model. We show that the contribution to this decay from thermal atoms in the second band is significant. For $\Delta > 0$ and depending on lattice depth, other channels involving the 5^{th}, 6^{th} or 7^{th} band contribute to the decay process. These decay rates are determined using tight binding results for bands $\alpha \leq 4$ and numerical results for bands $\alpha > 4$. We show that at temperatures close to T_c, the total decay rate $\Gamma \ll t/\hbar$, the tunneling rate between adjacent s and p orbitals. However, the total decay rate becomes comparable to or larger than the tunneling rate for larger detuning Δ and $T \ll T_c$.

In the future, we would like to address two other aspects of dynamics of atoms in this lattice geometry. The first aspect is the thermalization time scale for atoms in the excited bands after the lattice transformation. This should prove to be an interesting study, particularly comparing this to other time scales in the problem, and studying this for different lattice transformations. The other aspect of the lattice is that the first three excited bands intersect at the center of the first Brillouin zone,

with the second and fourth bands forming a Dirac cone. This point of intersection has topological significance. Extending the present study to atoms excited to still higher bands, particularly atoms excited to the 4^{th} band where they condense at the center of the first Brillouin zone will be quite interesting.

Chapter 5

Real-valued Wannier functions

5.1 Introduction

The BH models are an approximation to the full many-body Hamiltonian in the tight-binding (TB) limit, and are written in a single-particle basis of spatially localized wave functions, generally referred to as Wannier functions. The parameters of the BH model are obtained as integrals over these functions. Thus, the key to accurately model these systems is to first construct a set of properly localized orthonormal basis functions. For simple cubic lattices with inversion symmetry, the standard procedure is to construct Wannier functions as "simple" superpositions of the Bloch functions belonging to a *single* energy band [50, 51]. For more complex lattice geometries with either asymmetries or quasi-degenerate energy bands, this procedure, however, does not lead to basis functions localized at the potential minima within each unit cell.

A common approach to ensuring localized Wannier functions for atoms in optical lattices is to use non-orthogonal atomic orbitals, modeled as harmonic oscillator

wave functions near the potential minima [49, 52]. This underestimates the tunneling energies even for deep lattices where the harmonic approximation is expected to work better. A more general approach developed within the solid-state community is due to Marzari and Vanderbilt [53, 54], where maximally localized Wannier functions are constructed by minimizing its spread by a suitable gauge transformation of the composite Bloch functions. This scheme has been adapted for atoms in optical lattices [17, 55–58]. Wannier functions obtained using this method, however, are not guaranteed to be real-valued and in turn depend on the choice of gauge transformation. An alternate method for constructing Wannier functions is by minimization of density-induced tunneling and density-density interactions between neighboring unit cells [59].

In this chapter, I propose an alternative numerical scheme for constructing real-valued Wannier functions. Following Kivelson [60] who showed that for an inversion symmetric lattice, Wannier functions are eigenstates of the position operator, we construct Wannier functions by diagonalization of the position operator expressed in the eigenstates of the single-particle Hamiltonian. The localized functions are remarkably accurate even for lattices with a large asymmetry. To ensure that the Wannier functions are strictly real-valued, we obtain the band structure and corresponding real-valued eigenfunctions using a uniform Fourier-grid discrete variable representation (DVR) [65]. General background on the DVR method can be found in [140–143], and some of their uses in ultracold atomic systems can be found in [144, 145]. Generalized Wannier functions localized at the potential minima in a unit cell are similarly constructed using a superposition of Bloch functions of

multiple bands.

The remainder of the chapter is setup as follows. In Sec. 5.2, we introduce the asymmetric double-well optical lattice potential, for which we describe the numerical procedure to obtain real-valued approximate Wannier functions. The method can be used for general lattices. For clarity, we focus on a particular lattice potential. In Sec. 5.3, we discuss how the single-particle band structure for this lattice can be obtained using a DVR, and also how it compares with that of a plane-wave basis calculation. We also describe how to extend our approach to general lattices. In Sec. 5.4 real-valued approximate Wannier and localized functions within a double-well potential are obtained using the eigenvectors from the DVR calculations. In Sec. 5.5, we discuss the accuracy of these numerically obtained Wannier functions by comparing the tunneling energies obtained using these functions to those obtained using a Fourier transform of the band dispersion. We use these Wannier functions in Sec. 5.6 to compute the two-body interaction energies for various asymmetries. We conclude in Sec. 5.7.

5.2 Optical lattice potential

We consider optical lattice potentials that have a double-well structure along the x axis, and a single-well structure along the perpendicular y and z axes. Such a lattice can be constructed using a laser with wave vector k_L and its first harmonic. The potential is given by

$$V(\vec{x}) = -V_0 \cos^2(k_L x) - V_1 \cos^2\left[2k_L(x+b)\right] - V_2\left[\cos^2(2k_L y) + \cos^2(2k_L z)\right], \quad (5.1)$$

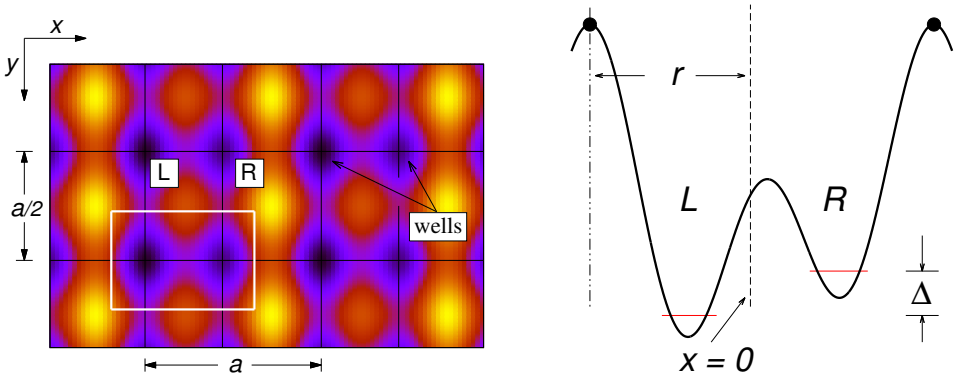

(a) (b)

Figure 5.1: (a) Contour plot of the optical lattice potential in the xy plane, where the potential minima are in dark blue. The white box encloses a unit cell of length a and $a/2$ along x and y, respectively. Each unit cell has a double well along the x axis, labeled L and R, and a single well along the y and z axes. (b) An asymmetric double-well potential (black curve) as a function of x for $V_1/V_0 = 1.3$ and $k_L b = 0.21\pi$. The horizontal red curves in the L and R wells represent the lowest two single-particle energy levels. The energy gap between these levels is Δ. The separation between the black dots is the lattice period a. The origin $x = 0$ of our coordinate system is indicated by the dashed line. For a symmetric lattice, the origin lies on the top of the barrier between the L and R wells. The distance between the origin and the left black dot is r.

where $V_{0,1,2} > 0$ are lattice depths. The lattice has periodicity $a = \pi/k_L$ along the x axis and $a/2$ along the perpendicular directions. The displacement b determines whether the lattice has an inversion-symmetric or asymmetric double-well. It is inversion symmetric for $k_L b = \pi/4$ and asymmetric otherwise. Throughout, we express energies in units of the recoil energy $E_R = \hbar^2 k_L^2/(2m_a)$, where m_a is the atomic mass. Figure 5.1a shows a contour plot of the optical-lattice potential in the xy plane for $k_L b = 0.21\pi$, while Fig. 5.1b shows the corresponding asymmetric double-well along the x axis. We will concentrate on the potential along the x axis in subsequent sections. The perpendicular directions will be needed when estimating two-body interaction energies in Sec. 5.6.

5.3 Band structure using a discrete variable representation

The single-particle band structure of a periodic potential is generally numerically determined in a plane-wave (PW) basis. For asymmetric lattices, the eigenvectors or the Bloch functions in this basis are complex valued and the corresponding Wannier functions are complex as well. We use a discrete variable representation (DVR) to obtain real-valued eigenfunctions.

We begin the procedure by discussing the one-dimensional DVR along the x axis. We are interested in solutions that have periodic boundary condition over M_x unit cells. For our double-well potential, it is convenient to apply the shift $x \to x - r$ such that the origin of the x axis coincides with the top of the potential barrier (see Fig. 5.1b), and consider the interval $(0, M_x a)$. For a symmetric double-well $r = a/2$,

while in general, it depends on the symmetry parameter b. We now introduce the uniformly spaced Fourier grid [65], based on $2N_x + 1$ periodic orthonormal basis functions $\phi_n(x) = \exp[i2\pi nx/(M_x a)]/\sqrt{M_x a}$ for $n = 0, \pm 1, \ldots, \pm N_x$. Orthonormal DVR basis functions are $f_i(x) = \langle x|x_i\rangle = \sqrt{\Delta x}\sum_{n=-N_x}^{N_x} \phi_n^*(x_i)\phi_n(x)$, labeled by grid points $x_i = i\Delta x$ with $i = 1, \ldots, 2N_x + 1$ and $\Delta x = M_x a/(2N_x + 1)$. A function $\langle x|x_i\rangle$ is localized around x_i and can be simplified with some trigonometry.

In this representation, the kinetic energy operator is $T_{ii'} = \langle x_i|T|x_{i'}\rangle$ where

$$T_{ii'} = (-1)^{i'-i} E_R \left(\frac{2\pi}{M_x k_L a}\right)^2 \begin{cases} N_x(N_x+1)/3, & i = i', \\ \dfrac{\cos\left[\pi(i'-i)/(2N_x+1)\right]}{2\sin^2\left[\pi(i'-i)/(2N_x+1)\right]}, & i \neq i', \end{cases} \tag{5.2}$$

and to a good approximation the potential energy operator is $\langle x_i|V|x_{i'}\rangle = V(x_i)\delta_{ii'}$ with Kronecker-delta δ_{ij}. In fact, it is this approximation that will limit our numerical accuracy using the DVR. On the other hand, the single-particle Hamiltonian $H_0 = T + V$ is a real symmetric matrix for both symmetric and asymmetric lattice potentials and its eigenfunctions can always be obtained using real arithmetic. We note that in a PW basis, the Hamiltonian for an asymmetric lattice is a complex Hermitian matrix. Typically, we require that $2N_x + 1 \gg M_x$ leading to many grid points per unit cell.

The eigenfunctions $|\lambda\rangle$ with dispersion ϵ_λ of H_0 with $\lambda \in \{1, \ldots, 2N_x + 1\}$ can be grouped into N_{band} bands containing M_x discrete quasi-momenta. This implies that both N_{band} and M_x must be odd as $M_x N_{\text{band}} = 2N_x + 1$. The lowest M_x eigenenergies correspond to the 1^{st} band, the next set corresponds to the 2^{nd} band, and so on. It can be separately shown from the $\phi_n(x)$ that allowed quasi-momenta

are

$$k_x = \frac{2p}{M_x}\frac{\pi}{a}, \quad p = 0, \pm 1, \pm 2, \ldots, \pm\frac{1}{2}\left(M_x - 1\right), \tag{5.3}$$

such that $-\pi/a \leq k_x \leq \pi/a$ and k_x stays within the 1$^{\text{st}}$ Brillouin zone. It is noteworthy that N_{band} also corresponds to the number of grid points within each unit cell. For real potentials $V(x)$, the eigenenergies for $\pm k_x$ are degenerate. Consequently, the single eigenstate with zero quasi-momentum can be easily located from the dispersion ϵ_λ. For other quasi-momenta, we can locate the pair of real eigenfunctions with degenerate ϵ_λ and compute the 2×2 matrix of the momentum operator. The eigenvalues of the momentum operator gives the quasi momentum k_x, thus leading to the assignment of the band dispersion $\epsilon_\lambda \to \epsilon_\alpha(k_x)$ with band index α. (Diagonal elements of the momentum operator are strictly zero, as the eigenfunctions of H_0 are real and periodic on interval $[0, M_x a]$)

Figure 5.2(a) shows numerical results for the double-well band dispersion at $k_x = 0$ for the lowest two bands using the PW basis. We find that energy differences become "noisy" beyond $N_{\text{PW}} > 25$ basis vectors and convergence is reached with uncertainties of $2 \times 10^{-12} E_R$ independent of the lattice asymmetry and band. This uncertainty should be compared with the band gap, $\approx \Delta$, between the two bands, which is on the order of E_R for typical lattice depths, and is close to the numerical accuracy to be expected using double-precision arithmetic. Figure 5.2(b) shows similar data, but now obtained for the DVR calculations as a function of N_{band} and $M_x = 3$. The integers N_{band} and N_{PW} can be directly compared as they both correspond to the number of energy bands obtained within the corresponding

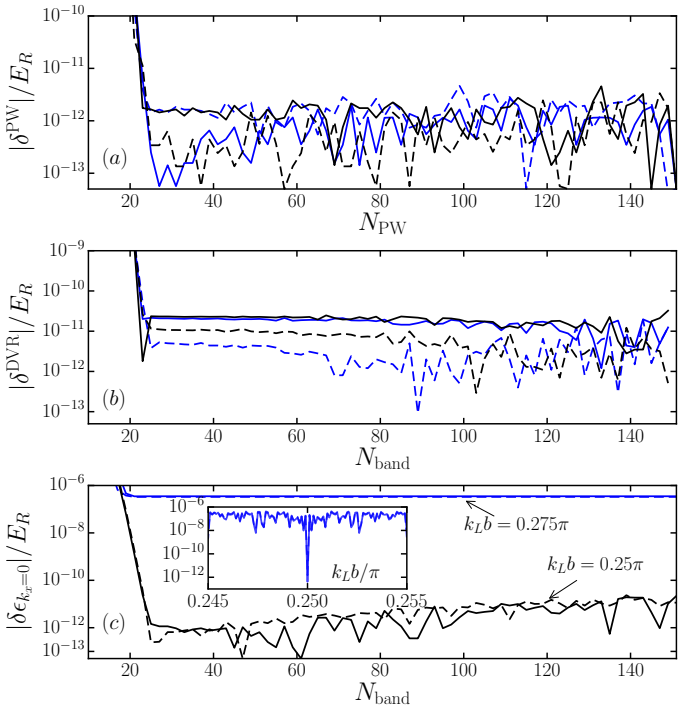

Figure 5.2: Panel (a) Convergence of the energy dispersion $\epsilon_\alpha(k_x)$ at quasi-momentum $k_x = 0$ computed with a PW basis as a function of $N_{\rm PW}$, the number of plane-waves. We plot the difference $\delta^{\rm PW}(N_{\rm PW}) = \epsilon_\alpha(k_x = 0; N_{\rm PW}) - \epsilon_\alpha(k_x = 0; N_{\rm PW}^{\rm max})$, where $N_{\rm PW}^{\rm max} = 151$. Panel (b) Similar plot using a DVR basis as a function of $N_{\rm band}$, the number of grid points in a unit cell. Plotted is $\delta^{\rm DVR}(N_{\rm band}) = \epsilon_\alpha(k_x = 0; N_{\rm band}) - \epsilon_\alpha(k_x = 0; N_{\rm band}^{\rm max})$, where $N_{\rm band}^{\rm max} = 151$ and $M_x = 3$. Panel (c) shows a comparison of $\epsilon_\alpha(k_x)$ at $k_x = 0$ obtained using the DVR and PW basis. We plot $\delta(N_{\rm band}) = \epsilon_\alpha(k_x = 0; {\rm DVR}) - \epsilon_\alpha(k_x = 0; {\rm PW})$ as a function of $N_{\rm band}$. The PW results are obtained with 151 basis vectors. Black and blue curves are for a symmetric lattice ($k_Lb = \pi/4$) and asymmetric lattice ($k_Lb = 0.275\pi$), respectively. Solid and dashed lines correspond to bands $\alpha = 1$ and 2, respectively and lattice depths are $V_0 = 35E_R$ and $V_1/V_0 = 1.3$, where E_R is the recoil energy. The inset in panel (c) compares the DVR and PW results as a function of lattice asymmetry k_Lb for fixed $N_{\rm band} = N_{\rm PW} = 51$.

calculation. We find that convergence is reached for $N_{\text{band}} > 25$ with uncertainties of $2\times10^{-11}E_R$ independent of the lattice asymmetry and band. For PW calculations with $N_{PW} > 25$ and DVR calculations with $N_{\text{band}} > 25$, the largest uncertainty is independent of quasi-momentum.

Figure 5.2(c) compares the $k_x = 0$ band dispersion computed with the DVR and PW basis, respectively. It shows that for symmetric lattices, the DVR and PW results agree to within the uncertainty of the DVR calculation. For asymmetric lattices, however, they converge to different values. The inset further highlights the difference between symmetric and asymmetric lattices by studying the difference of the band dispersion as a function of lattice asymmetry $k_L b$. We find that the value of $\epsilon_\alpha(k_x = 0)$ for the DVR is always larger than the PW result and the difference is symmetric around $k_L b = \pi/4$. The two results only agree infinitesimally close to $k_L b = \pi/4$. Furthermore, we find that the discrepancy is the same independent of quasi-momentum. As we will show in Sec. 5.5, this constant offset, nevertheless, leads to tunneling energies that are more accurate than might naively be expected.

Although we have focused on DVR-based band structure calculations for a one dimensional lattice, the method can be extended to higher dimensional non-separable lattices, such as graphene. The simplest approach is based on the realization that it is always possible to construct a non-primitive unit cell with orthogonal unit vectors such that the higher-dimensional kinetic-energy operator is separable along the unit vector directions and Eq. (5.2) can be directly used. Alternatively, we construct DVR basis functions from plane-waves that are periodic over a multiple of the primitive lattice vectors. In this case, the kinetic energy is not separable, but

can still be expressed in terms of trigonometric functions. We, however, note that for a d-dimensional lattice the matrix size of the single-particle Hamiltonian in the DVR method will be M^d times the size of the corresponding PW matrix, where M is the number of discrete quasi-momentum points along an axis. This implies that the determination of the eigenpairs with the DVR method is computationally more intensive, but is guaranteed to lead to real-valued eigenvectors.

5.4 Approximate Wannier functions

In this section we numerically construct approximate but real-valued Wannier functions localized within unit cells and generalized Wannier functions localized near the potential minina in each double well from superpositions of our real-valued DVR eigenfunctions. Here, we describe a method for constructing these Wannier functions based on Refs. [8, 60].

Kivelson [60] showed that for symmetric lattices with inversion symmetry, real-valued Wannier functions for band α are eigenstates of the projected position operator $\hat{x}_\alpha = \mathcal{P}_\alpha \, \hat{x} \, \mathcal{P}_\alpha$, where $\mathcal{P}_\alpha$ is the projection operator on the eigenstates of band α. The spacing between neighboring eigenvalues of this projected operator is a lattice constant.

We extend this approach for constructing real-valued Wannier functions to both symmetric and asymmetric lattices, even though there is no formal proof that for asymmetric lattices eigenfunctions of the position operator are Wannier functions. We term our functions "approximate" Wannier functions. Following the

previous section, the DVR eigenfunctions $|\lambda\rangle$ can be grouped into bands α. In fact, we have $|\lambda\rangle = |m, \alpha\rangle$, with $m \in \{1, \ldots, M_x\}$ and projector $\mathcal{P}_\alpha = \sum_m |m, \alpha\rangle\langle m, \alpha|$. We construct the matrix $\langle m, \alpha|\hat{x}|m', \alpha\rangle$ over all m and m' in the same band α using that $\langle x_i|\hat{x}|x_{i'}\rangle = x_i\delta_{ii'}$ to good approximation. Diagonalization leads to real approximate Wannier functions $w_{j,\alpha}(x)$ for unit cell $j = \{1, \ldots, M_x\}$ and as we will show in Sec. 5.5, they reproduce the tunneling energies with great accuracy.

Generalized Wannier functions $v_{j,\eta}(x)$ localized in the $\eta = L$ and R wells of Fig. 5.1b can be constructed by creating superpositions of DVR functions from multiple bands. In our case, we restrict the bands to $\alpha \in \{1, 2\}$ and compute the eigenfunctions of the projected position operator $\mathcal{P}\hat{x}\mathcal{P}$, where $\mathcal{P} = \sum_{m,\alpha=1,2} |m, \alpha\rangle\langle m, \alpha|$. This approach is used for both symmetric and asymmetric lattices.

Figures 5.3 (a) and (d) show numerical Wannier functions $w_{j,\alpha}(x)$ for a symmetric lattice with band index $\alpha \in \{1, 2\}$ on a linear and logarithmic scale, respectively. The Wannier function is localized in the unit cell at the center of the lattice with $j = j_c \equiv (M_x + 1)\text{div}2$ and $x_c = M_x a/2$. For the symmetric lattice, both $w_{j_c,1}(x)$ and $w_{j_c,2}(x)$ are, however, spread over the two wells in the unit cell. Figures 5.3 (b) and (e) show similar plots for an asymmetric lattice, while Figs. 5.3 (c) and (f) show generalized Wannier functions $v_{j_c,\eta}(x)$ with $\eta \in \{L, R\}$ based on the first two bands for the same lattice parameters. Owing to a large asymmetry for these last four panels, the band gap between the two lowest bands is large. We thus expect $w_{j_c,1}(x) \approx w_{j_c,R}(x)$ and $w_{j_c,2}(x) \approx w_{j_c,L}(x)$ as indeed observed when comparing Figs. 5.3 (b) and (c). It is, however, interesting to note that the $v_{j_c,\eta}(x)$'s and $w_{j_c,\alpha}(x)$'s are not exactly the same. In fact, $v_{j_c,\eta}(x)$ is more localized within the

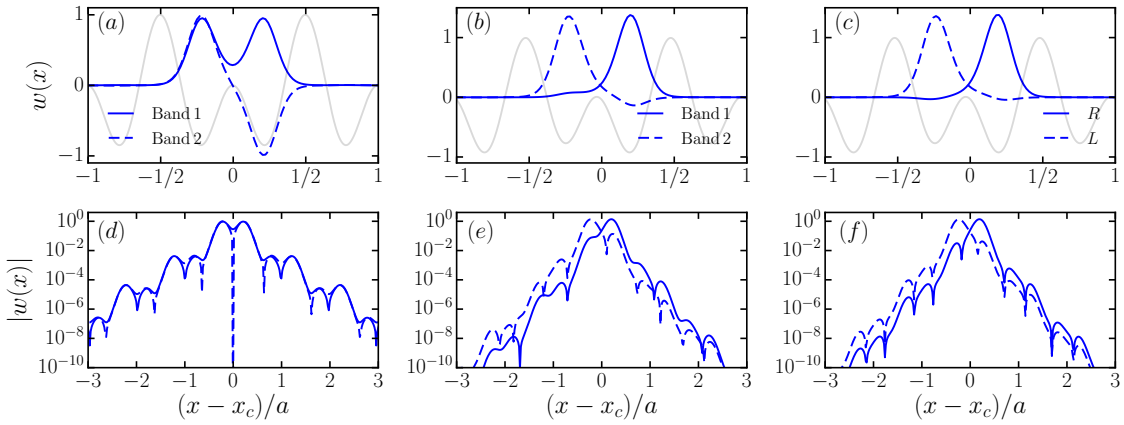

Figure 5.3: Plots of normalized Wannier functions $w_{j_c,\alpha}(x)$ and generalized Wannier functions $v_{j_c,\eta}(x)$ in the center of the lattice as a function of x. Here, wave functions and position are in units of $1/\sqrt{M_x a}$ and lattice period a, respectively. Panels (a) and (d) show the $\alpha = 1, 2$ Wannier functions for a symmetric lattice on a linear and logarithmic scale, respectively. For clarity, we have shifted the x axis by x_c, such that the center of the interval is at the origin. Here, $M_x = 21$, $N_{\text{band}} = 53$, $k_L b = 0.25\pi$, $V_0/E_R = 35$ and $V_1/V_0 = 1.3$. The solid and dashed blue curves represent the 1^{st} and 2^{nd} band, respectively. The gray line represents the symmetric double-well potential. Panels (b) and (e) show similar plots, but now for an asymmetric lattice with $k_L b = 0.275\pi$ with other parameters unchanged. Panels (c) and (f) show the generalized Wannier functions at the L and R wells within a double-well for the same lattice as used in panels (b) and (e). The solid and dashed blue lines represent $v_{j_c,R}(x)$ and $v_{j_c,L}(x)$, respectively.

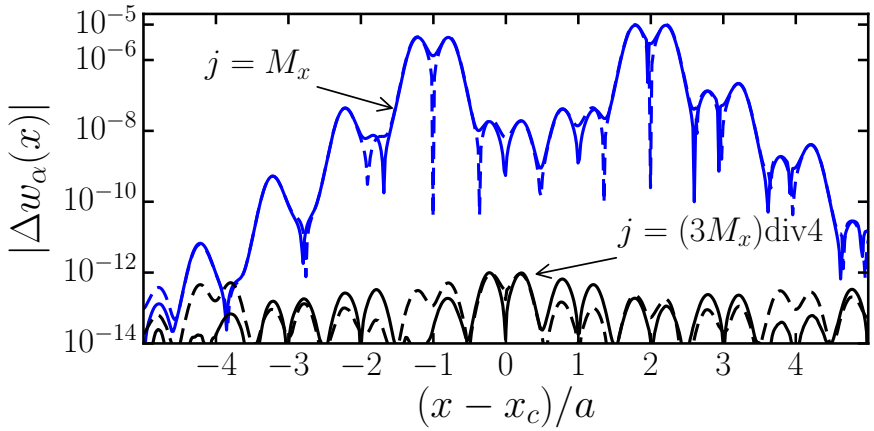

Figure 5.4: Graphs of difference between (shifted) Wannier functions $w_{j,\alpha}(x)$ and that at the center of the lattice. Plotted are $\Delta w_\alpha(x) = |w_{j,\alpha}(x-[j-j_c]a)|-|w_{j_c,\alpha}(x)|$ for unit cells $j = (3M_x)\text{div}4$ (black curves) and M_x (blue curves) as a function of x in units of lattice period a. The argument $x - [j - j_c]a$ is computed assuming modular arithmetic on interval $M_x a$. Solid and dashed lines correspond to bands $\alpha = 1$ and 2, respectively. The plot is for a symmetric lattice with $k_L b = 0.25\pi$, $V_0 = 35E_R$, $V_1/V_0 = 1.3$, $M_x = 21$ and $N_{\text{band}} = 53$.

L and R wells compared to $w_{j_c,\alpha}(x)$. For even larger asymmetries, this difference in localization persists and the "tail" of $w_{j_c,\alpha}(x)$ does not approach $v_{j_c,\eta}(x)$, leading to marked differences in the calculated BH parameters, as will be shown in Sec. 5.6.

Figure 5.4 shows a comparison of Wannier functions for a symmetric lattice computed at different unit cells. We find that the difference between the Wannier functions at the edge and the center is of the order of $10^{-5}/\sqrt{M_x a}$ for all x. For all other unit cells, the difference from the central Wannier function is of the order of $10^{-13}/\sqrt{M_x a}$, which is close to our numerical accuracy. One of such a difference

with $j = (3M_x)\text{div}4$ is shown in the figure. Hence, the shape of our approximate Wannier functions are mostly independent of unit cell. This observation remains true for asymmetric lattices.

5.5 Tunneling energies based on Wannier functions

In Sec. 5.4 we showed that approximate Wannier functions and generalized Wannier functions within a double-well can be constructed from DVR eigenvectors. In this section we use these functions to compute tunneling energies and discuss their accuracy. In particular, the accuracy of the single band Wannier functions are ascertained in Sec. 5.5.1 by comparing band tunneling energies as they only depend on the band dispersion and should be independent of the choice of Wannier functions. Tunneling energies between neighboring L and R wells are computed in Sec. 5.5.2 and a corresponding tight-binding (TB) model is shown to have significant contributions from tunneling energy terms between next-nearest neighbors and beyond.

5.5 Band tunneling energies

Tunneling energies are defined by the matrix elements $J_\alpha = \langle w_{j,\alpha}|H_0|w_{j',\alpha}\rangle$ over the Wannier functions of band α localized in unit cells j and j'. Here, H_0 is the single-particle Hamiltonian. We mainly focus on nearest-neighbor tunneling with $j' = j \pm 1$. Formally, the J_α should only depend on $|j - j'|$.

There are three different ways to obtain tunneling energies. The first is to use

our approximate Wannier functions for band α as computed in Sec. 5.4 and calculate the matrix element. We label them J_α^{W}. The other two methods rely on the usual definition of a Wannier function as a "Fourier transform" of Bloch functions of the corresponding band. With this definition, the tunneling energies only depend on $\epsilon_\alpha(k_x)$ and between nearest-neighbor unit cells ($|j - j'| = 1$) is given by

$$J_\alpha = \frac{a}{2\pi} \int_{-\pi/a}^{\pi/a} \cos(k_x a) \epsilon_\alpha(k_x) dk_x, \tag{5.4}$$

independent of j. The tunneling energy can now be determined either by substituting $\epsilon_\alpha(k_x)$ calculated using the PW basis or by using that obtained from the DVR method. We refer to these tunneling energies by J_α^{PW} and J_α^{DVR}, respectively.

Figure 5.5 shows a comparison between tunneling energies J_α^{PW}, J_α^{DVR} and J_α^{W} as a function of the number of unit cells. The energy J_α^{W} has been computed using approximate "DVR" Wannier function for the central unit cell. We find that for a symmetric lattice (panel (a)) convergence is reached for $M_x > 9$ unit cells, with uncertainties of $2 \times 10^{-13} E_R$ for all methods. This confirms the central idea of Ref. [60], that Wannier functions are eigenstates of the $\hat{x}_\alpha$ operator for symmetric lattices. Figure 5.5 (b) shows $J_\alpha^{\mathrm{DVR}} - J_\alpha^{\mathrm{PW}}$ and $J_\alpha^{\mathrm{W}} - J_\alpha^{\mathrm{PW}}$ converge to $2 \times 10^{-11} E_R$ for band 1 and $1 \times 10^{-10} E_R$ for band 2, much above the value reached for the symmetric lattice. Within the DVR calculation, however, J_α^{W} and J_α^{DVR} agree much better. The discrepancy between the PW and DVR results can be attributed to the difference in the band dispersion shown in Fig. 5.2. Nevertheless, even an uncertainty of $10^{-10} E_R$ is sufficient for all practical purposes.

We have numerically ascertained that J_α^{W} does not vary with the unit cell

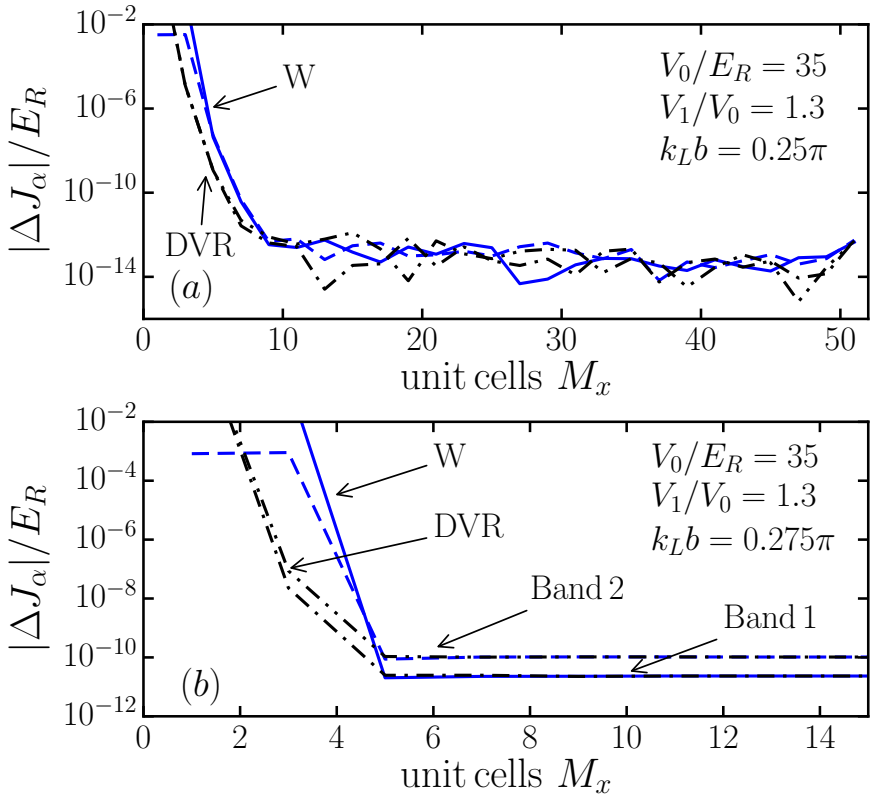

Figure 5.5: Comparison of the nearest neighbor tunneling energies $J_\alpha^{\rm PW}$, $J_\alpha^{\rm DVR}$ and $J_\alpha^{\rm W}$ for bands $\alpha = \{1, 2\}$, as computed using the Fourier transform of the band dispersion from the PW and DVR calculations, and the DVR band Wannier functions $w_\alpha(x)$, respectively. (a) Tunneling energy comparison for a symmetric lattice with $k_L b = 0.25\pi$. Plotted are $\Delta J_\alpha = J_\alpha^{\rm DVR} - J_\alpha^{\rm PW}$ (black curves labeled DVR) and $\Delta J_\alpha = J_\alpha^{\rm W} - J_\alpha^{\rm PW}$ (blue curves labeled W) in units of E_R as a function of the number of unit cells M_x. Solid and dashed lines correspond to bands $\alpha = 1$ and 2, respectively. We used $V_0 = 35E_R$, $V_1/V_0 = 1.3$ and $N_{\rm PW} = N_{\rm band} = 35$. (b) Similar plot for an asymmetric lattice with $k_L b = 0.275\pi$ with other parameters unchanged.

index j to better than $10^{-13}E_R$ apart from the two edge unit cells consistent with our observations on the shape of Wannier functions in Fig. 5.4. In fact, the difference between the tunneling energies at the central and edge unit cell is only $10^{-8}E_R$. Consequently, the value of J_α^{W} obtained from the central unit cell is better than that from the edge unit cells and agrees better with J_α^{PW}. In other words, a comparison with the tunneling energies J_α^{PW} gives a good estimate of the accuracy of our real-valued Wannier functions.

We have also determined the next-nearest neighbor tunneling energies. For typical lattice depths, its value is two orders of magnitude or more lower than that of nearest neighbors. Its uncertainty in units of E_R is the same as for nearest-neighbor tunneling energies. Hence, we conclude that the approximate DVR Wannier functions can be used to compute tunneling energies between distant neighbors.

5.5 Tight binding tunneling energies

It is often useful to write down a tight-binding Hamiltonian in terms of L and R wells defined in Fig. 5.1b and with hopping parameters computed from our generalized Wannier functions with the lowest on-site energies $\langle v_{j,\eta}|H_0|v_{j',\eta}\rangle$. Figure 5.6 defines tunneling energies between adjacent unit cells and the energy gap Δ between the on-site energies based on the lowest two bands of our H_0. The largest parameters are given by $t = \langle w_{j,L}|H_0|w_{j,R}\rangle$ and $J = \langle w_{j,R}|H_0|w_{j+1,L}\rangle$, where j is the unit cell index. Similar expressions can be written down for other parameters. The value of these tunneling energies depends on the definition of the generalized Wannier functions and cannot be extracted from a transformation of the band dispersion

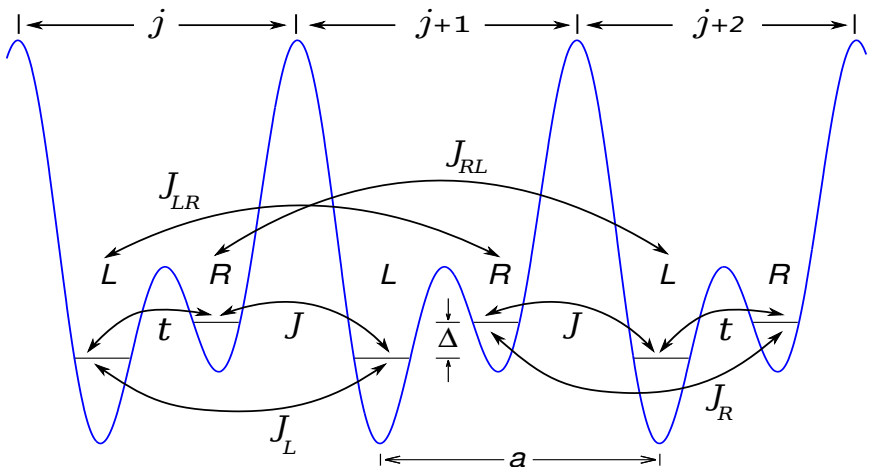

Figure 5.6: Tight-binding Hamiltonian based on the lowest two bands for an asymmetric double-well optical lattice. The figure shows various tunneling energies t, J, J_L, J_R, J_{LR} and J_{RL} between three neighboring unit cells. The energy gap between the two on-site energies is Δ and the lattice has period a.

energies. Finally, we note that all coefficients are real-valued.

Figure 5.7 shows the largest seven hopping parameters of our TB model as a function of lattice depth V_0 for an asymmetric lattice. As expected, the tunneling energies decrease with lattice depth, while simultaneously Δ increases. For fixed lattice depth the tunneling energies are smaller the further the atom has to hop.

The TB Hamiltonian for two modes within a unit cell can be diagonalized analytically by a transformation to quasi-momentum space. The eigenenergies are

$$\epsilon_\alpha^{\mathrm{TB}}(k_x) = -(J_R + J_L)\cos k_x a \mp \sqrt{\left[(J_R - J_L)\cos k_x a - \Delta/2\right]^2 + |f(k_x)|^2}, \qquad (5.5)$$

where $\mp$ correspond to bands $\alpha = 1$ and 2, respectively, and $f(k_x) = t + Je^{-ik_x a} + J_{LR}e^{ik_x a} + J_{RL}e^{-2ik_x a}$. The band tunneling energies J_α^{TB} can be obtained by substituting $\epsilon_\alpha^{\mathrm{TB}}(k_x)$ into Eq. (5.4) and performing the Fourier transform.

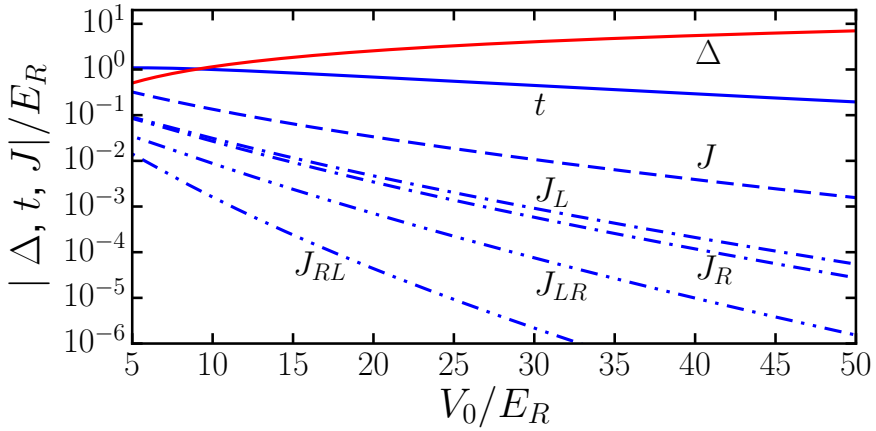

Figure 5.7: Log-linear plot of the absolute value of tunneling energies t, J, J_L, J_R, J_{LR}, J_{RL} and energy-gap Δ in units of E_R as a function of lattice depth V_0. The plot is for an asymmetric lattice with $k_L b = 0.275\pi$ and $V_1/V_0 = 1.3$.

We can now compare the band tunneling energies of our TB simulations with those of the exact band structure calculations using the PW basis. We find that the difference between the TB and PW result is within approximately 50% for both bands when we only include nearest-neighbor tunneling energies t and J and 5% when in addition next nearest-neighbor tunneling energies J_L and J_R are included, and this stays nearly the same upon including the next to next-nearest neighbor hopping terms J_{LR} and J_{RL}. These differences are almost independent of the lattice depth and consistent with results of Ref. [17] who based their calculations on complex-valued maximally-localized Wannier functions. The TB result can get better if we include more tunneling energies and allow atoms to hop even further.

5.6 Interaction energies

We have shown the excellent accuracy of the approximate Wannier functions in Sec. 5.5. In this section, we use these functions to study the two-body atom-atom interaction terms in the Hubbard model. So far, we have focused on the double-well lattice along the x axis. We can extend the calculations to the perpendicular directions and obtain the corresponding Wannier functions. Owing to the large band gap between the 1^{st} and 2^{nd} bands along perpendicular directions compared to that along the x direction, only the ground band is considered. Thus, the full three-dimensional band Wannier functions are $w_\alpha(\vec{x}) = w_{j_c,\alpha}(x)w(y)w(z)$, where band index $\alpha \in \{1, 2\}$ and $w(y)$, $w(z)$ are the ground-band Wannier functions at the center of the lattice along the perpendicular directions. We note that the y and z Wannier functions have the same functional form as for simplicity we have assumed the same lattice depth along the perpendicular directions. Similarly, the generalized Wannier functions are $v_\eta(\vec{x}) = v_{j_c,\eta}(x)w(y)w(z)$, where $\eta \in \{L, R\}$.

In the Hubbard model using a band basis, two-body on-site interaction energies are

$$U_{\alpha_1\alpha_2\alpha_3\alpha_4} = g \int w_{\alpha_1}(\vec{x})w_{\alpha_2}(\vec{x})w_{\alpha_3}(\vec{x})w_{\alpha_4}(\vec{x})d\vec{x}, \tag{5.6}$$

where $g = 4\pi\hbar^2 a_s/m_a$, a_s is the s-wave scattering length and we use that the $w(\vec{x})$ are real. There are five distinct coefficients: U_{1111}, U_{1112}, U_{1122}, U_{1222} and U_{2222}. On-site interaction energies $U_{\eta_1\eta_2\eta_3\eta_4}$ in the LR basis using the generalized Wannier functions $v_\eta(\vec{x})$ can be similarly defined. The five distinct interactions coefficients

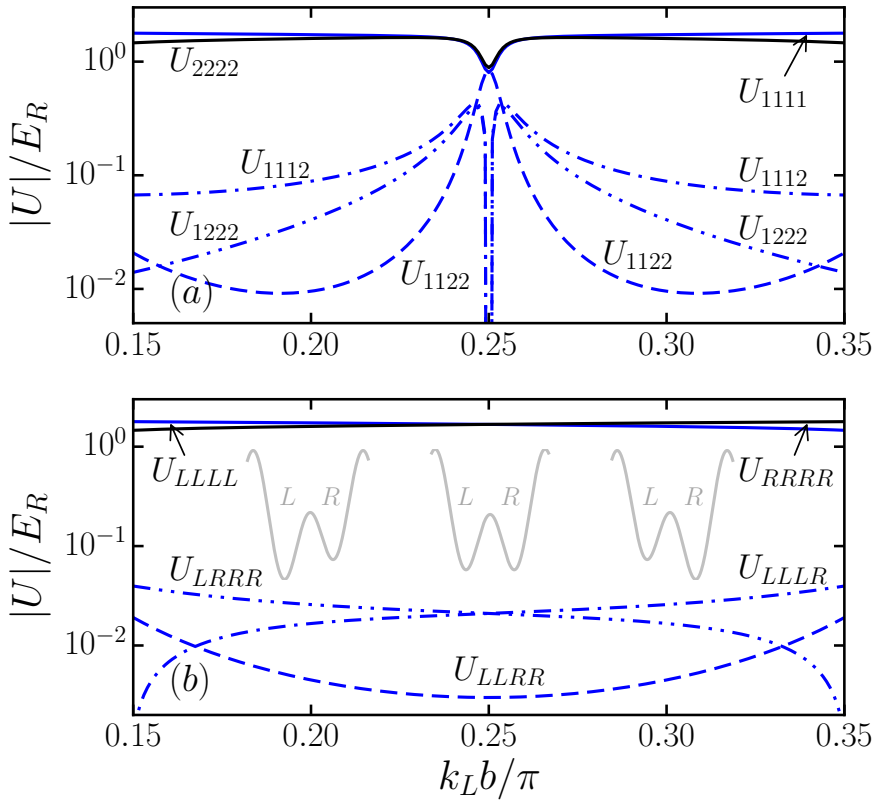

Figure 5.8: Two-body interaction energies in the Hubbard model for ^{87}Rb in units of E_R as a function of lattice asymmetry $k_L b/\pi$. We use $V_0/E_R = 35$, $V_1/V_0 = 1.3$, $V_2/E_R = 70$ and scattering length $a_s = 5.3$ nm. Panel (a) shows interaction energies $U_{\alpha_1\alpha_2\alpha_3\alpha_4}$ in the band basis with $\alpha \in \{1, 2\}$. Panel (b) shows interaction energies $U_{\eta_1\eta_2\eta_3\eta_4}$ in the LR basis with $\eta \in \{L, R\}$. From left to right the insets show a schematic of a double-well potential for lattice asymmetries $k_L b < 0.25\pi$, $k_L b = 0.25\pi$ and $k_L b > 0.25\pi$, respectively.

are U_{LLLL}, U_{LLLR}, U_{LLRR}, U_{LRRR} and U_{RRRR}.

Figures 5.8 (a) and (b) show the two-body interaction energies $U_{\alpha_1\alpha_2\alpha_3\alpha_4}$ and $U_{\eta_1\eta_2\eta_3\eta_4}$, respectively, for ^{87}Rb with $a_s = 5.3$ nm as a function of the lattice asymmetry b, with other lattice parameters kept fixed. Figure 5.8 (a) is symmetric around $k_L b = \pi/4$. At the symmetry point $k_L b = \pi/4$, $U_{1111} \lesssim U_{1122} \lesssim U_{2222}$, while U_{1112} and U_{1222} are strictly zero due to parity. As the lattice becomes asymmetric, U_{1111} and U_{2222} double their strength, U_{1122} rapidly decreases, while U_{1112} and U_{1222} have a maximum but remain relatively large.

Figure 5.8 (b) shows that $U_{\eta_1\eta_2\eta_3\eta_4}$ has a smoother dependence on asymmetry than $U_{\alpha_1\alpha_2\alpha_3\alpha_4}$. For all asymmetries, we observe that U_{LLLL} and U_{RRRR} are much larger than the other energies. Moreover, $U_{LLLL} = U_{RRRR}$ for a symmetric lattice, and $U_{RRRR} > U_{LLLL}$ for $k_L b > \pi/4$. This behavior is reversed for $k_L b < \pi/4$. This is a consequence of the fact that $v_R(\vec{x})$ is more confined than $v_L(\vec{x})$ for $k_L b > \pi/4$ and vice versa. Interestingly, the density-induced tunneling energies U_{LRRR} and U_{LLLR} are, in general, larger than the density-density term U_{LLRR}. The former coefficients lead to terms in a Hubbard model where an atom hops from one well to the other in a unit cell, while the latter coefficient leads to either a long-range density-density interaction or pair hopping. The relative size of these energies highlight the limits of Hubbard models that do or do not include specific two-body terms [15].

The two-body interaction energies within the two bases can be compared in several limits of the lattice asymmetry. For $k_L b > \pi/4$ and very large asymmetries where $U_{1122} \ll U_{1111}$ the Wannier functions $w_1(\vec{x})$ approach $v_R(\vec{x})$ (similarly, $w_2(\vec{x})$ approaches $v_L(\vec{x})$) and, thus, $U_{1111} \to U_{RRRR}$ and $U_{2222} \to U_{LLLL}$. In fact, for as

low as $k_L b = 0.26\pi$, $U_{1111} \approx 0.95\, U_{RRRR}$. On the other hand, for a symmetric lattice we can write $w_{1,2}(\vec{x}) \approx (v_L(\vec{x}) \pm v_R(\vec{x}))/\sqrt{2}$ and $U_{LLLL} = U_{RRRR}$, which leads to U_{1111}, U_{1122}, $U_{2222} \approx U_{LLLL}/2$. The additional realization that U_{LLLL} and U_{RRRR} are nearly insensitive to asymmetry also explains the doubling in value of U_{1111} and U_{2222} near $k_L b = \pi/4$.

Even though the Wannier functions $w_1(\vec{x})$ and $v_R(\vec{x})$ approach each other for large asymmetries and $k_L b > \pi/4$, the function $v_R(x)$ is always more confined than $w_1(x)$. Consequently, cross-terms U_{1122}, U_{1112} and U_{1222}, which depend on the tail of the Wannier functions, are always larger than the corresponding cross-terms U_{LLRR}, U_{LLLR} and U_{LRRR}.

5.7 Conclusion

We have shown that real-valued Wannier functions can be efficiently constructed for both symmetric and asymmetric periodic potentials or optical lattices. The first step involves obtaining the single-particle band structure and real-valued eigenvectors using a Discrete Variable Representation (DVR). A Fourier grid DVR based on basis functions with periodic boundary conditions is shown to have excellent numerical accuracy compared to a direct calculation based on plane-waves. In the next step, restricted to eigenvectors within the subspace of band α, Wannier functions $w_\alpha(x)$ localized within a unit cell are obtained as eigenstates of the position operator. By using eigenvectors corresponding to the lowest two bands, generalized Wannier functions $w_\eta(x)$ localized to L and R wells within a double-well can also

be constructed. By a comparison of the tunneling energies, the Wannier functions are shown to reproduce the Hubbard parameters with excellent accuracy. Tunneling energies are subsequently obtained between the L and R wells using the generalized Wannier functions, and limits of a tight-binding containing only nearest-neighbor tunneling energies are discussed. Finally, we use these functions to study the two-body interaction energies in the BH model and discuss the relative importance of the various interaction energy terms. The numerical methods developed are general and can be applied to a wide array of optical lattice geometries in one, two or three dimensions.

Chapter 6

Conclusions

The behavior of ultracold atoms in optical lattices can be described by the quantum many-body Bose-Hubbard (BH) Hamiltonian and the characteristics of the single-band BH Hamiltonian have been studied in great detail. Experiments with ultracold atoms in optical lattices, due to their high degree of tunability, have become the testing ground of diverse quantum many-body Hamiltonians. As such, the paradigm has shifted towards studying "extensions" to the standard BH model.

In this thesis, I have presented my results on the multi-band BH model in a double-well optical lattice. I have shown that the phase diagram for such a system is markedly different from that of the "standard" single-band BH model and the Mott lobes do not monotonically decrease in size with increase of atom number. Subsequently, I derived an effective single-band Hamiltonian to describe this system, and showed that such a Hamiltonian has strong on-site three-body interactions. In addition I described how by tuning the lattice parameters, the effective two-body interaction can be tuned to zero. The experimental parameters used are accessible to present day cold atom experiments.

I have also proposed yet another method to create an ultra-cold gas of bosonic atoms in an optical lattice where atoms only interact via on-site three-body interactions. This is achieved by a careful cancellation of two contributions in the pair-wise interaction between two atoms, one proportional to the zero-energy scattering length and a second proportional to the effective range. We predict that this cancellation can occur for the strontium-88 isotope as well as near narrow magnetic Feshbach resonances in alkali-metal atom or chromium collisions.

There have been several proposals of "unconventional" Bose-Einstein condensates in optical lattices and predictions of rich orbital physics in higher bands. In this thesis, I have presented our largely analytical results on the lifetime of a condensate formed in the second band of a double-well 2D optical lattice with weak harmonic confinement in the perpendicular z direction. I have shown that the decay rate depends on lattice asymmetry and temperature. In certain experimentally accessible parameter regimes, the decay rate is actually smaller than the tunneling rate between adjacent wells, thus allowing for the possibility of observing such a condensation. There have indeed been experimental realizations of Bose-Einstein condensates in excited bands of an optical lattice.

The parameters of the BH models are obtained as integrals over spatially localized single-particle basis functions, often referred to as Wannier functions. The standard methods for obtaining these functions generally produce complex-valued wave functions. In this thesis, I have proposed a numerical method using discrete variable representation for constructing real-valued approximate Wannier functions localized in a unit cell for both symmetric and asymmetric periodic potentials. I sub-

sequently showed by a comparison of tunneling energies that the obtained Wannier functions have very high accuracy.

The theoretical results derived for observing three-body interactions in an optical lattice can have possible experimental realizations. The numerical methods developed for constructing Wannier functions are general and can be put to use for more complex lattice geometries in one, two or three dimensions. This thesis uncovers some interesting and emergent aspects among a bevy of rich quantum phenomena associated with the BH models. Surely, the BH models are going to get more exotic in the coming days and years!

Bibliography

[1] I. Bloch, J. Dalibard, and W. Zwerger, "Many-body physics with ultracold gases," *Reviews of Modern Physics*, vol. 80, pp. 885–964, July 2008.

[2] J. Sebby-Strabley, M. Anderlini, P. S. Jessen, and J. V. Porto, "Lattice of double wells for manipulating pairs of cold atoms," *Physical Review A*, vol. 73, p. 033605, Mar. 2006.

[3] P. J. Lee, M. Anderlini, B. L. Brown, J. Sebby-Strabley, W. D. Phillips, and J. V. Porto, "Sublattice Addressing and Spin-Dependent Motion of Atoms in a Double-Well Lattice," *Physical Review Letters*, vol. 99, p. 020402, July 2007.

[4] S. Trotzky, P. Cheinet, S. Flling, M. Feld, U. Schnorrberger, A. M. Rey, A. Polkovnikov, E. A. Demler, M. D. Lukin, and I. Bloch, "Time-Resolved Observation and Control of Superexchange Interactions with Ultracold Atoms in Optical Lattices," *Science*, vol. 319, pp. 295–299, Jan. 2008.

[5] M. Atala, M. Aidelsburger, J. T. Barreiro, D. Abanin, T. Kitagawa, E. Demler, and I. Bloch, "Direct measurement of the Zak phase in topological Bloch bands," *Nature Physics*, vol. 9, pp. 795–800, Dec. 2013.

[6] L. Tarruell, D. Greif, T. Uehlinger, G. Jotzu, and T. Esslinger, "Creating, moving and merging Dirac points with a Fermi gas in a tunable honeycomb lattice," *Nature*, vol. 483, pp. 302–305, Mar. 2012.

[7] G.-B. Jo, J. Guzman, C. K. Thomas, P. Hosur, A. Vishwanath, and D. M. Stamper-Kurn, "Ultracold Atoms in a Tunable Optical Kagome Lattice," *Physical Review Letters*, vol. 108, p. 045305, Jan. 2012.

[8] T. Uehlinger, G. Jotzu, M. Messer, D. Greif, W. Hofstetter, U. Bissbort, and T. Esslinger, "Artificial Graphene with Tunable Interactions," *Physical Review Letters*, vol. 111, p. 185307, Oct. 2013.

[9] S. Paul and E. Tiesinga, "Large effective three-body interaction in a double-well optica l lattice," *Physical Review A*, vol. 92, p. 023602, Aug. 2015.

[10] D.-S. Lühmann, O. Jürgensen, and K. Sengstock, "Multi-orbital and density-induced tunneling of bosons in optical lattices," *New Journal of Physics*, vol. 14, p. 033021, Mar. 2012.

[11] D. Jaksch and P. Zoller, "The cold atom Hubbard toolbox," *Annals of Physics*, vol. 315, pp. 52–79, Jan. 2005.

[12] D. Jaksch, C. Bruder, J. I. Cirac, C. W. Gardiner, and P. Zoller, "Cold bosonic atoms in optical lattices," *Physical Review Letters*, vol. 81, no. 15, pp. 3108–3111, 1998.

[13] D. van Oosten, P. van der Straten, and H. T. C. Stoof, "Quantum phases in an optical lattice," *Physical Review A*, vol. 63, p. 053601, Apr. 2001.

[14] M. Greiner, O. Mandel, T. Esslinger, T. W. Hänsch, and I. Bloch, "Quantum phase transition from a superfluid to a Mott insulator in a gas of ultracold atoms," *Nature*, vol. 415, pp. 39–44, Jan. 2002.

[15] O. Jürgensen, K. Sengstock, and D.-S. Lühmann, "Density-induced processes in quantum gas mixtures in optical lattices," *Physical Review A*, vol. 86, p. 043623, Oct. 2012.

[16] I. Danshita, J. E. Williams, C. A. R. Sá de Melo, and C. W. Clark, "Quantum phases of bosons in double-well optical lattices," *Physical Review A*, vol. 76, p. 043606, Oct. 2007.

[17] M. Modugno and G. Pettini, "Maximally localized Wannier functions for ultracold atoms in one-dimensional double-well periodic potentials," *New Journal of Physics*, vol. 14, p. 055004, May 2012.

[18] A. J. Daley, J. M. Taylor, S. Diehl, M. Baranov, and P. Zoller, "Atomic Three-Body Loss as a Dynamical Three-Body Interaction," *Physical Review Letters*, vol. 102, p. 040402, Jan. 2009.

[19] T. Sowiński, "Exact diagonalization of the one-dimensional Bose-Hubbard model with local three-body interactions," *Physical Review A*, vol. 85, p. 065601, June 2012.

[20] A. Safavi-Naini, J. von Stecher, B. Capogrosso-Sansone, and S. T. Rittenhouse, "First-Order Phase Transitions in Optical Lattices with Tunable Three-Body Onsite Interaction," *Physical Review Letters*, vol. 109, p. 135302, Sept. 2012.

[21] M. Greiter, X.-G. Wen, and F. Wilczek, "Paired Hall state at half filling," *Physical Review Letters*, vol. 66, pp. 3205–3208, June 1991.

[22] A. Wójs, C. Töke, and J. K. Jain, "Global Phase Diagram of the Fractional Quantum Hall Effect Arising from Repulsive Three-Body Interactions," *Physical Review Letters*, vol. 105, p. 196801, Nov. 2010.

[23] B. Paredes, T. Keilmann, and J. I. Cirac, "Pfaffian-like ground state for three-body hard-core bosons in one-dimensional lattices," *Physical Review A*, vol. 75, p. 053611, May 2007.

[24] M. Roncaglia, M. Rizzi, and J. I. Cirac, "Pfaffian State Generation by Strong Three-Body Dissipation," *Physical Review Letters*, vol. 104, p. 096803, Mar. 2010.

[25] A. Kitaev, "Fault-tolerant quantum computation by anyons," *Annals of Physics*, vol. 303, no. 1, pp. 2 – 30, 2003.

[26] P. R. Johnson, E. Tiesinga, J. V. Porto, and C. J. Williams, "Effective three-body interactions of neutral bosons in optical lattices," *New Journal of Physics*, vol. 11, p. 093022, Sept. 2009.

[27] E. Tiesinga and P. R. Johnson, "Collapse and revival dynamics of number-squeezed superfluids of ultracold atoms in optical lattices," *Physical Review A*, vol. 83, p. 063609, June 2011.

[28] U. Bissbort, F. Deuretzbacher, and W. Hofstetter, "Effective multibody-induced tunneling and interactions in the Bose-Hubbard model of the lowest dressed band of an optical lattice," *Physical Review A*, vol. 86, p. 023617, Aug. 2012.

[29] K. W. Mahmud and E. Tiesinga, "Dynamics of spin-1 bosons in an optical lattice: Spin mixing, quantum-phase-revival spectroscopy, and effective three-body interactions," *Physical Review A*, vol. 88, p. 023602, Aug. 2013.

[30] G. K. Campbell, J. Mun, M. Boyd, P. Medley, A. E. Leanhardt, L. G. Marcassa, D. E. Pritchard, and W. Ketterle, "Imaging the Mott Insulator Shells by Using Atomic Clock Shifts," *Science*, vol. 313, pp. 649–652, Aug. 2006.

[31] S. Will, T. Best, U. Schneider, L. Hackermüller, D.-S. Lühmann, and I. Bloch, "Time-resolved observation of coherent multi-body interactions in quantum phase revivals," *Nature*, vol. 465, pp. 197–201, May 2010.

[32] M. J. Mark, E. Haller, K. Lauber, J. G. Danzl, A. J. Daley, and H.-C. Nägerl, "Precision Measurements on a Tunable Mott Insulator of Ultracold Atoms," *Physical Review Letters*, vol. 107, p. 175301, Oct. 2011.

[33] M. J. Mark, E. Haller, K. Lauber, J. G. Danzl, A. Janisch, H. P. Bchler, A. J. Daley, and H.-C. Nägerl, "Preparation and Spectroscopy of a Metastable Mott-Insulator State with Attractive Interactions," *Physical Review Letters*, vol. 108, p. 215302, May 2012.

[34] A. J. Daley and J. Simon, "Effective three-body interactions via photon-assisted tunneling in an optical lattice," *Physical Review A*, vol. 89, p. 053619, May 2014.

[35] D. S. Petrov, "Three-Body Interacting Bosons in Free Space," *Physical Review Letters*, vol. 112, p. 103201, Mar. 2014.

[36] M. Hafezi, P. Adhikari, and J. M. Taylor, "Engineering three-body interaction and Pfaffian states in circuit QED systems," *Physical Review B*, vol. 90, p. 060503, Aug. 2014.

[37] E. Braaten and H.-W. Hammer, "Efimov physics in cold atoms," *Ann. of Phys.*, vol. 322, pp. 120–163, 2007.

[38] Y. Castin, "Bose-einstein condensates in atomic gases: simple theoretical results," *Coherent atomic matter waves, Lecture Notes of Les Houches Summer School 1999*, pp. 1–136, 2001.

[39] R. P. Feynman, *Statistical Mechanics, A Set of Lectures.* Addison-Wesley, Boston, 1972.

[40] V. M. Stojanović, C. Wu, W. V. Liu, and S. Das Sarma, "Incommensurate Superfluidity of Bosons in a Double-Well Optical Lattice," *Physical Review Letters*, vol. 101, p. 125301, Sept. 2008.

[41] C. Wu, "Unconventional Bose-Einstein condensations beyond the no-node theorem," *Modern Physics Letters B*, vol. 23, no. 1, pp. 1–24, 2009.

[42] A. Isacsson and S. M. Girvin, "Multiflavor bosonic Hubbard models in the first excited Bloch band of an optical lattice," *Physical Review A*, vol. 72, p. 053604, Nov. 2005.

[43] W. V. Liu and C. Wu, "Atomic matter of nonzero-momentum bose-einstein condensation and orbital current order," *Physical Review A*, vol. 74, no. 1, p. 013607, 2006.

[44] C. Wu and S. Das Sarma, "px,y-orbital counterpart of graphene: Cold atoms in the honeycomb optical lattice," *Physical Review B*, vol. 77, no. 23, p. 235107, 2008.

[45] Z. Cai and C. Wu, "Complex and real unconventional bose-einstein condensations in high orbital bands," *Physical Review A*, vol. 84, no. 3, p. 033635, 2011.

[46] G. Wirth, M. Ölschläger, and A. Hemmerich, "Evidence for orbital superfluidity in the P-band of a bipartite optical square lattice," *Nature Physics*, vol. 7, pp. 147–153, Dec. 2010.

[47] T. Müller, S. Fölling, A. Widera, and I. Bloch, "State preparation and dynamics of ultracold atoms in higher lattice orbitals," *Physical Review Letters*, vol. 99, no. 20, p. 200405, 2007.

[48] M. Ölschläger, G. Wirth, and A. Hemmerich, "Unconventional Superfluid Order in the F Band of a Bipartite Optical Square Lattice," *Physical Review Letters*, vol. 106, p. 015302, Jan. 2011.

[49] S. Paul and E. Tiesinga, "Formation and decay of Bose-Einstein condensates in an excited band of a double-well optical lattice," *Physical Review A*, vol. 88, p. 033615, Sept. 2013.

[50] W. Kohn, "Analytic Properties of Bloch Waves and Wannier Functions," *Physical Review*, vol. 115, pp. 809–821, Aug. 1959.

[51] G. H. Wannier, "Dynamics of Band Electrons in Electric and Magnetic Fields," *Reviews of Modern Physics*, vol. 34, pp. 645–655, Oct. 1962.

[52] K. L. Lee, B. Grémaud, R. Han, B.-G. Englert, and C. Miniatura, "Ultracold fermions in a graphene-type optical lattice," *Physical Review A*, vol. 80, p. 043411, Oct. 2009.

[53] N. Marzari and D. Vanderbilt, "Maximally localized generalized Wannier functions for composite energy bands," *Physical Review B*, vol. 56, no. 20, pp. 12847–12865, 1997.

[54] N. Marzari, A. A. Mostofi, J. R. Yates, I. Souza, and D. Vanderbilt, "Maximally localized Wannier functions: Theory and applications," *Reviews of Modern Physics*, vol. 84, no. 4, pp. 1419–1475, 2012.

[55] B. Vaucher, S. R. Clark, U. Dorner, and D. Jaksch, "Fast initialization of a high-fidelity quantum register using optical superlattices," *New Journal of Physics*, vol. 9, p. 221, July 2007.

[56] J. Ibañez Azpiroz, A. Eiguren, A. Bergara, G. Pettini, and M. Modugno, "Self-consistent tight-binding description of Dirac points moving and merging in two-dimensional optical lattices," *Physical Review A*, vol. 88, p. 033631, Sept. 2013.

[57] R. Walters, G. Cotugno, T. H. Johnson, S. R. Clark, and D. Jaksch, "*Ab initio* derivation of Hubbard models for cold atoms in optical lattices," *Physical Review A*, vol. 87, p. 043613, Apr. 2013.

[58] J. Ibañez Azpiroz, A. Eiguren, A. Bergara, G. Pettini, and M. Modugno, "Tight-binding models for ultracold atoms in honeycomb optical lattices," *Physical Review A*, vol. 87, p. 011602, Jan. 2013.

[59] D.-S. Lühmann, O. Jürgensen, M. Weinberg, J. Simonet, P. Soltan-Panahi, and K. Sengstock, "Quantum phases in tunable state-dependent hexagonal optical lattices," *Physical Review A*, vol. 90, p. 013614, July 2014.

[60] S. Kivelson, "Wannier functions in one-dimensional disordered systems: Application to fractionally charged solitons," *Physical Review B*, vol. 26, no. 8, pp. 4269–4277, 1982.

[61] C. Wu, W. V. Liu, J. Moore, and S. Das Sarma, "Quantum Stripe Ordering in Optical Lattices," *Physical Review Letters*, vol. 97, p. 190406, Nov. 2006.

[62] Q. Zhou, J. V. Porto, and S. Das Sarma, "Condensates induced by interband coupling in a double-well lattice," *Physical Review B*, vol. 83, p. 195106, May 2011.

[63] M. Ölschläger, G. Wirth, T. Kock, and A. Hemmerich, "Topologically Induced Avoided Band Crossing in an Optical Checkerboard Lattice," *Physical Review Letters*, vol. 108, p. 075302, Feb. 2012.

[64] K. Sun, W. V. Liu, A. Hemmerich, and S. D. Sarma, "Topological semimetal in a fermionic optical lattice," *Nature Physics*, vol. 8, pp. 67–70, Nov. 2011.

[65] D. T. Colbert and W. H. Miller, "A novel discrete variable representation for quantum mechanical reactive scattering via the Smatrix Kohn method," *The Journal of Chemical Physics*, vol. 96, no. 3, pp. 1982–1991, 1992.

[66] M. E. Fisher, M. N. Barber, and D. Jasnow, "Helicity modulus, superfluidity, and scaling in isotropic systems," *Phys. Rev. A*, vol. 8, pp. 1111–1124, Aug 1973.

[67] A. Smerzi, A. Trombettoni, P. G. Kevrekidis, and A. R. Bishop, "Dynamical superfluid-insulator transition in a chain of weakly coupled bose-einstein condensates," *Phys. Rev. Lett.*, vol. 89, p. 170402, Oct 2002.

[68] E. Altman, A. Polkovnikov, E. Demler, B. I. Halperin, and M. D. Lukin, "Superfluid-insulator transition in a moving system of interacting bosons," *Phys. Rev. Lett.*, vol. 95, p. 020402, Jul 2005.

[69] D. Jaksch, C. Bruder, J. I. Cirac, C. W. Gardiner, and P. Zoller, "Cold Bosonic Atoms in Optical Lattices," *Phys. Rev. Lett.*, vol. 81, p. 3108, 1998.

[70] M. Greiner, O. Mandel, T. Esslinger, T. W. Hänsch, and I. Bloch, "Quantum phase transition from a superfluid to a Mott insulator in a gas of ultracold atoms," *Nature*, vol. 415, p. 39, 2002.

[71] P. J. Lee, M. Anderlini, B. L. Brown, J. Sebby-Strabley, W. D. Phillips, and J. V. Porto, "Sublattice addressing and spin-dependent motion of atoms in a double-well lattice," *Phys. Rev. Lett.*, vol. 99, p. 020402, 2007.

[72] Y. Qian, M. Gong, and C. Zhang, "Quantum transport of bosonic cold atoms in double-well optical lattices," *Phys. Rev. A*, vol. 84, p. 013608, 2011.

[73] M. Ölschläger, G. Wirth, T. Kock, and A. Hemmerich, "Topologically induced avoided band crossing in an optical checkerboard lattice," *Phys. Rev. Lett.*, vol. 108, p. 075302, Feb 2012.

[74] P. Soltan-Panahi, D.-S. Lhmann, J. Struck, P. Windpassinger, and K. Sengstock, "Quantum phase transition to unconventional multi-orbital superfluidity in optical lattices," *Nature Physics*, vol. 8, pp. 71–75, 2012.

[75] M. Snoek and W. Hofstetter, "Two-dimensional dynamics of ultracold atoms in optical lattices," *Phys. Rev. A*, vol. 76, p. 051603, 2007.

[76] T. Uehlinger, G. Jotzu, M. Messer, D. Greif, W. Hofstetter, U. Bissbort, and T. Esslinger, "Artificial graphene with tunable interactions," *Phys. Rev. Lett.*, vol. 111, p. 185307, 2013.

[77] O. Jrgensen and D.-S. Lhmann, "Dimerized Mott insulators in hexagonal optical lattices," *New Journal of Physics*, vol. 16, p. 093023, 2014.

[78] Y.-J. Lin, R. L. Compton, A. R. Perry, W. D. Phillips, J. V. Porto, and I. B. Spielman, "Bose-Einstein Condensate in a Uniform Light-Induced Vector Potential," *Phys. Rev. Lett.*, vol. 102, p. 130401, 2009.

[79] Y.-J. Lin, K. Jiménez-García, and I. B. Spielman, "Spin-orbit-coupled Bose-Einstein condensates," *Nature*, vol. 471, pp. 83–86, 2011.

[80] A. Hu, L. Mathey, I. Danshita, E. Tiesinga, C. J. Williams, and C. W. Clark, "Counterflow and paired superfluidity in one-dimensional Bose mixtures in optical lattices," *Phys. Rev. A*, vol. 80, p. 023619, 2009.

[81] A. T. Bolukbasi and M. Iskin, "Superfluid-Mott-insulator transition in the spin-orbit-coupled Bose-Hubbard model," *Phys. Rev. A*, vol. 89, p. 043603, 2014.

[82] R. C. Brown, R. Wyllie, S. B. Koller, E. A. Goldschmidt, M. Foss-Feig, and J. V. Porto, "Two-dimensional superexchange-mediated magnetization dynamics in an optical lattice," *Science*, vol. 348, pp. 540–544, 2015.

[83] G. Rosi, F. Sorrentino, L. Cacciapuoti, M. Prevedelli, and G. M. Tino, "Precision measurement of the Newtonian gravitational constant using cold atoms," *Nature*, vol. 510, pp. 518–521, 2014.

[84] K. W. Mahmud, L. Jiang, E. Tiesinga, and P. R. Johnson, "Bloch oscillations and quench dynamics of interacting bosons in an optical lattice," *Phys. Rev. A*, vol. 89, p. 023606, 2014.

[85] F. Meinert, M. J. Mark, E. Kirilov, K. Lauber, P. Weinmann, M. Gröbner, and H.-C. Nägerl, "Interaction-induced quantum phase revivals and evidence for the transition to the quantum chaotic regime in 1d atomic bloch oscillations," *Phys. Rev. Lett.*, vol. 112, p. 193003, 2014.

[86] V. Giovannetti, S. Lloyd, and L. Maccone, "Advances in quantum metrology," *Nat Photon*, vol. 5, pp. 222–229, 2011.

[87] J. Javanainen and H. Chen, "Optimal measurement precision of a nonlinear interferometer," *Phys. Rev. A*, vol. 85, p. 063605, 2012.

[88] E. Tiesinga and P. R. Johnson, "Quadrature interferometry for nonequilibrium ultracold atoms in optical lattices," *Phys. Rev. A*, vol. 87, p. 013423, 2013.

[89] K. W. Mahmud, E. Tiesinga, and P. R. Johnson, "Dynamically decoupled three-body interactions with applications to interaction-based quantum metrology," *Phys. Rev. A*, vol. 90, p. 041602, 2014.

[90] T. Kraemer, M. Mark, P. Waldburger, J. G. Danzl, C. Chin, B. Engeser, A. D. Lange, K. Pilch, A. Jaakkola, H.-C. Nägerl, and R. Grimm, "Evidence for Efimov quantum states in an ultracold gas of caesium atoms," *Nature*, vol. 440, no. 7082, pp. 315–318, 2006.

[91] F. Ferlaino and R. Grimm, "Forty years of Efimov physics: How a bizarre prediction turned into a hot topic," *Physics*, vol. 3, p. 9, 2010.

[92] J. Wang, J. P. D'Incao, Y. Wang, and C. H. Greene, "Universal three-body recombination via resonant d-wave interactions," *Phys. Rev. A*, vol. 86, p. 062511, 2012.

[93] Y. Wang and P. S. Julienne, "Universal van der Waals physics for three cold atoms near Feshbach resonances," *Nat. Phys.*, vol. 10, pp. 768–773, 2014.

[94] Z. Shotan, O. Machtey, S. Kokkelmans, and L. Khaykovich, "Three-Body Recombination at Vanishing Scattering Lengths in an Ultracold Bose Gas," *Phys. Rev. Lett.*, vol. 113, p. 053202, 2014.

[95] D. S. Petrov, "Three-Body Interacting Bosons in Free Space," *Phys. Rev. Lett.*, vol. 112, p. 103201, 2014.

[96] A. J. Daley and J. Simon, "Effective three-body interactions via photon-assisted tunneling in an optical lattice," *Phys. Rev. A*, vol. 89, p. 053619, 2014.

[97] S. Paul and E. Tiesinga, "Large effective three-body interaction in a double-well optical lattice," *Phys. Rev. A*, vol. 92, p. 023602, 2015.

[98] H. Kadau, M. Schmitt, M. Wenzel, C. Wink, T. Maier, I. Ferrier-Barbut, and T. Pfau, "Observing the Rosensweig instability of a quantum ferrofluid," *Nature*, vol. 530, pp. 194–197, Feb. 2016.

[99] K.-T. Xi and H. Saito, "Droplet formation in a bose-einstein condensate with strong dipole-dipole interaction," *Phys. Rev. A*, vol. 93, p. 011604, Jan 2016.

[100] R. N. Bisset and P. B. Blakie, "Crystallization of a dilute atomic dipolar condensate," *Phys. Rev. A*, vol. 92, p. 061603, Dec 2015.

[101] B. Gao, "Analytic description of atomic interaction at ultracold temperatures: The case of a single channel," *Phys. Rev. A*, vol. 80, p. 012702, 2009.

[102] G. F. Gribakin and V. V. Flambaum, "Calculation of the scattering length in atomic collisions using the semiclassical approximation," *Phys. Rev. A*, vol. 48, p. 546, 1993.

[103] C. Chin, R. Grimm, P. Julienne, and E. Tiesinga, "Feshbach resonances in ultracold gases," *Rev. Mod. Phys.*, vol. 82, pp. 1225–1286, 2010.

[104] P. R. Johnson, E. Tiesinga, J. V. Porto, and C. J. Williams, "Effective three-body interactions of neutral bosons in optical lattices," *New Journal of Physics*, vol. 11, p. 093022, 2009.

[105] X. Y. Yin, D. Blume, P. R. Johnson, and E. Tiesinga, "Universal and nonuniversal effective N-body interactions for ultracold harmonically trapped few-atom systems," *Phys. Rev. A*, vol. 90, p. 043631, 2014.

[106] K. Huang and C. N. Yang, "Quantum-Mechanical Many-Body Problem with Hard-Sphere Interaction," *Phys. Rev.*, vol. 105, pp. 767–775, 1957.

[107] A. Derevianko, "Revised Huang-Yang multipolar pseudopotential," *Phys. Rev. A*, vol. 72, p. 044701, 2005.

[108] Z. Idziaszek and T. Calarco, "Pseudopotential Method for Higher Partial Wave Scattering," *Phys. Rev. Lett.*, vol. 96, p. 013201, 2006.

[109] L. Pricoupenko, "Pseudopotential in resonant regimes," *Phys. Rev. A*, vol. 73, p. 012701, 2006.

[110] D. van Oosten, P. van der Straten, and H. T. C. Stoof, "Quantum phases in an optical lattice," *Phys. Rev. A*, vol. 63, p. 053601, 2001.

[111] T. Busch, B.-G. Englert, K. Rzazewski, and M. Wilkens, "Two Cold Atoms in a Harmonic Trap," *Found. of Phys.*, vol. 28, pp. 549–559, 1998.

[112] A. Zee, *Quantum Field Theory in a Nutshell*. Princeton University Press, 2nd ed., 2010.

[113] S. R. Beane, W. Detmold, and M. J. Savage, "n-boson energies at finite volume and three-boson interactions," *Phys. Rev. D*, vol. 76, p. 074507, 2007.

[114] V. V. Flambaum, G. F. Gribakin, and C. Harabati, "Analytical calculation of cold-atom scattering," *Physical Review A*, vol. 59, no. 3, pp. 1998–2005, 1999.

[115] B. Gao, "Quantum-defect theory of atomic collisions and molecular vibration spectra," *Phys. Rev. A*, vol. 58, p. 4222, 1998.

[116] A. Stein, H. Knöckel, and E. Tiemann, "The 1s 1s asymptote of Sr2 studied by Fourier-transform spectroscopy," *Eur. Phys. J. D*, vol. 57, no. 2, p. 171, 2010.

[117] J. Werner, A. Griesmaier, S. Hensler, J. Stuhler, T. Pfau, A. Simoni, and E. Tiesinga, "Observation of Feshbach resonances in an ultracold gas of ^{52}Cr," *Phys. Rev. Lett.*, vol. 94, p. 183201, 2005.

[118] A. Frisch, M. Mark, K. Aikawa, F. Ferlaino, J. L. Bohn, C. Makrides, A. Petrov, and S. Kotochigova, "Quantum chaos in ultracold collisions of gas-phase erbium atoms," *Nature*, vol. 507, pp. 475–479, 2014.

[119] A. Petrov, E. Tiesinga, and S. Kotochigova, "Anisotropy-Induced Feshbach Resonances in a Quantum Dipolar Gas of Highly Magnetic Atoms," *Phys. Rev. Lett.*, vol. 109, p. 103002, 2012.

[120] K. Baumann, N. Q. Burdick, M. Lu, and B. L. Lev, "Observation of low-field Fano-Feshbach resonances in ultracold gases of dysprosium," *Phys. Rev. A*, vol. 89, p. 020701, 2014.

[121] U. Fano, "Effects of Configuration Interaction on Intensities and Phase Shifts," *Phys. Rev.*, vol. 124, p. 1866, 1961.

[122] J. R. Taylor, *Scattering Theory*. John Wiley & Sons, London, 1st ed., 1972.

[123] T. Köhler, K. Góral, and P. S. Julienne, "Production of cold molecules via magnetically tunable Feshbach resonances," *Rev. Mod. Phys.*, vol. 78, pp. 1311–1361, 2006.

[124] D. S. Petrov, "Three-Boson Problem near a Narrow Feshbach Resonance," *Phys. Rev. Lett.*, vol. 93, p. 143201, 2004.

[125] C. L. Blackley, P. S. Julienne, and J. M. Hutson, "Effective-range approximations for resonant scattering of cold atoms," *Phys. Rev. A*, vol. 89, p. 042701, 2014.

[126] T. Stöferle, H. Moritz, K. Günter, M. Köhl, and T. Esslinger, "Molecules of Fermionic Atoms in an Optical Lattice," *Phys. Rev. Lett.*, vol. 96, p. 030401, 2006.

[127] C. Ospelkaus, S. Ospelkaus, L. Humbert, P. Ernst, K. Sengstock, and K. Bongs, "Ultracold heteronuclear molecules in a 3d optical lattice," *Phys. Rev. Lett.*, vol. 97, p. 120402, 2006.

[128] E. Tiesinga, C. J. Williams, F. H. Mies, and P. S. Julienne, "Interacting Atoms Under Strong Quantum Confinement," *Phys. Rev. A*, vol. 61, p. 063416, 2000.

[129] M. Greiner, O. Mandel, T. W. Hänsch, and I. Bloch, "Collapse and revival of the matter wave field of a BoseEinstein condensate," *Nature*, vol. 419, pp. 51–54, 2002.

[130] J. Sebby-Strabley, B. L. Brown, M. Anderlini, P. J. Lee, W. D. Phillips, J. V. Porto, and P. R. Johnson, "Preparing and probing atomic number states with an atom interferometer," *Physical Review Letters*, vol. 98, p. 200405, 2007.

[131] S. Will, T. Best, U. Schneider, L. Hackermuller, D.-S. Luhmann, and I. Bloch, "Time-resolved observation of coherent multi-body interactions in quantum phase revivals," *Nature*, vol. 465, pp. 197–201, 2010.

[132] B. D. Esry, C. H. Greene, and J. P. Burke, "Recombination of Three Atoms in the Ultracold Limit," *Phys. Rev. Lett.*, vol. 83, p. 1751, 1999.

[133] K. S. Novoselov, A. K. Geim, S. V. Morozov, D. Jiang, M. I. Katsnelson, I. V. Grigorieva, S. V. Dubonos, and A. A. Firsov, "Two-dimensional gas of massless dirac fermions in graphene," *Nature*, vol. 438, p. 197, 2005.

[134] H. Lignier, C. Sias, D. Ciampini, Y. Singh, A. Zenesini, O. Morsch, and E. Arimondo, "Dynamical control of matter-wave tunneling in periodic potentials," *Phys. Rev. Lett.*, vol. 99, p. 220403, 2007.

[135] J. Struck, C. Olschlager, R. Le Targat, P. Soltan-Panahi, A. Eckardt, M. Lewenstein, P. Windpassinger, and K. Sengstock, "Quantum simulation of frustrated classical magnetism in triangular optical lattices," *Science*, vol. 333, pp. 996–999, 2011.

[136] M. V. Berry, "Quantal phase factors accompanying adiabatic changes," *Proceedings of the Royal Society of London. A. Mathematical and Physical Sciences*, vol. 392, p. 45, 1984.

[137] A. Altland and B. Simons, *Condensed Matter Field Theory*. Cambridge University Press, 2008.

[138] C. Cohen-Tannoudji, J. Dupont-Roc, and G. Grynberg, *Atom-Photon Interactions: Basic Processes and Applications*. Wiley-Interscience, 1992.

[139] M. Edwards, R. J. Dodd, C. W. Clark, and K. Burnett, "Zero-temperature, mean-field theory of atomic Bose-Einstein condensates," *J. Res. Natl. Inst. Stand. Technol.*, vol. 101, no. 4, p. 553, 1996.

[140] V. Szalay, "Discrete variable representations of differential operators," *The Journal of Chemical Physics*, vol. 99, pp. 1978–1984, Aug. 1993.

[141] E. Tiesinga, C. J. Williams, and P. S. Julienne, "Photoassociative spectroscopy of highly excited vibrational le vels of alkali-metal dimers: Green-function approach for eigenvalue solvers," *Physical Review A*, vol. 57, pp. 4257–4267, June 1998.

[142] R. G. Littlejohn, M. Cargo, T. C. Jr, K. A. Mitchell, and B. Poirier, "A general framework for discrete variable representation basis sets," *The Journal of Chemical Physics*, vol. 116, pp. 8691–8703, May 2002.

[143] V. Szalay, G. Czakó, A. Nagy, T. Furtenbacher, and A. G. Császár, "On one-dimensional discrete variable representations with general basis functions," *The Journal of Chemical Physics*, vol. 119, pp. 10512–10518, Nov. 2003.

[144] N. Nygaard, G. M. Bruun, B. I. Schneider, C. W. Clark, and D. L. Feder, "Vortex line in a neutral finite-temperature superfluid Fermi gas," *Physical Review A*, vol. 69, p. 053622, May 2004.

[145] M. L. Wall, K. R. A. Hazzard, and A. M. Rey, "Effective many-body parameters for atoms in non-separable Gaussian optical potentials," *Physical Review A*, vol. 92, July 2015.